The Buffered Block Forward Backward technique for solving electromagnetic wave scattering problems

Diana Boguşevschi

A dissertation submitted in fulfilment of the requirements for the award of

Doctor of Philosophy

to the

School of Electronic Engineering

Dublin City University

Supervisor: Dr. Conor Brennan

February 2010

Declaration

I hereby certify that this material, which I now submit for assessment on the programme of study leading to the award of Doctor of Philosophy is entirely my own work, that I have exercised reasonable care to ensure that the work is original, and does not to the best of my knowledge breach any law of copyright, and has not been taken from the work of others save and to the extent that such work has been cited and acknowledged within the text of my work.

Signed: _____ ID No.: 55156444

(Diana Boguşevschi)

Date: February 10, 2010

Abstract

This work focuses on efficient numerical techniques for solving electromagnetic wave scattering problems. The research is focused on three main areas: scattering from perfect electric conductors, 2D dielectric scatterers and 3D dielectric scattering objects. The problem of fields scattered from perfect electric conductors is formulated using the Electric Field Integral Equation. The Coupled Field Integral Equation is used when a 2D homogeneous dielectric object is considered. The Combined Field Integral Equation describes the problem of scattering from 3D homogeneous dielectric objects. Discretising the Integral Equation Formulation using the Method of Moments creates the matrix equation that is to be solved. Due to the large number of discretisations necessary the resulting matrices are of significant size and therefore the matrix equations cannot be solved by direct inversion and iterative methods are employed instead. Various iterative techniques for solving the matrix equation are presented including stationary methods such as the "forward-backward" technique, as well its matrix-block version. A novel iterative solver referred to as Buffered Block Forward Backward (BBFB) method is then described and investigated. It is shown that the incorporation of buffer regions dampens spurious diffraction effects and increases the computational efficiency of the algorithm. The BBFB is applied to both perfect electric conductors and homogeneous dielectric objects. The convergence of the BBFB method is compared to that of other techniques and it is shown that, depending on the grouping and buffering used, it can be more effective than classical methods based on Krylov subspaces for example. A possible application of the BBFB, namely the design of 2D dielectric photonic band-gap TeraHertz waveguides is investigated.

Acknowledgements

I would like to thank my supervisor Dr. Conor Brennan for his help, advice and commitment to this work. Thanks are also due to my fellow colleagues in the RINCE Research group Barry Kirkpatrick, John Diskin, Marie Mullen, Patrick Bradley and Elif Degirmenci.

Contents

List of Figures

List of Tables

Chapter 1

Thesis Overview

The problem of electromagnetic wave scattering is of great importance in the domain of computational electromagnetics. Maxwell's equations underpin all computational electromagnetic techniques allowing a thorough and precise description of the electromagnetic behaviour of any structure. There are numerous books on fundamental electromagnetics, such as [1] by Umran and Aziz, [2] by Balanis, [3] by Peterson *et al.*, [4] by Chew *et al.*. These deliver an extensive view of the particular area of Computational Electromagnetics, and the methods and techniques associated with it. Chapter 2 of this thesis describes a general introduction to the basic concepts of Electromagnetics. Maxwell's equations in differential and integral form are presented in Section 2.1. A brief description of available numerical methods for solving Maxwell's equations is provided in Section 2.2. These include the Finite Difference Time-Domain Method (FDTD), the Finite Element Method (FEM) and Ray Tracing.

This thesis is focused on the Surface Field Integral Equation (SFIE) formulation and its solution using the Method of Moments. An in depth review of the Integral Equation (IE) formulation and the Method of Moments (MoM) is presented in Chapter 3. The IE offers an exact description of wave scattering problems and is presented in Section 3.1. Various IE formulations applicable to different classes of problems are reviewed in this Section. The IE formulation differs for perfectly electrically conducting scatterers, homogeneous and inhomogeneous dielectric bodies. The Magnetic Field Integral Equation (MFIE) and the Electric Field Integral Equation (EFIE) can be both used for problems involving perfectly

electrically conducting scatterers. However the MFIE is not suitable for open bodies and infinitesimally thin objects. For 2D homogeneous dielectric bodies the Coupled EFIE or Coupled MFIE can be used in order to formulate the electromagnetic scattering problem. However the Coupled IE formulations tend to introduce errors due to interior resonances. A comparison between the MFIE and EFIE formulations is presented in [5], showing that the MFIE tends to outperform the EFIE in terms of convergence when applied to perfect electrically conducting surfaces. This is due to a better conditioning of the matrix obtained after applying the Method of Moments to the IE formulation. The two methods were linearly combined in [5] and applied to wavelike surfaces and homogeneous cylinders, leading to the Combined Field Integral Equation (CFIE) that showed higher convergence rates compared to each formulation applied separately. A similar procedure was performed earlier in [6] where the CFIE was derived for perfect electric conductors. It can be noted that the Combined Field Integral Equation is equivalent to a linear combination of the Coupled EFIE and the Coupled MFIE. It avoids the interior resonance problems associated with the Coupled IE formulations. Hence the CFIE formulation is currently widely used when solving problems of wave scattering from 3D objects [1; 3].

The Method of Moments (MoM) is a technique used to discretise integral equations in order to obtain a matrix equation and is presented in Section 3.2. The surface of the scatterer is discretised and basis functions are associated with the partitions. The partitions are usually small in terms of wavelength, but some basis functions defined on large domains exist. In addition to the basis functions, testing or weighting functions are employed in order to enforce the boundary conditions and to compensate possible discontinuities of the fields that may occur after applying the basis functions. In this work, when solving the problem of electromagnetic wave scattering from a 2D object the discretisation procedure is straightforward, where the surface is divided into small segments, and a pulse basis function is associated with each segment, as is outlined in [7]. The weighting functions employed in this case are the Dirac delta testing functions enforcing the boundary conditions at the midpoint of each segment [3].

The discretisation of 3D scatterers is more complex compared to the 2D scatterers. The arbitrary perfect electric conducting bodies are usually partitioned using the Rao-Wilton-

Glisson (RWG) basis function technique [8]. In this thesis the testing functions employed in this case enforce the boundary conditions across the triangle centroids. The same discretisation technique is used for the 3D homogeneous dielectric scatterers. However, the testing function used for the homogeneous dielectric scatterers is different from the one used for perfect electric conductors, whereby this weighting function is chosen to be identical to the basis function. This is also known as the Galerkin testing function and is introduced by Umashankar, Taflove and Rao in [9].

The discretisation of the integral equation via the MoM results in a number of linearly independent equations, each one associated with a testing function. The set of linear equations constitute a matrix equation that is to be solved. The left hand side of the equation is represented by the dense impedance matrix which defines the interactions between the basis functions and testing functions and the unknown vector of basis function amplitudes. The right hand side is a vector containing information about the incident field.

In many cases the size of the scattering object is extremely large in terms of the wavelengths. Hence, after applying the MoM to the IE formulation, the resulting matrix equation will be difficult or impossible to store. Therefore solving the matrix equation by direct matrix inversion is extremely time consuming or impossible. This is the motivation behind using the iterative solvers instead. They allow the sequential "building up" of a solution for the current density without having to explicitly store or invert the matrix. In the case of stationary solvers this is referred to as "current marching".

There are two main types of iterative solvers: stationary and non stationary. The *stationary* methods comprise the Gauss-Seidel, Jacobi, Successive Overrelaxation (SOR), Symmetric Successive Overrelaxation (SSOR) among others. The *non stationary* methods are based on the development of Krylov subspaces. The most common non stationary methods are Conjugate Gradient (CG) and Generalized Minimum Residual (GMRES). A thorough history of iterative solvers is presented in [10], describing how these methods evolved from being viewed as slow and inefficient to becoming an extremely important part of computational science and engineering. [11; 12; 13; 14; 15; 16; 17; 18; 19] are a few of the bibliography items that deliver an in depth description and analysis of iterative solvers.

A key current research topic is the development of computationally efficient iterative solvers. For example West and Sturm [20] performed a study of different iterative techniques examining their performance when applied to systems resulting from electromagnetic wave scattering from breaking water waves. The non stationary iterative solvers were shown to be very reliable in terms of convergence. These methods tend to converge in most cases regardless of the geometry of the scattering surface. The convergence rates of the stationary methods are a lot more inconsistent. The stationary methods tend to work well when applied to problems involving objects that do not exhibit the possibility of much multiple scattering. Therefore these methods are not effective for complex geometrical surfaces. Nevertheless stationary methods were shown to converge at a much faster rate compared to non stationary techniques when applied to problems of scattering from simple structures. The convergence characteristics of the iterative solvers is highly dependent on the spectral properties of the coefficient matrix. Preconditioners are matrices employed in order to improve these spectral properties. This is achieved by multiplying each side of the matrix equations with an appropriate preconditioner. This results in having the same solution as the original system, but with improved spectral properties. A comprehensive description of the preconditioning methods is provided in [12; 14; 17; 21; 22]. Iterative solvers and preconditioning techniques are reviewed in Chapter 4.

The subsequent chapters describe the work done by the author. The new Buffered Block Forward Backward (BBFB) Method for solving the problem of wave scattering from perfect electric conductors is presented in Chapter 5. The classical Forward Backward method represents current marching from basis function to basis function. The BBFB technique introduces the innovation of marching the currents from block to block. The block term refers to the fact that the basis functions are grouped into sub-regions, whereas the buffer represents the neighboring sub-region region. The introduction of the buffer regions allows the suppression of spurious diffraction effects that would occur otherwise, which leads to improved convergence.

In Chapter 6 the Buffered Block Forward Backward method is extended to problems of scattering from 2D homogeneous dielectric scatterers. A 2D application of the BBFB method, namely the design of 2D TeraHertz photonic band gap waveguides is presented

in Chapter 7. Chapter 8 describes the extension of the BBFB method to problems of electromagnetic wave scattering from 3D homogeneous dielectric objects. In all cases the convergence of the BBFB method is compared to that of various Krylov solvers. Conclusions and future work are presented in Chapter 9.

Note: In this work vector fields appear in bold with a bar over the letter (e.g. $\bar{\boldsymbol{\mathcal{E}}}$, $\bar{\mathbf{E}}$, matrices and vectors are represented in bold (e.g. $\mathbf{Z}$, $\mathbf{V}$) and scalars in italic (e.g. A_z, J_z).

Chapter 2

Review of Computational Electromagnetics

2.1 Maxwell's Equations

All electromagnetic phenomena have to satisfy a set of equations known as *Maxwell's equations*, which were independently obtained through experiments before being combined together with the correctional displacement current by Maxwell. This set of equations is based on Coulomb's law, Ampere's law, Faraday's law and the principle of conservation of electric charge and it reflects all the properties of electromagnetics, such as the fact that a time-changing magnetic flux induces an electromotive force and a time-varying electric field produces a magnetic field, that light is an electromagnetic wave and that electric and magnetic fields can be transmitted through space whether it's filled with matter or empty.

2.1.1 Differential form of Maxwell's equations

Maxwell's equations in differential form are used to describe the field vectors, current densities and charge densities at any point in space at any time. The differential form of Maxwell's equations is the most widely used form in computational electromagnetics and

is presented below [1; 3; 2]:

$$\nabla \times \bar{\boldsymbol{\mathcal{E}}} = -\bar{\boldsymbol{\mathcal{K}}}^i - \frac{\partial \bar{\boldsymbol{\mathcal{B}}}}{\partial t} \tag{2.1}$$

$$\nabla \cdot \bar{\boldsymbol{\mathcal{D}}} = \rho_e \tag{2.2}$$

$$\nabla \times \bar{\boldsymbol{\mathcal{H}}} = \bar{\boldsymbol{\mathcal{J}}}^i + \frac{\partial \bar{\boldsymbol{\mathcal{D}}}}{\partial t} \tag{2.3}$$

$$\nabla \cdot \bar{\boldsymbol{\mathcal{B}}} = \rho_m \tag{2.4}$$

All these quantities are functions of both time and space, and are defined below:

$\bar{\boldsymbol{\mathcal{E}}}$ = electric field intensity (Volts/metre)

$\bar{\boldsymbol{\mathcal{B}}}$ = magnetic flux density (Webers/square metre)

$\bar{\boldsymbol{\mathcal{D}}}$ = electric flux density (Coulombs/square metre)

$\bar{\boldsymbol{\mathcal{H}}}$ = magnetic field intensity (Amperes/metre)

$\bar{\boldsymbol{\mathcal{K}}}^i$ = source magnetic current density (Volts/square metre)

$\bar{\boldsymbol{\mathcal{J}}}^i$ = source electric current density (Amperes/square metre)

ρ_e = electric charge density (Coulombs/cubic metre)

ρ_m = magnetic charge density (Webers/cubic metre)

Equation (2.1) also known as Faraday's Law is based on the experimental fact that time-changing magnetic flux produces an electric field. Equation (2.2) also known as Gauss' law describes the fact that electric charges attract or repel each other with a force inversely proportional to the square of the distance between them. Ampere's Law is presented in the third Maxwell's equation and it states that time-changing electric flux produces a magnetic field. The ρ_m term in Equation (2.4) is introduced , despite the fact that magnetic charges do not exist, in order to balance Maxwell's equations and it will be used in later chapters. In the absence of the ρ_m term Equation (2.4) states that the magnetic field lines close in themselves [1]. $\bar{\boldsymbol{\mathcal{K}}}^i$ is introduced for similar reasons.

2.1.2 Integral form of Maxwell's equations

In contrast to the differential formulation, the integral formulation of Maxwell's equations describes the field vectors, charge densities and current densities over an extended region of space. The integral form of Maxwell's equations is obtained using the divergence and Stokes' theorems.

According to Stokes' theorem the line integral of an arbitrary vector field $\bar{\mathbf{W}}$ along a closed path $\mathscr{C}$ is equal to the integral of the dot product of the curl of the vector field $\bar{\mathbf{W}}$ with the normal to the surface $\mathscr{S}$ that has the contour $\mathscr{C}$ as its boundary [2]. This can be expressed as:

$$\oint_{\mathscr{C}} \bar{\mathbf{W}} \cdot d\mathbf{l} = \iint_{\mathscr{S}} (\nabla \times \bar{\mathbf{W}}) \cdot d\mathbf{s} \tag{2.5}$$

Therefore the integral forms of Faraday's and Ampere's laws can be obtained:

$$\iint_{\mathscr{S}} (\nabla \times \bar{\boldsymbol{\mathcal{E}}}) \cdot d\mathbf{s} = -\iint_{\mathscr{S}} \bar{\boldsymbol{\mathcal{K}}}^i \cdot d\mathbf{s} - \iint_{\mathscr{S}} \frac{\partial \bar{\boldsymbol{\mathcal{B}}}}{\partial t} \cdot d\mathbf{s} \tag{2.6}$$

After applying Stokes' theorem Equation (2.6) becomes:

$$\oint_{\mathscr{C}} \bar{\boldsymbol{\mathcal{E}}} \cdot d\mathbf{l} = -\iint_{\mathscr{S}} \bar{\boldsymbol{\mathcal{K}}}^i \cdot d\mathbf{s} - \iint_{\mathscr{S}} \frac{\partial \bar{\boldsymbol{\mathcal{B}}}}{\partial t} \cdot d\mathbf{s} \tag{2.7}$$

In the same manner, Ampere's law can be derived using Stokes' theorem:

$$\oint_{\mathscr{C}} \bar{\boldsymbol{\mathcal{H}}} \cdot d\mathbf{l} = \iint_{\mathscr{S}} \bar{\boldsymbol{\mathcal{J}}}^i \cdot d\mathbf{s} + \iint_{\mathscr{S}} \frac{\partial \bar{\boldsymbol{\mathcal{D}}}}{\partial t} \cdot d\mathbf{s} \tag{2.8}$$

According to the divergence theorem the closed surface integral of the normal component of an arbitrary vector field $\bar{\mathbf{W}}$ over a surface $\mathscr{S}$ is equal to the volume integral of the divergence of $\bar{\mathbf{W}}$ over the volume $\mathscr{V}$ enclosed by $\mathscr{S}$ [2]. This can be expressed as:

$$\oint_{\mathscr{S}} \bar{\mathbf{W}} \cdot d\mathbf{s} = \int_{\mathscr{V}} \nabla \cdot \bar{\mathbf{W}} dv \tag{2.9}$$

The integral form of Gauss's law can be expressed using the divergence theorem [2]:

$$\int_{\mathscr{V}} \nabla \cdot \bar{\boldsymbol{\mathcal{D}}} dv = \int_{\mathscr{V}} \rho_e dv = \mathcal{Q}_e \tag{2.10}$$

which leads to:

$$\oint_{\mathscr{S}} \bar{\boldsymbol{\mathcal{D}}} \cdot d\mathbf{s} = \int_{\mathscr{V}} \rho_e dv = \mathcal{Q}_e \tag{2.11}$$

where $\mathcal{Q}_e$ is the total electric charge inside the volume $\mathscr{V}$. The same procedure can be applied to the fourth Maxwell's equation. Therefore Maxwell's equations in integral form can be written [1; 3; 2]:

$$\oint_{\mathscr{C}} \bar{\boldsymbol{\mathcal{E}}} \cdot d\mathbf{l} = -\iint_{\mathscr{S}} \bar{\boldsymbol{\mathcal{K}}}^i \cdot d\mathbf{s} - \iint_{\mathscr{S}} \frac{\partial \bar{\boldsymbol{\mathcal{B}}}}{\partial t} \cdot d\mathbf{s} \tag{2.12}$$

$$\oint_{\mathscr{S}} \bar{\boldsymbol{\mathcal{D}}} \cdot d\mathbf{s} = \mathcal{Q}_e \tag{2.13}$$

$$\oint_{\mathscr{C}} \bar{\boldsymbol{\mathcal{H}}} \cdot d\mathbf{l} = \iint_{\mathscr{S}} \bar{\boldsymbol{\mathcal{J}}}^i \cdot d\mathbf{s} + \iint_{\mathscr{S}} \frac{\partial \bar{\boldsymbol{\mathcal{D}}}}{\partial t} \cdot d\mathbf{s} \tag{2.14}$$

$$\oint_{\mathscr{S}} \bar{\boldsymbol{\mathcal{B}}} \cdot d\mathbf{s} = \mathcal{Q}_m \tag{2.15}$$

2.1.3 Time-harmonic form of Maxwell's equations

The differential and integral forms of Maxwell's equations have been presented in Sections 2.1.1 and 2.1.2. A further simplification of Maxwell's equations can be achieved by assuming that the field is time harmonic. This enables the expression of the differential and integral forms of Maxwell's equations in a simpler manner. The time-harmonic fields can be related to the instantaneous fields using the time dependence $e^{j\omega t}$. Assume $\bar{\boldsymbol{\mathcal{W}}}$ to represent an instantaneous field vector, then the corresponding complex spatial form $\bar{\mathbf{W}}$ is

obtained as presented in Equation (2.16)

$$\bar{\boldsymbol{\mathcal{W}}}(x,y,z;t) = \Re e[\bar{\mathbf{W}}(x,y,z)e^{j\omega t}] \tag{2.16}$$

The time-harmonic differential and integral form of Maxwell's equations can be obtained by replacing the instantaneous fields by the corresponding complex spatial forms and by replacing $\frac{\partial}{\partial t}$ with $j\omega$.

Therefore the time-harmonic differential form of Maxwell's equations can be formulated below [2]:

$$\nabla \times \bar{\mathbf{E}} = -\bar{\mathbf{K}}^i - j\omega\bar{\mathbf{B}} \tag{2.17}$$

$$\nabla \cdot \bar{\mathbf{D}} = \rho_e \tag{2.18}$$

$$\nabla \times \bar{\mathbf{H}} = \bar{\mathbf{J}}^i + j\omega\bar{\mathbf{D}} \tag{2.19}$$

$$\nabla \cdot \bar{\mathbf{B}} = \rho_m \tag{2.20}$$

Consequently, the time-harmonic integral equation form of Maxwell's equations is expressed in Equations (2.21-2.24).

$$\oint_{\mathscr{C}} \bar{\mathbf{E}} \cdot \mathbf{dl} = -\iint_{\mathscr{S}} \bar{\mathbf{K}}^i \cdot d\mathbf{s} - j\omega \iint_S \bar{\mathbf{B}} \cdot d\mathbf{s} \tag{2.21}$$

$$\oint_{\mathscr{S}} \bar{\mathbf{D}} \cdot d\mathbf{s} = Q_e \tag{2.22}$$

$$\oint_{\mathscr{C}} \bar{\mathbf{H}} \cdot d\mathbf{l} = \iint_S \bar{\mathbf{J}}^i \cdot d\mathbf{s} + j\omega \iint_{\mathscr{S}} \bar{\mathbf{D}} \cdot d\mathbf{s} \tag{2.23}$$

$$\oint_{\mathscr{S}} \bar{\mathbf{B}} \cdot d\mathbf{s} = Q_m \tag{2.24}$$

2.2 Numerical Solutions

There are various numerical techniques used to solve Maxwell's equations. This thesis is focused on the Method of Moments and an extensive description of it is given in Chapter 3. However many techniques for solving the Partial Differential Equations (PDE) system described by Maxwell's equations are available. The most popular ones include the Finite-

Difference Time Domain (FDTD) and Finite Element Method (FEM) which are exact full wave methods. A brief description of the FDTD and FEM is presented in the following sections.

2.2.1 Finite Difference Time-Domain Method

The Finite-Difference Time-Domain (FDTD) method developed by Yee [23] is a technique that is used to solve the partial differential equations (PDE) associated with Maxwell's equations [4]. The FDTD algorithm is quite popular due to its simplicity and flexibility [24]. The FDTD requires the solution space to be divided into a uniform mesh composed of cells, where the magnetic and electric field are defined over each cell as can be seen in Figure (2.1). In the FDTD approach no matrix solution is required. It uses a different technique referred to as leapfrogging. The leapfrog technique assumes that the electric and magnetic fields are staggered in space at one half-cell apart and in time at one half-step apart [25]. Figure (2.2) presents a schematic description of the leapfrogging technique, where $\mathbf{E}_{n-1}$ is the electric field at step $n-1$ and $\mathbf{H}_{n-\frac{1}{2}}$ is the magnetic field at step $n-\frac{1}{2}$. Both $\mathbf{E}_{n-1}$ and $\mathbf{H}_{n-\frac{1}{2}}$ are used in order to compute $\mathbf{E}_n$. Next $\mathbf{H}_{n-\frac{1}{2}}$ and $\mathbf{E}_n$ are used in order to compute $\mathbf{H}_{n+\frac{1}{2}}$. This process is performed until a solution is obtained for each time step. This mechanism allows a direct solution of the fields for each particular instant in time offering second-order accuracy in both time and space. Another important feature of the FDTD method is that it offers solution for a wide variety of scattering and coupling problems [3]. A frequency dependent variation of FDTD is presented in [26] which can be applied to problems of scattering from frequency-dependent materials.

The FDTD method is one of the simplest numerical techniques for solving Maxwell's equations, however its effectiveness is highly dependent on the accuracy of the numerical modeling of the primary source, the precise field extension formulation and efficient mesh truncation, particularly when used in Electromagnetic Interference/Electromagnetic Compatibility (EMI/EMC) problems. When solving EMI/EMC problems the source of energy plays a very important role in calculating the emitted radiation. Therefore it has to be integrated into the model so that it follows as closely as possible the actual physical coupling

[27]. For open region radiation EMI/EMC problems, the solution domain would be infinite and therefore impossible to discretise. Thus the mesh has to be truncated to a finite size whereby an appropriate mesh truncation formulation is defined on the boundaries of the domain that is to be solved. These boundaries should be chosen as close as possible to the radiating structure in order to minimise computational effort.

When the far fields are to be calculated, the FDTD requires a very high computational effort. Field Extension algorithms are employed instead. The Field Extension techniques are based on finding magnetic and electric currents on imaginary paths that enclose both the primary and the secondary radiation sources [4; 28; 29; 30; 31; 32; 33].

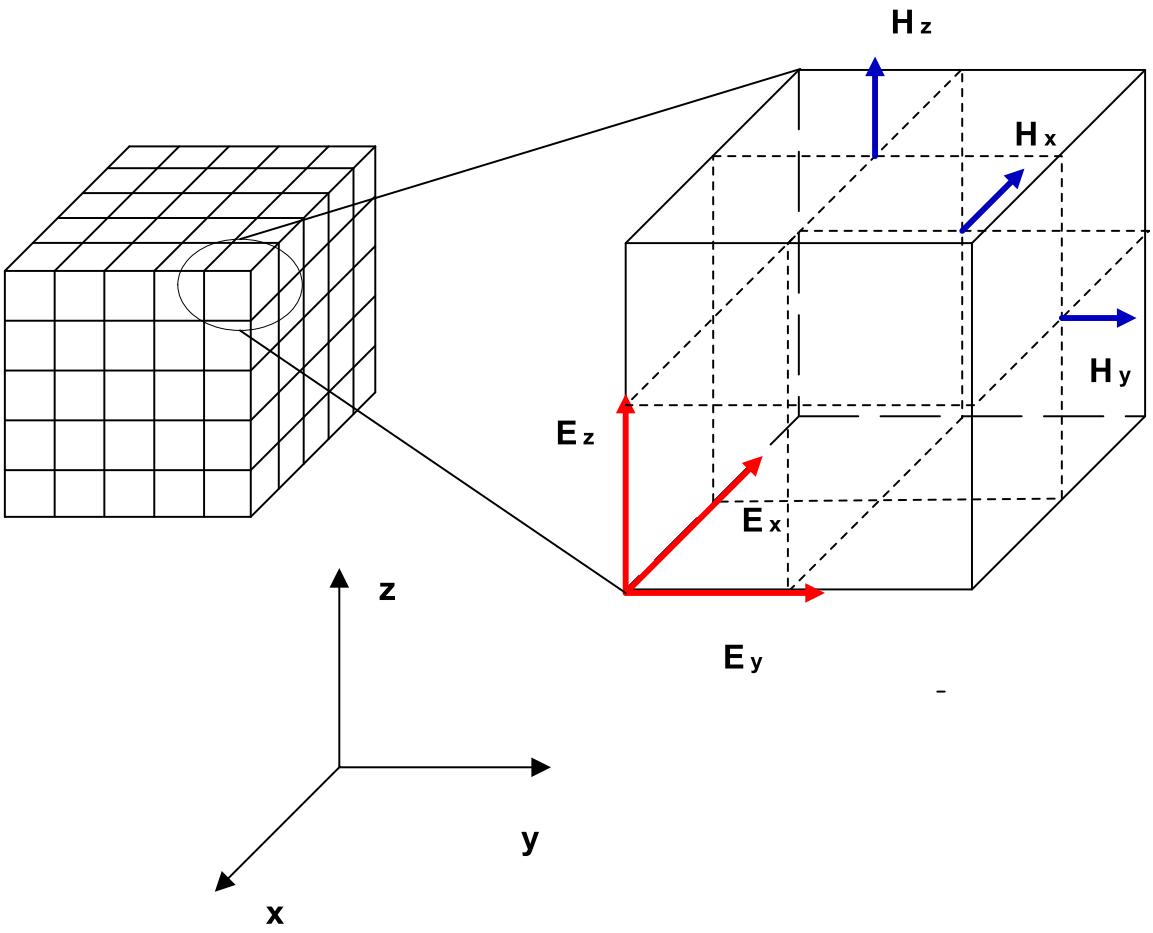

Figure 2.1: The FDTD (Yee) cell

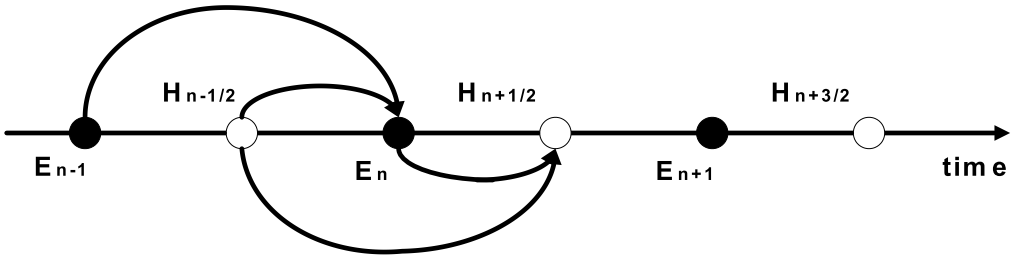

Figure 2.2: The leapfrog algorithm used in the FDTD method

2.2.2 Finite Element Method

The Finite Element Method (FEM) is another numerical technique used to solve Partial Differential Equations (PDEs). This technique is based on the conversion of the PDEs into matrix equations. The complicated scattering domain can be subdivided into a finite number of regions [34]. These elements are highly flexible patches, therefore allowing the analysis of extremely complicated scattering geometries. They allow local approximation of field quantities inside the volume enclosed by the elements points. The FEM uses different elements depending on the particular physical characteristics of the scatterer. Hence it is a mixed-basis formulation. It uses vector (edge) basis functions for transverse field components and scalar (nodal) basis functions for angular components. Another important advantage over the Method of Moments formulation is that the FEM has the same formulation for conducting, homogeneous and inhomogeneous dielectrics. The FEM technique does not require any modifications due to geometrical properties of the scatterers.

The resulting system equations are sparse, however the order of the resultant linear system is large, due to the fact that quantities have to be defined throughout the actual scattering structure and the surrounding volume. When using the Finite Element method it must be ensured that it is free of spurious modes. When FEM is applied to open-region domains the use of appropriate absorbing boundary conditions (ABCs) is critical. Partial Differential Equations Solvers, including FEM and FDTD, have a drawback incurred by the grid dispersion error, which can be rectified by increasing the mesh density. However

this generates a higher system size, therefore increasing the computational effort [4; 35; 28; 30; 36].

A variation of the classical FEM method is the FEM/IE technique which combines both the finite element and the Integral Equation approaches. The FEM/IE method is based on the idea of transforming the original problem into exterior and interior problems, where the interior problem, or the inhomogeneous body will be modeled using the FEM approach, whereas the exterior problem is solved using the IE approach [37; 38; 39].

2.3 Ray Optical Methods

Time or frequency domain numerical methods require a high level of discretisation with at least ten mesh cells per wavelength, resulting in a very large number of mesh points. This is necessary in order to achieve good accuracy in the final result. However, when very high frequency scattering problems are considered it becomes difficult to solve them using such finely meshed grids. However at high frequencies the behaviour of the fields becomes well approximated by asymptotic methods such as the Geometrical Theory of Diffraction (GTD) and Uniform Theory of Diffraction (UTD) [40].

Geometrical Optics (GO), also referred to as *ray optics*, is an approximate high-frequency method used to determine the wave propagation for incident, reflected and refracted fields [2; 41]. The GO concepts have been formulated by establishing a rigorous connection between Maxwell's equations and general geometrical quantities. This is achieved by deriving the wave equation from Maxwell's equation with the assumptions that the permeability is constant in space, whereas the permittivity, hence the refractive index, varies only slightly over distances comparable with the radiation wavelength. The most important property of the high-frequency field is the assumption that the wave is locally plane, which allows the simplification of the reflected and refracted waves expressions. This leads to much simpler equations for polarization, amplitude, phase and propagation paths [42]. In order to achieve more accurate results the Geometrical Theory of Diffraction (GTD) was introduced. It accounts for diffracted rays whose paths are determined using

a Fermat's principle generalization [42; 43]. However the GTD does not account for the rays diffracted into the shadow boundaries. In order to compensate for this issue the Uniform Theory of Diffraction (UTD) was developed by Kouyoumjian and Pathak [44]. They managed to bound the diffracted fields across the shadow boundaries by multiplying the diffraction coefficients by a transition function which allows a more precise calculation of the fields in the transition region.

Using UTD for practical problems involves first finding the rays. Ray tracing can be employed for this purpose. Ray tracing is an approximate method which can be used at very high frequencies where the size of the scatterer is much larger compared to the wavelength of the problem. It represents the process of finding all direct, reflected, transmitted and diffracted wave paths from the transmitter to the receiver. The received fields are then calculated by combining the contributions from all the rays, each contribution being calculated according to UTD [45].

Shooting and Bouncing Rays (SBR) is another technique similar to ray tracing, where a large number of rays are sent from the transmitter source point in equally spaced directions, and the field at each point is the sum of the fields from all rays passing through that point. The reflections, diffractions and transmissions of each ray are calculated using UTD [46].

Chapter 3

Integral Equation formulation and the Method of Moments

The Integral Equation (IE) formulation is obtained using Green's functions and the surface equivalence principle. In contrast to the PDE based methods it generates a smaller number of unknowns and is extremely flexible in terms of the geometry of the scatterer. The resulting matrix equations are dense. However various fast solvers can be efficiently used in order to build up a solution for the unknown current density induced on the surface of the scatterer [2; 4]. The IE formulation varies depending on the scattering surface. The Volume Integral Equation is applied when the scatterer is inhomogeneous, whereas for a homogeneous scatterer a Surface Integral Equation formulation is employed. The Coupled Integral Equation formulation and the Combined Field Integral Equation Formulation can be applied to 2D and 3D homogeneous dielectric scattering problems [3].

An Integral Equation Formulation for a scattering problem is posed in terms of an unknown current density. A numerical technique referred to as the Method of Moments (MoM) is then used in order to convert the continuous equation to a matrix equation [3; 2; 8; 4; 9; 47]. The first step in the MoM procedure is to discretise the surface of the scatterer into a series of wire segments or patches much smaller than the wavelength. Basis functions are then associated with these patches. These act as expansion functions

for the unknown current. The Method of Moments is highly efficient due to the fact that it discretises only the physical structure of the scattering object. It therefore involves fewer unknowns than the DE formulation. Another attraction of the IE formulation is the fact that it imposes the radiation condition, therefore not requiring local boundary conditions which are imperative in the DE formulation [4]. The MoM is most commonly a frequency-domain technique which can calculate the unknown currents over a single frequency or a narrow band of frequencies [28].

In order to develop the IE formulation a general scattering problem is first described in Section 3.1.1. The Volume Equivalence and Surface Equivalence Principles, which are used to simplify the original scattering problem, are then described in Section 3.1.2 and 3.1.3. The IE formulation for perfect electric conductors is presented in Section 3.1.4, followed by the IE formulation for homogeneous dielectrics both in 2D and 3D in Section 3.1.5. The MoM for these scattering problems is discussed in Sections 3.2.1-3.2.4.

3.1 Integral Equation Formulation

3.1.1 Scattering Problem

A general scattering problem is represented in Figure (3.1). An arbitrary homogeneous object is considered. It is illuminated by a primary source located outside the scatterer that produces incident fields $\bar{\mathbf{E}}^i$ and $\bar{\mathbf{H}}^i$. $\bar{\mathbf{E}}^s$ and $\bar{\mathbf{H}}^s$ are the fields scattered from the object. Equations (3.1-3.2) represent a mathematical description of the scattering problem:

$$\bar{\mathbf{E}} = \bar{\mathbf{E}}^i + \bar{\mathbf{E}}^s \tag{3.1}$$

$$\bar{\mathbf{H}} = \bar{\mathbf{H}}^i + \bar{\mathbf{H}}^s \tag{3.2}$$

where $\bar{\mathbf{E}}^i$ and $\bar{\mathbf{H}}^i$ denote the incident field, $\bar{\mathbf{E}}^s$ and $\bar{\mathbf{H}}^s$ represent the scattered field. The incident fields in the close proximity of the scatterer, away form the source, have to satisfy the Helmholtz equations:

$$\nabla^2\bar{\mathbf{E}}^i + k^2\bar{\mathbf{E}}^i = 0 \tag{3.3}$$

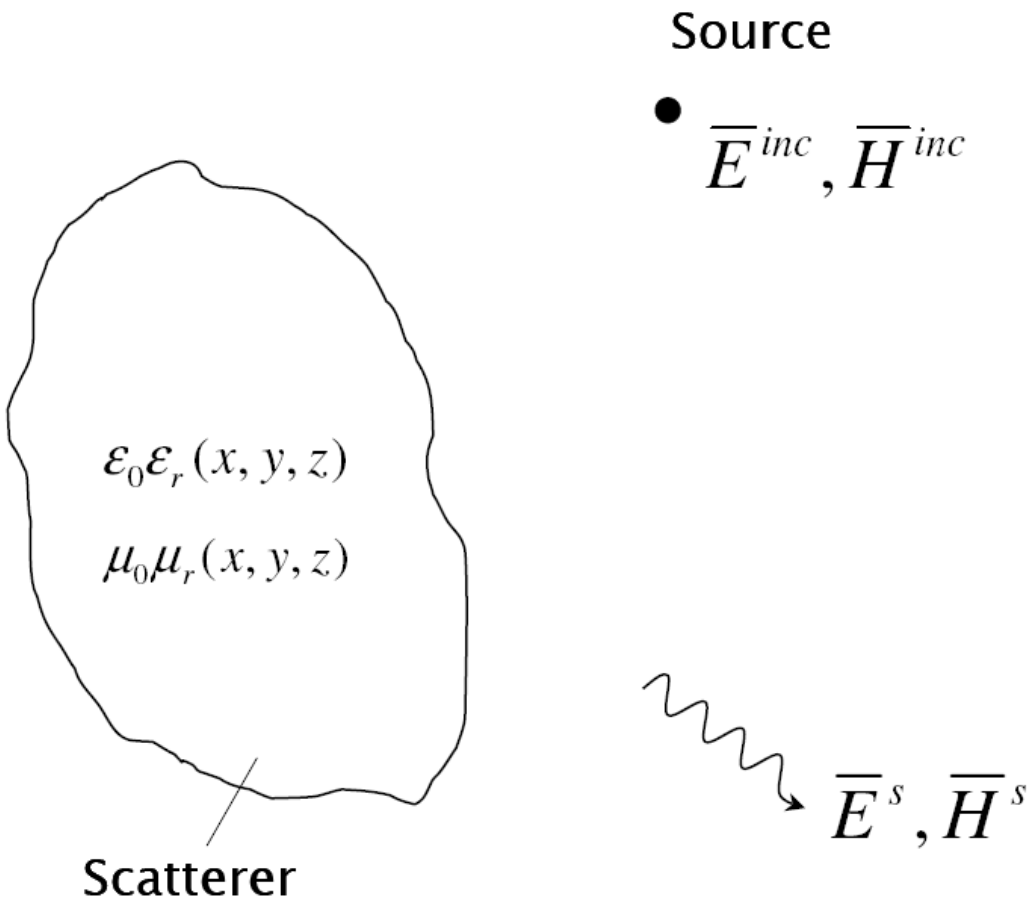

Figure 3.1: The scattering problem

$$\nabla^2 \bar{\mathbf{H}}^i + k^2 \bar{\mathbf{H}}^i = 0 \tag{3.4}$$

Expressions for the scattered fields are derived after introducing the Volume Equivalence Principle in Section 3.1.2.

3.1.2 Volume Equivalence Principle

Consider a free-space region that contains an arbitrary object described by relative permittivity $\varepsilon_r(x, y, z)$ and relative permeability $\mu_r(x, y, z)$ within that region. Assume that the object is illuminated by an incident field. Then the previously stated Maxwell's equations (2.17-2.20) can be rewritten as follows describing the fields in the vicinity of the object [3]:

$$\nabla \times \bar{\mathbf{E}} = -j\omega\mu_0\mu_r \bar{\mathbf{H}} \tag{3.5}$$

$$\nabla \times \bar{\mathbf{H}} = j\omega\varepsilon_0\varepsilon_r \bar{\mathbf{E}} \tag{3.6}$$

$$\nabla \cdot (\varepsilon_0\varepsilon_r \bar{\mathbf{E}}) = 0 \tag{3.7}$$

$$\nabla \cdot (\mu_0\mu_r \bar{\mathbf{H}}) = 0 \tag{3.8}$$

In order to derive the integral equation, the original problem is converted into an equivalent one by replacing the dielectric and magnetic material by equivalent currents and charges [3]. Assume a free space environment where the source is represented by $\bar{\mathbf{J}}$ and $\bar{\mathbf{K}}$ generating the fields $\bar{\mathbf{E}}$ and $\bar{\mathbf{H}}$. The Maxwell's equations for this scenario are formulated as:

$$\nabla \times \bar{\mathbf{E}} = -j\omega\mu_0 \bar{\mathbf{H}} - \bar{\mathbf{K}} \tag{3.9}$$

$$\nabla \times \bar{\mathbf{H}} = j\omega\varepsilon_0 \bar{\mathbf{E}} + \bar{\mathbf{J}} \tag{3.10}$$

$$\nabla \cdot \left(\varepsilon_0 \bar{\mathbf{E}}\right) = \rho_e \tag{3.11}$$

$$\nabla \cdot \left(\mu_0 \bar{\mathbf{H}}\right) = \rho_m \tag{3.12}$$

The equivalent electric and magnetic densities $\bar{\mathbf{J}}$ and $\bar{\mathbf{K}}$ are defined as:

$$\bar{\mathbf{K}} = j\omega\mu_0\left(\mu_r - 1\right)\bar{\mathbf{H}} \tag{3.13}$$

$$\bar{\mathbf{J}} = j\omega\varepsilon_0\mu_0\left(\varepsilon_r - 1\right)\bar{\mathbf{E}} \tag{3.14}$$

$$\rho_e = \varepsilon_0\varepsilon_r\bar{\mathbf{E}}\cdot\nabla\left(\frac{1}{\varepsilon_r}\right) \tag{3.15}$$

$$\rho_m = \mu_0\mu_r\bar{\mathbf{H}}\cdot\nabla\left(\frac{1}{\mu_r}\right) \tag{3.16}$$

where $\mu_r = \frac{\mu}{\mu_0}$ and $\varepsilon_r = \frac{\varepsilon}{\varepsilon_0}$. Equations (3.9) to (3.12) describe the fields due to sources that radiate in free space. Solving the problem of a source radiating in free space is significantly easier then solving the initial equations (3.5) - (3.8) which represent the scattering problem in an inhomogeneous environment, as potential theory can be used.

The scattered fields can now be obtained from solving the following equations, noting that $\bar{\mathbf{J}}$ and $\bar{\mathbf{K}}$ represent the equivalent densities described by Equations (3.13-3.14):

$$\nabla^2\bar{\mathbf{E}}^s + k^2\bar{\mathbf{E}}^s = j\omega\mu_0\bar{\mathbf{J}} - \frac{\nabla\nabla\cdot\bar{\mathbf{J}}}{j\omega\varepsilon_0} + \nabla\times\bar{\mathbf{K}} \tag{3.17}$$

$$\nabla^2\bar{\mathbf{H}}^s + k^2\bar{\mathbf{H}}^s = -\nabla\times\bar{\mathbf{J}} + j\omega\varepsilon_0\bar{\mathbf{K}} - \frac{\nabla\nabla\cdot\bar{\mathbf{K}}}{j\omega\mu_0} \tag{3.18}$$

The solution to Equations (3.17-3.18) can be expressed in terms of the magnetic and electric vector potentials $\bar{\mathbf{A}}$ and $\bar{\mathbf{F}}$ [3]:

$$\bar{\mathbf{E}}^s = \frac{\nabla\nabla\cdot\bar{\mathbf{A}} + k^2\bar{\mathbf{A}}}{j\omega\varepsilon_0} - \nabla\times\bar{\mathbf{F}} \tag{3.19}$$

$$\bar{\mathbf{H}}^s = \nabla\times\bar{\mathbf{A}} + \frac{\nabla\nabla\cdot\bar{\mathbf{F}} + k^2\bar{\mathbf{F}}}{j\omega\mu_0} \tag{3.20}$$

The vector potentials $\bar{\mathbf{A}}$ and $\bar{\mathbf{F}}$ satisfy the following equations:

$$\nabla^2\bar{\mathbf{A}} + k^2\bar{\mathbf{A}} = -\bar{\mathbf{J}} \tag{3.21}$$

$$\nabla^2\bar{\mathbf{F}} + k^2\bar{\mathbf{F}} = -\bar{\mathbf{K}} \tag{3.22}$$

where $k^2 = \omega^2 \mu_0 \varepsilon_0$. The electric and magnetic scattered field can now be formulated as:

$$\bar{\mathbf{E}}^s = -j\omega\mu_0\bar{\mathbf{A}} - j\frac{1}{\omega\varepsilon_0}\nabla(\nabla\cdot\bar{\mathbf{A}}) - \nabla\times\bar{\mathbf{F}} \tag{3.23}$$

$$\bar{\mathbf{H}}^s = \nabla\times\bar{\mathbf{A}} - j\omega\varepsilon_0\bar{\mathbf{F}} - j\frac{1}{\omega\mu_0}\nabla(\nabla\cdot\bar{\mathbf{F}}) \tag{3.24}$$

Using the three-dimensional Green's function $G = \frac{e^{-jk|\bar{r}|}}{4\pi|\bar{r}|}$ the vector potentials can be expressed as:

$$\bar{\mathbf{A}} = \bar{\mathbf{J}} * G \tag{3.25}$$

$$\bar{\mathbf{F}} = \bar{\mathbf{K}} * G \tag{3.26}$$

which leads to:

$$\bar{\mathbf{A}}(\bar{r}) = \mu_0 \iiint \bar{\mathbf{J}}(\bar{r}^{'})\frac{e^{jk|\bar{r}-\bar{r}^{'}|}}{4\pi|\bar{r}-\bar{r}^{'}|}d\bar{r}^{'} \tag{3.27}$$

$$\bar{\mathbf{F}}(\bar{r}) = \varepsilon_0 \iiint \bar{\mathbf{K}}(\bar{r}^{'})\frac{e^{jk|\bar{r}-\bar{r}^{'}|}}{4\pi|\bar{r}-\bar{r}^{'}|}d\bar{r}^{'} \tag{3.28}$$

3.1.3 Surface Equivalence Principle

The surface equivalence principle is enforced in order to simplify the problems involving homogeneous scatterers. According to the surface equivalence principle the dielectric and the magnetic materials are replaced with mathematically equivalent sources placed on the scattering surface which radiate in homogeneous space

Consider two regions of space separated by a surface S, as it can be seen in Figure (3.2). The first is free space described by permittivity ε_0 and permeability μ_0. $\bar{\mathbf{J}}_1$ and $\bar{\mathbf{K}}_1$ represent the source radiating fields $\bar{\mathbf{E}}_1$ and $\bar{\mathbf{H}}_1$. By applying the surface equivalence principle, the original source is removed and replaced by an equivalent one. This is presented in Figure (3.3), where the original problem has been replaced with an equivalent exterior problem where the fields throughout the homogeneous region are now null. The equivalent sources $\mathbf{J}_s$ and $\mathbf{K}_s$ can be now represented in terms of the outward normal vector $\hat{n}$ and

the original fields $\bar{\mathbf{E}}_1$ and $\bar{\mathbf{H}}_1$:

$$\mathbf{J}_s = \hat{n} \times \bar{\mathbf{H}}_1 \tag{3.29}$$

$$\mathbf{K}_s = -\hat{n} \times \bar{\mathbf{E}}_1 \tag{3.30}$$

The introduction of equivalent sources simplifies the problem. However it does not solve it and the unknown scattered fields as well as the equivalent sources $\bar{\mathbf{J}}_s$ $\bar{\mathbf{K}}_s$ still remain to be found. Now the equations (3.9-3.12) have to be solved using the equivalent surface currents in (3.29-3.30) and the following continuity equations:

$$\rho_e = \frac{-1}{j\omega} \nabla_s \cdot \bar{\mathbf{J}}_s \tag{3.31}$$

$$\rho_m = \frac{-1}{j\omega} \nabla_s \cdot \bar{\mathbf{K}}_s \tag{3.32}$$

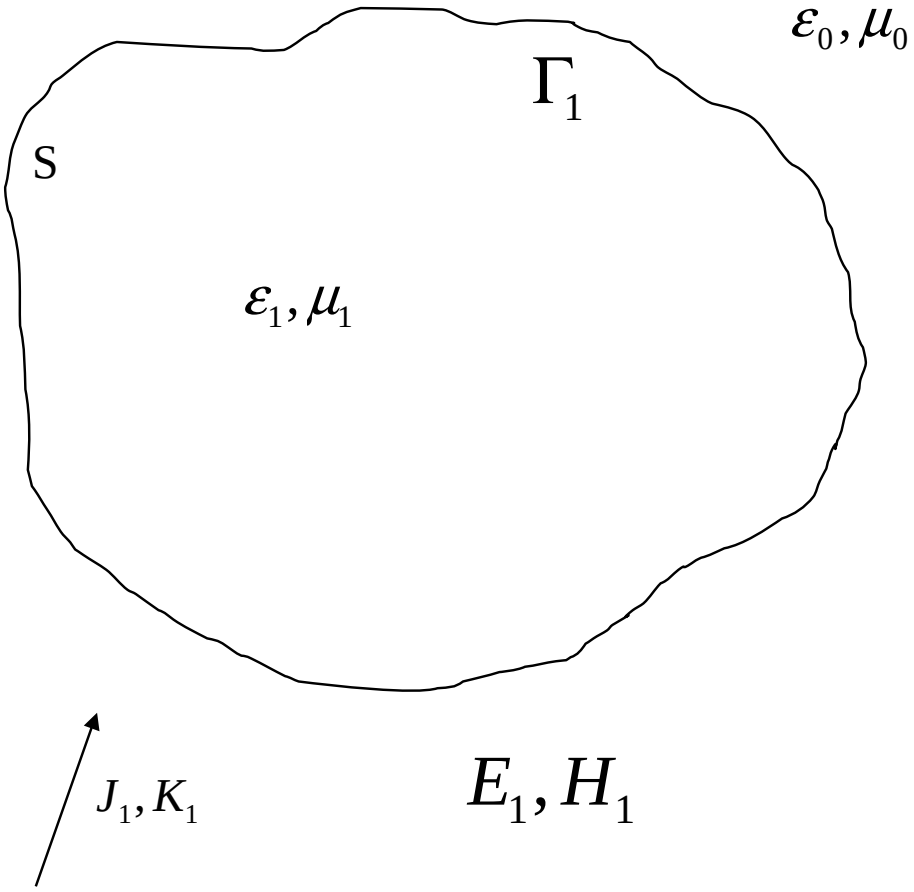

Figure 3.2: Surface Equivalence Principle. Original Problem

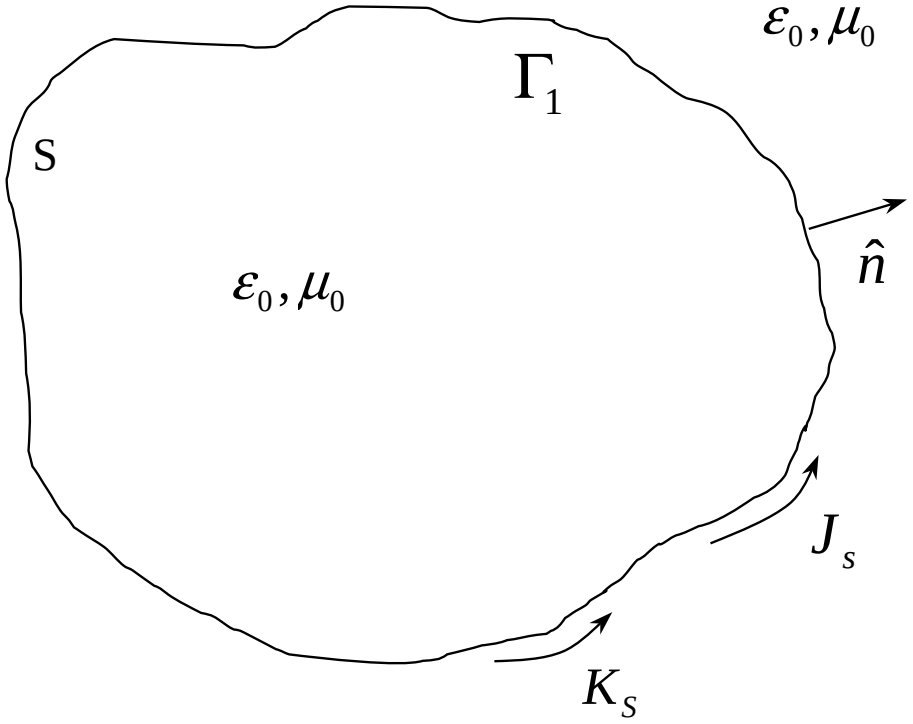

Figure 3.3: Surface Equivalence Principle. Equivalent Problem

3.1.4 Integral Equation for Perfect Electric Conductors

Consider a perfect electric conductor (PEC) illuminated by a source as shown in Figure (3.4). In order to formulate the Integral Equation formulation for problems of wave scattering from PECs the boundary conditions which state that the total tangential electric field on a PEC surface is equal to 0 is used [2]. Therefore $\bar{\mathbf{K}}_s = 0$. Hence, noting that the t subscript indicates the tangential components of the corresponding fields, we can write.

$$\bar{\mathbf{E}}_t = \bar{\mathbf{E}}_t^i + \bar{\mathbf{E}}_t^s \tag{3.33}$$

$$\bar{\mathbf{E}}_t^i = -\bar{\mathbf{E}}_t^s \tag{3.34}$$

An equivalent electric current $\bar{\mathbf{J}}_s$ is induced on the scattering surface by the incident field. The scattered field can then be expressed using Equations (3.19-3.23) assuming that the incident field is known:

$$\bar{\mathbf{E}}_t^s = -j\omega\mu_0\bar{\mathbf{A}} - j\frac{1}{\omega\varepsilon_0}\nabla(\nabla\cdot\bar{\mathbf{A}}) \tag{3.35}$$

Substituting the vector potential $\bar{\mathbf{A}}$ expression given by (3.27) in Equation (3.35) the resulting scattered field $\bar{\mathbf{E}}_t^s$ can be now written in the form of an integral:

$$\bar{\mathbf{E}}_t^s = -j\frac{\eta}{k}\left[k^2\iint\bar{\mathbf{J}}_s(\bar{r}^{'})\frac{e^{jk|\bar{r}-\bar{r}^{'}|}}{4\pi|\bar{r}-\bar{r}^{'}|}d\bar{r}^{'} + \nabla\iint\nabla^{'}\cdot\bar{\mathbf{J}}_s(\bar{r}^{'})\frac{e^{jk|\bar{r}-\bar{r}^{'}|}}{4\pi|\bar{r}-\bar{r}^{'}|}d\bar{r}^{'}\right] \tag{3.36}$$

where $\eta = \sqrt{\frac{\mu_0}{\varepsilon_0}}$. Applying Equation (3.34) the incident tangential field on the PEC surface can now be expressed as:

$$\bar{\mathbf{E}}_t^i = j\frac{\eta}{k}\left[k^2\iint\bar{\mathbf{J}}_s(\bar{r}^{'})\frac{e^{jk|\bar{r}-\bar{r}^{'}|}}{4\pi|\bar{r}-\bar{r}^{'}|}d\bar{r}^{'} + \nabla\iint\nabla^{'}\cdot\bar{\mathbf{J}}_s(\bar{r}^{'})\frac{e^{jk|\bar{r}-\bar{r}^{'}|}}{4\pi|\bar{r}-\bar{r}^{'}|}d\bar{r}^{'}\right] \tag{3.37}$$

.

Equation (3.37) expresses the current density $\bar{\mathbf{J}}_s$ in terms of the incident field and is referred to as *Electric Field Integral Equation* (EFIE). The EFIE given by Equation (3.37) is employed in Chapter 5 for solving the problem of electromagnetic wave scattering from

a wedge composed of 2 PEC plates.

An alternative formulation is the *Magnetic Field Integral Equation* (MFIE) which is expressed in terms of the incident magnetic field at a infinitesimally small distance outside the scatterer (S^+).

$$\hat{n} \times \bar{\mathbf{H}}^i = \bar{\mathbf{J}}_s - \{\hat{n} \times \nabla \times \bar{\mathbf{A}}\}_{S^+} \tag{3.38}$$

Again one must solve for current density $\bar{\mathbf{J}}_s$.

Equation (3.37) is the IE for a problem of electromagnetic wave scattering from a 3D PEC. In order to simplify it for a 2D case consider a 2D PEC problem where the incident wave is TM_z. For a TM_z incident wave the only electric field component present is E_z and the current J_z. The EFIE Equation 3.37 simplifies to:

$$E_z^i(t) = jk\eta A_z(t) \tag{3.39}$$

where

$$A_z(t) = \int J_z(t^{'}) \frac{1}{4j} H_0^{(2)}(kR) dt^{'} \tag{3.40}$$

where $R = \sqrt{[x(t) - x(t^{'})]^2 + [y(t) - y(t^{'})]^2}$ and t is a simple variable that parameterises the surface of the scatterer. $H_0^{(2)}(kR)$ is the Hankel function of second kind of order 0.

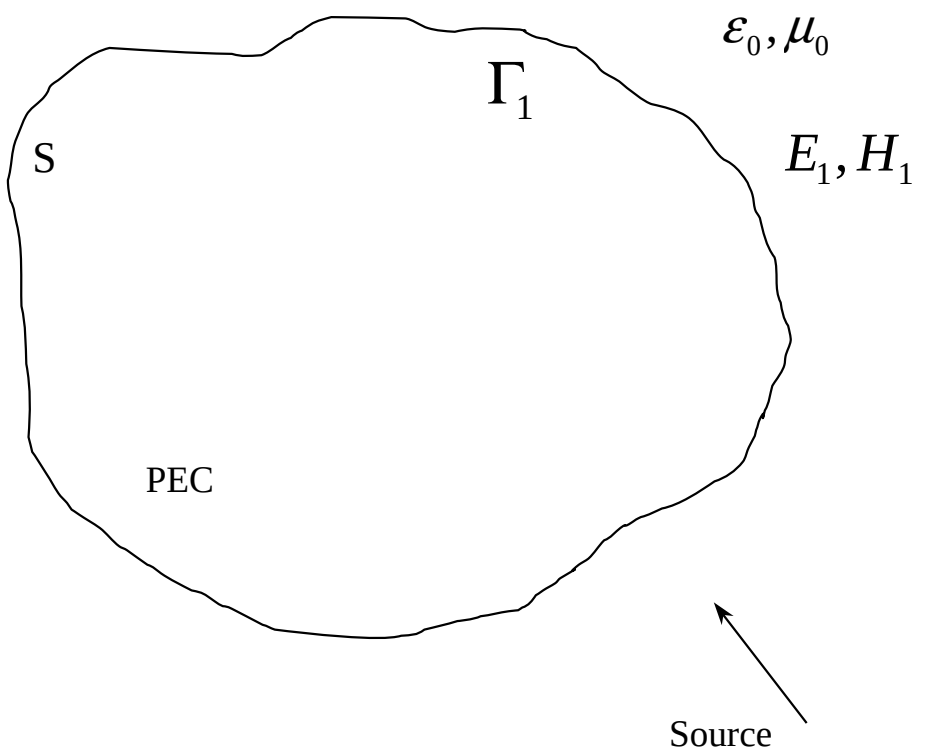

Figure 3.4: Surface Equivalence Principle used for Electric Field Integral Equation. Original Problem

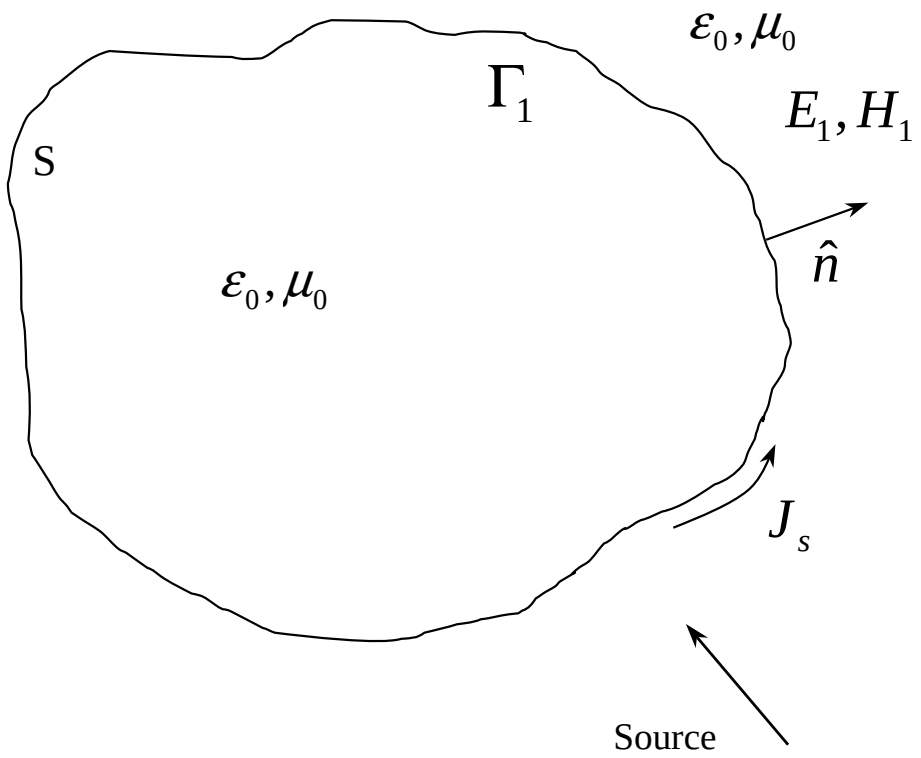

Figure 3.5: Surface Equivalence Principle used for Electric Field Integral Equation. Equivalent Problem.

3.1.5 Integral Equation formulation for homogeneous dielectric objects

In order to formulate the Integral Equation for homogeneous dielectric scatterers the surface equivalence principle is employed. Two different regions are considered. The first region is free space and the second region is the homogeneous scattering object. $\bar{\mathbf{E}}_1$ and $\bar{\mathbf{H}}_1$ are the fields within free space. The homogeneous scatterer is described by constant relative permittivity ε_r and relative permeability μ_r, and $\bar{\mathbf{E}}_2$ and $\bar{\mathbf{H}}_2$ are the fields within it. After applying the surface equivalence principle we obtain two different problems: an equivalent exterior problem and an equivalent interior one.

The equivalent sources $\bar{\mathbf{J}}_1$ and $\bar{\mathbf{K}}_1$ associated with the equivalent exterior problem are given by:

$$\bar{\mathbf{J}}_1 = \hat{n} \times \bar{\mathbf{H}}_1 \tag{3.41}$$

$$\bar{\mathbf{K}}_1 = \bar{\mathbf{E}}_1 \times \hat{n} \tag{3.42}$$

The equivalent sources $\bar{\mathbf{J}}_2$ and $\bar{\mathbf{K}}_2$ associated with the equivalent interior problem are:

$$\bar{\mathbf{J}}_2 = (-\hat{n}) \times \bar{\mathbf{H}}_2 \tag{3.43}$$

$$\bar{\mathbf{K}}_2 = \bar{\mathbf{E}}_2 \times (-\hat{n}) \tag{3.44}$$

where $\bar{\mathbf{J}}_1 = -\bar{\mathbf{J}}_2$ and $\bar{\mathbf{K}}_1 = -\bar{\mathbf{K}}_2$. In both equivalent exterior and interior problems $\hat{n}$ represents the normal vector pointing out of the scatterer.

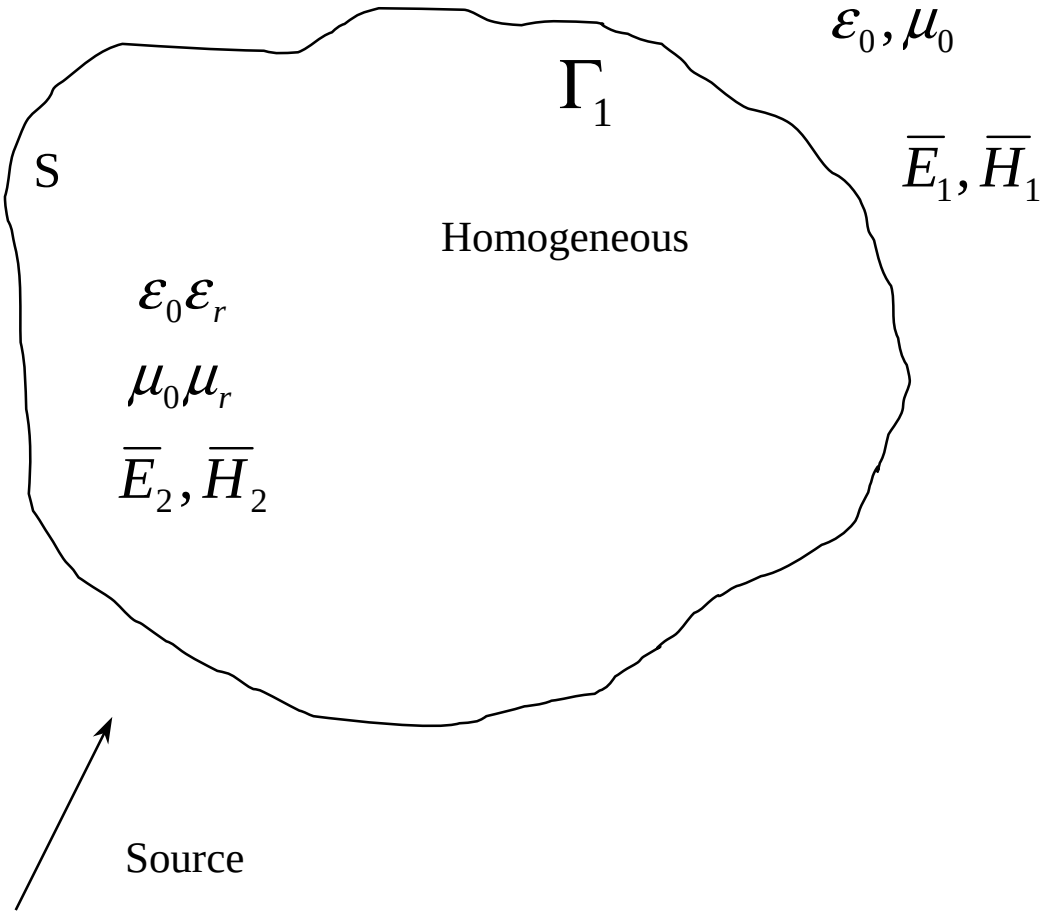

Figure 3.6: Homogeneous dielectric scatterer. Original problem

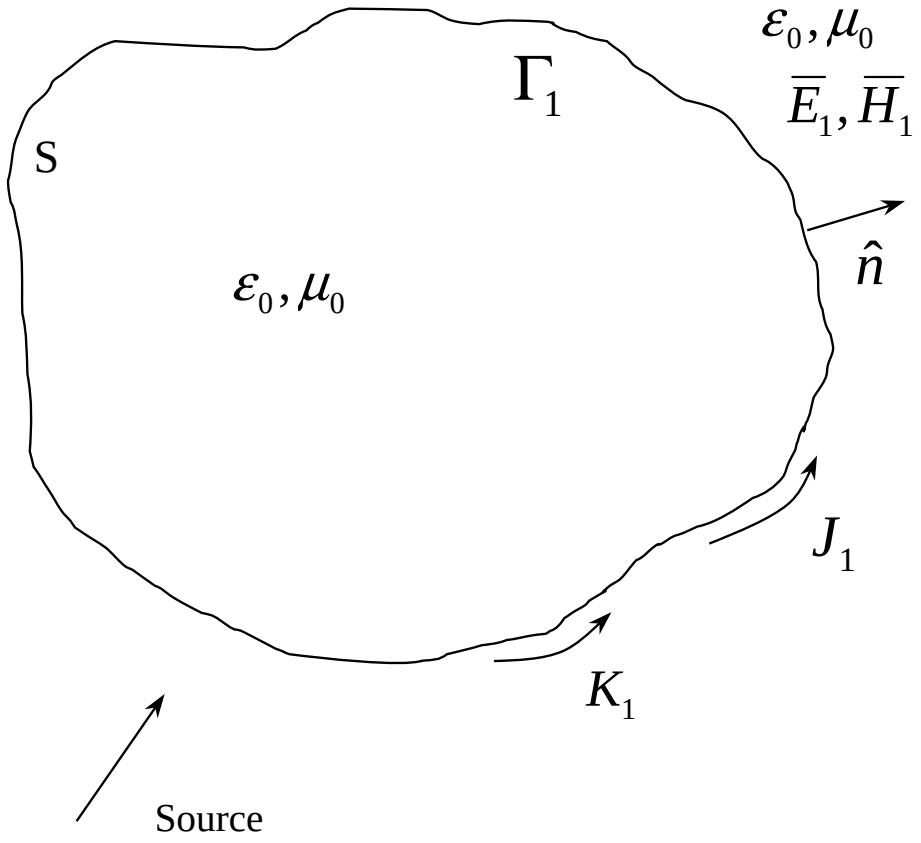

Figure 3.7: Equivalent Exterior Problem associated with a homogeneous dielectric scatterer

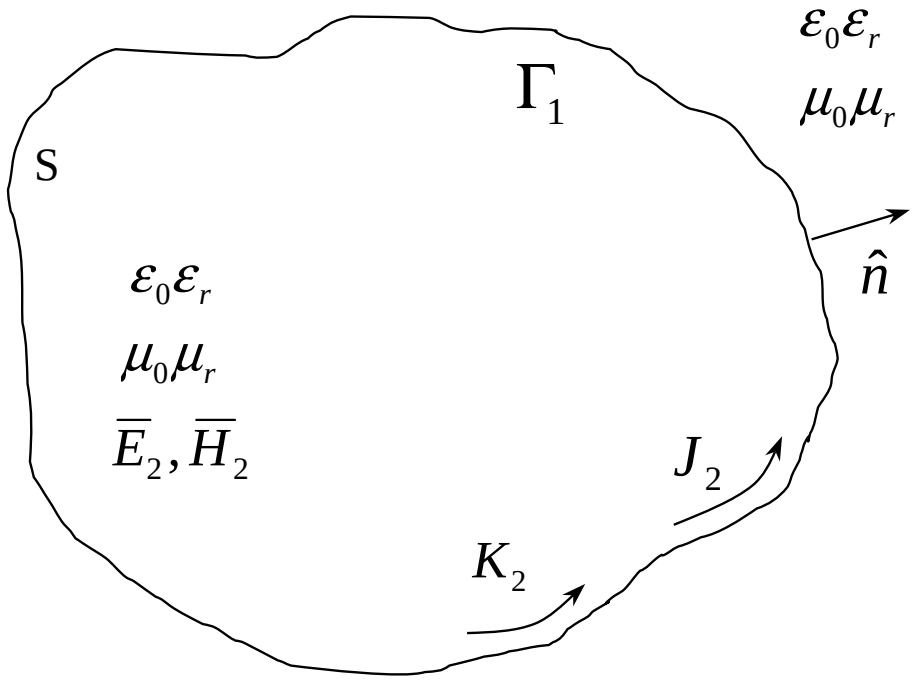

Figure 3.8: Equivalent Interior Problem associated with a homogeneous dielectric scatterer.

The equations (3.19) and (3.20) can now be combined with (3.41-3.44), leading to a set of equations that characterize the fields in the close proximity to the surface outside (S^+) the scatterer and inside (S^-) the scatterer. These are referred to as the Coupled Electric Field Integral Equations and are given by:

$$\hat{n} \times \bar{\mathbf{E}}^{inc} = -\bar{\mathbf{K}}_1 - \hat{n} \times \{\frac{\eta_0}{jk_0}(\nabla\nabla \cdot \bar{\mathbf{A}} + k_0^2\bar{\mathbf{A}}) - \nabla \times \bar{\mathbf{F}}\}_{S^+} \tag{3.45}$$

$$0 = \bar{\mathbf{K}}_1 - \hat{n} \times \{\frac{\eta_d}{jk_d}(\nabla\nabla \cdot \bar{\mathbf{A}}_d + k_d^2\bar{\mathbf{A}}_d) - \nabla \times \bar{\mathbf{F}}_d\}_{S^-} \tag{3.46}$$

where $k_0 = \omega\sqrt{\mu_0\varepsilon_0}$ and $k_d = \omega\sqrt{\mu\varepsilon}$ are the wavenumbers for free space medium and the dielectric scatterer respectively. $\eta_0 = \sqrt{\frac{\mu_0}{\varepsilon_0}}$ and $\eta_d = \sqrt{\frac{\mu}{\varepsilon}}$ are the intrinsic impedances of the mediums. The vector potentials $\bar{\mathbf{A}}$ and $\bar{\mathbf{F}}$ are associated with the exterior problem, whereas $\bar{\mathbf{A}}_d$ and $\bar{\mathbf{F}}_d$ are associated with the dielectric scatterer:

$$\bar{\mathbf{A}} = \bar{\mathbf{J}}_1 * \frac{e^{-jk_0r}}{4\pi r} \tag{3.47}$$

$$\bar{\mathbf{F}} = \bar{\mathbf{K}}_1 * \frac{e^{-jk_0r}}{4\pi r} \tag{3.48}$$

$$\bar{\mathbf{A}}_d = \bar{\mathbf{J}}_1 * \frac{e^{-jk_dr}}{4\pi r} \tag{3.49}$$

$$\bar{\mathbf{F}}_d = \bar{\mathbf{K}}_1 * \frac{e^{-jk_dr}}{4\pi r} \tag{3.50}$$

$$\tag{3.51}$$

An alternative integral equation formulation is the Coupled Magnetic Field Integral Equation:

$$\hat{n} \times \bar{\mathbf{H}}^{inc} = \bar{\mathbf{J}}_1 - \hat{n} \times \{\nabla \times \bar{\mathbf{A}} + \frac{\nabla\nabla \cdot \bar{\mathbf{F}} + k_0^2\bar{\mathbf{F}}}{jk_0\eta_0}\}_{S^+} \tag{3.52}$$

$$0 = -\bar{\mathbf{J}}_1 - \hat{n} \times \{\nabla \times \bar{\mathbf{A}}_d + \frac{\nabla\nabla \cdot \bar{\mathbf{F}}_d + k_d^2\bar{\mathbf{F}}_d}{jk_d\eta d}\}_{S^-} \tag{3.53}$$

The formulation described in Equations (3.45-3.46) is for a 3D scattering problem. In order to derive the 2D formulation of the Coupled EFIE consider a TM_z incident wave.

The Coupled EFIE can be simplified as:

$$E_z^{inc}(t) = K_t(t) + jk_0\mu_0 A_z^{(0)} + \{\frac{\partial F_y^{(0)}}{\partial x} - \frac{\partial F_x^{(0)}}{\partial y}\}_{S^+} \tag{3.54}$$

$$0 = -K_t(t) + jk_d\eta_d A_z^{(d)} + \{\frac{\partial F_y^{(d)}}{\partial x} - \frac{\partial F_x^{(d)}}{\partial y}\}_{S^-} \tag{3.55}$$

where

$$A_z^{(i)} = \int J_z(t^{'})\frac{1}{4j}H_0^{(2)}(k_i R)dt^{'} \tag{3.56}$$

$$\bar{F}_t^{(i)} = \int \hat{t}(t^{'})K_t(t^{'})\frac{1}{4j}H_0^{(2)}(k_i R)dt^{'} \tag{3.57}$$

$$R = \sqrt{[x(t) - x(t^{'})]^2 + [y(t) - y(t^{'})]^2} \tag{3.58}$$

t is a variable that parameterises the surface of the scatterer in the same manner as for the perfect electric conductor and $\hat{t}$ represents the unit vector tangent to the scatterer contour. This Coupled EFIE is used to describe the 2D homogeneous dielectric scattering problem in Chapters 6 and 7.

The coupled EFIE and MFIE have a drawback of being affected by interior resonances. In order to overcome this issue the Combined Field Integral Equation (CFIE) is introduced. By rearranging equations (3.45), (3.46), (3.52) and (3.53) the following expressions can be written for the exterior equivalent problem [3]:

$$\bar{\mathbf{K}} = -\hat{n} \times \bar{\mathbf{E}}^{inc} - \hat{n} \times \{\frac{\eta}{jk}(\nabla\nabla \cdot \bar{\mathbf{A}} + k^2\bar{\mathbf{A}}) - \nabla \times \bar{\mathbf{F}}\}_{S^+} \tag{3.59}$$

$$\bar{\mathbf{J}} = \hat{n} \times \bar{\mathbf{H}}^{inc} + \hat{n} \times \{\nabla \times \bar{\mathbf{A}} + \frac{\nabla\nabla \cdot \bar{\mathbf{F}} + k^2\bar{\mathbf{F}}}{jk_1\eta}\}_{S^+} \tag{3.60}$$

The interior problem can be formulated accordingly:

$$\bar{\mathbf{K}} = \hat{n} \times \{\frac{\eta_d}{jk_d}(\nabla\nabla \cdot \bar{\mathbf{A}}_d + k_d^2\bar{\mathbf{A}}_d) - \nabla \times \bar{\mathbf{F}}_d\}_{S^-} \tag{3.61}$$

$$\bar{\mathbf{J}} = -\hat{n} \times \{\nabla \times \bar{\mathbf{A}}_d + \frac{\nabla\nabla \cdot \bar{\mathbf{F}}_d + k_d^2 \bar{\mathbf{F}}_d}{jk_d\eta_d}\}_{S^-} \tag{3.62}$$

The CFIE formulations can be obtained from equations (3.59), (3.60), (3.61) and (3.62), which leads to [3]:

$$-\hat{n}\times\bar{\mathbf{E}}^{inc} = \hat{n}\times\{\frac{\eta}{jk}(\nabla\nabla\cdot\bar{\mathbf{A}} + k^2\bar{\mathbf{A}}) - \nabla\times\bar{\mathbf{F}}\}_{S^+} + \hat{n}\times\{\frac{\eta_d}{jk_d}(\nabla\nabla\cdot\bar{\mathbf{A}}_d + k_d^2\bar{\mathbf{A}}_d) - \nabla\times\bar{\mathbf{F}}_d\}_{S^-} \tag{3.63}$$

$$-\hat{n}\times\bar{\mathbf{H}}^{inc} = \hat{n}\times\{\nabla\times\bar{\mathbf{A}} + \frac{\nabla\nabla\cdot\bar{\mathbf{F}} + k^2\bar{\mathbf{F}}}{jk_1\eta}\}_{S^+} + \hat{n}\times\{\nabla\times\bar{\mathbf{A}}_d + \frac{\nabla\nabla\cdot\bar{\mathbf{F}}_d + k_d^2\bar{\mathbf{F}}_d}{jk_d\eta_d}\}_{S^-} \tag{3.64}$$

The Combined Field Integral Equation given in (3.63) and (3.64) is used in Chapter 8 in order to describe the problem of wave scattering from a 3D homogeneous dielectric sphere.

These formulations form the basis of solving the problem of computation of fields scattered from perfectly electrically conducting structures and homogeneous dielectric scatterers. The next step involves the discretisation of the continuous integral equation, using the Method of Moments approach.

3.2 Method of Moments

The Method of Moments (MoM) is a technique used to reduce the Integral Equations discussed in Sections 3.1.4-3.1.5 to discrete linear systems of equations that can be solved on a computer.

There are two main types of basis functions. One class involves subdividing the scattering surface with a fine mesh and associating a basis function with each patch of the mesh [48; 7]. The second type includes basis functions that do not require segmentation of the scattering surface and are defined over the entire scatterer.

For 2D problems the most common subdomain basis function is the pulse basis function. Piecewise linear or triangular basis functions are defined on two neighboring segments, and also overlap adjacent functions. This generates a smoother representation of the unknown current compared to the pulse basis function, however it requires a slightly higher computational effort. Another type of basis function is the wavelet basis function. They allow the creation of sparse matrices, therefore decreasing the computational effort [49].

In terms of discretisation approach two main types of discretisations were widely investigated: the wire-grid modelling and the patch modelling. When applying the wire-grid approach the surface of the scatterer is modelled using a mesh of wire segments short in terms of wavelength, assuming that the current densities are uniformly distributed across the surface of the wire. This method is applied to various conducting surfaces in [50] showing that it is quite simple to implement and is highly accurate in delivering far-field results including the radar cross section. However, the wire-grid modelling method has various limitations as was shown in [51] and is unsuitable for calculating surface currents.

In order to overcome these shortcomings, the patch modelling has been introduced instead. Various patch modelling techniques have been investigated. In [52] quadrilateral patches were employed in modelling the scattering surface, solving the scattering problem using the Magnetic Field Integral Equation (MFIE). The MFIE is restricted to a limited type of problems, being unsuitable for open bodies and infinitesimally thin conductors. The MoM using rectangular patches is applied to the EFIE in [53], showing that the surface

currents computed using this discretisation technique match the physical measurements. However, the square patch partitioning approach is limited in terms of the scattering geometry, being more suitable for flat objects that do not present irregularities. A triangular patch modelling approach of a perfectly conducting plate was investigated in [54], suggesting that this approach offers a higher degree of accuracy compared to square patches. This partitioning method was later generalised for arbitrary shaped open or closed 3D conducting objects by Rao, Wilton and Glisson in [8] and is referred to as the Rao-Wilton-Glisson (RWG) basis function technique. The testing functions employed in this case enforce the boundary conditions across the triangle centroids. Figure (3.10) depicts a PEC scatterer modeled using the triangular patches.

Other new basis functions have been investigated in recent times. Multiresolution (MR) basis functions associated with hierarchical meshes are discussed in [55]. MR basis functions represent linear combinations of the RWG functions and are shown to be very effective when analysing arbitrary geometries. MR basis functions have also been combined with Curvilinear RWG (CRWG) basis functions, which are defined over curvilinear triangular patches [56] allowing a higher level of accuracy.

Lagrangian basis functions have also received much attention lately [3; 57; 58; 59]. These are defined over curvilinear patches and are based on the development of Lagrange interpolation polynomials. These basis functions greatly simplify the evaluation of the integral. Another advantage is an easier meshing procedure.

Another class of basis function is the Characteristic Basis Function (CBF) which is defined on large domains of the scatterer. An extended version of the CBF is the Multilevel CBF (CBFM) [60]. Both the CBF and CBFM methods have the main purpose of reducing the size of the impedance matrix and are mostly used in solving extremely large scattering problems.

Dual basis functions [61] and Buffa-Christiansen basis function [62] are recently introduced basis functions, which are defined on polygons and polygon pairs, generating well conditioned matrices. Tong *et al.* suggested that these basis functions are better suited for dielectric scatterers, although they require a higher computational effort compared to the RWG [61].

In this work the basis functions employed are the pulse basis functions for 2D scattering problems and the RWG basis functions for 3D scattering problems.

General Description of MoM

Consider the equation involving the linear operator Z:

$$Zx = v \tag{3.65}$$

An approximate solution can be obtained for equation (3.65) so that:

$$x \cong \sum_{n=1}^{N} \alpha_n B_n \tag{3.66}$$

where $\{B_n\}$ represents basis functions defined on the domain of Z and the coefficients α_n are unknowns that are to be determined [3]. The residual of the linear equation is calculated by replacing Equation (3.66) in Equation (3.65) and is given by:

$$Z\left(\sum_{n=1}^{N} \alpha_n B_n\right) - v = \sum_{n=1}^{N} \alpha_n Z B_n - v \tag{3.67}$$

The MoM consists requires that the residual be orthogonal to a set of testing functions $T_1, \ldots, T_N$. This results in a matrix equation:

$$\mathbf{Z}\boldsymbol{\alpha} = \boldsymbol{\beta} \tag{3.68}$$

where the entires of $\mathbf{Z}$ have the form $Z_{mn} = \langle T_m, ZB_n \rangle$ and $\beta = \langle T_m, v \rangle$, where $\langle * \rangle$ denotes an inner product. This technique of obtaining the matrix equation (3.68) from the continuous linear equation (3.65) is known as the *Method of Moments* (MoM). Specific application of the MoM are provided in the following sections.

3.2.1 TM-Wave Scattering from 2D Perfect Electric Conductors

Figure (3.9(a)) shows a two dimensional perfect electrically conducting (PEC) scatterer illuminated by a TM_z source.

The EFIE associated with this problem is formulated in Section 3.1.4 and is given by

$$E_z^i(t) = jk\eta A_z(t) \tag{3.69}$$

where

$$A_z(t) = \int J_z(t^{'})\frac{1}{4j}H_0^{(2)}(kR)dt^{'} \tag{3.70}$$

where $R = \sqrt{[x(t) - x(t')]^2 + [y(t) - y(t')]^2}$ and t is a variable that parameterises the surface of the scatterer.

In order to build up a solution for the current density J_z the contour of the scatterer is discretised into cells as is shown in figure (3.9(b)). Each cell has centre (x_n, y_n) and is associated with a *pulse basis function* $p_n(t)$ represented by:

$$p_n(t) = \begin{cases} 1 & \text{if} \quad (x_n, y_n) \in \text{cell}\, n \\ 0 & \text{if} \quad (x_n, y_n) \notin \text{cell}\, n \end{cases} \tag{3.71}$$

The current density is a function of position around the surface of the scatterer and it can be approximated in terms of the pulse basis functions as:

$$J_z(t) \cong \sum_{n=1}^{N} j_n p_n(t) \tag{3.72}$$

Replacing (3.72) in (3.69) yields:

$$E_z^i \cong jk\eta \sum_{n=1}^{N} j_n \int_{\text{cell}\, n} \frac{1}{4j}H_0^{(2)}(kR)dt^{'} \tag{3.73}$$

N independent equations are obtained if Equation (3.73) is enforced at the centre of

each basis function domain. This is equivalent to using Dirac delta testing functions and is referred to as point matching. This produces a $N \times N$ system which can be written as follows:

$$\begin{bmatrix} E_z^i(t_1) \\ E_z^i(t_2) \\ \vdots \\ E_z^i(t_N) \end{bmatrix} = \begin{bmatrix} Z_{11} & Z_{12} & \dots & Z_{1N} \\ Z_{21} & Z_{22} & \dots & Z_{2N} \\ \vdots & \vdots & \dots & \vdots \\ Z_{N1} & Z_{N2} & \dots & Z_{NN} \end{bmatrix} \begin{bmatrix} j_1 \\ j_2 \\ \vdots \\ j_N \end{bmatrix} \tag{3.74}$$

Equation 3.74 can be solved in order to compute the unknown $j_1 \dots j_N$ coefficients. Once these coefficients are known, the fields exterior to the scatterer can be computed. The matrix $\mathbf{Z}$ is of order N and is referred to as the impedance matrix containing the interactions between the basis functions where the entries Z_{mn}, where $m \neq n$ are given by:

$$Z_{mn} = \frac{k\eta}{4} \int_{\text{cell}\, n} H_0^{(2)}(kR_m) dt' \tag{3.75}$$

where $R_m = \sqrt{[x_m(t) - x(t')]^2 + [y_m(t) - y(t')]^2}$. An approximation that the Hankel function is constant over each discretisation is considered, whereby the Z_{mn} entries can be expressed as:

$$Z_{mn} \cong \frac{k\eta}{4} w_n H_0^{(2)}(kR_{mn}) \tag{3.76}$$

where $R_{mn} = \sqrt{[x_m - x_n]^2 + [y_m - y_n]^2}$, w_n represents the width of cell n. It is not possible to use the same equation for the diagonal terms Z_{mm}, due to the fact that $R_{mm} = 0$ which makes the Hankel function infinite. Another approximation is considered in this case, whereby the Hankel function is replaced by a power series expansion. This leads to:

$$Z_{mm} \cong \frac{k\eta w_m}{4} \left\{ 1 - j\frac{2}{\pi} \left[\ln\left(\frac{\gamma k w_m}{4} \right) - 1 \right] \right\} \tag{3.77}$$

where $\gamma \cong 1.78107$.

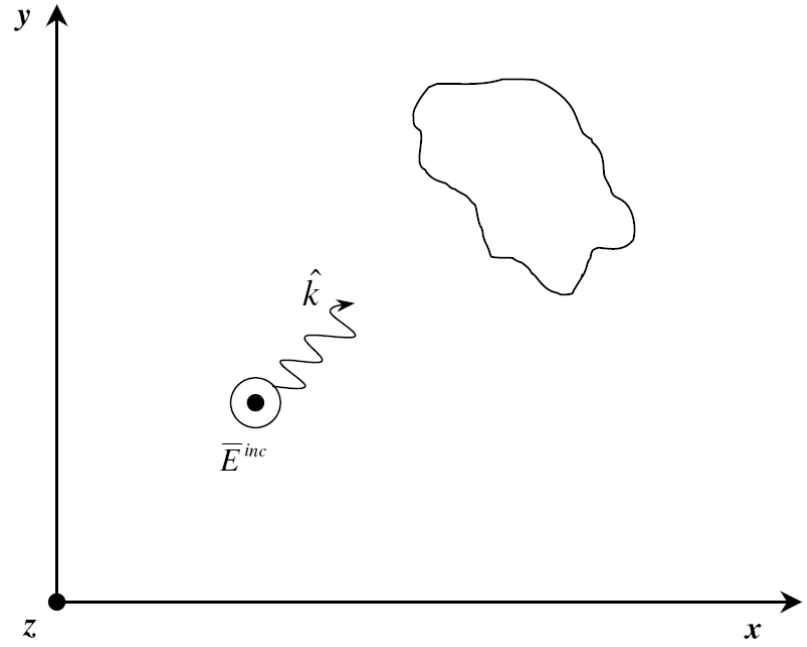

(a) A perfect electric conductor illuminated by a incident wave

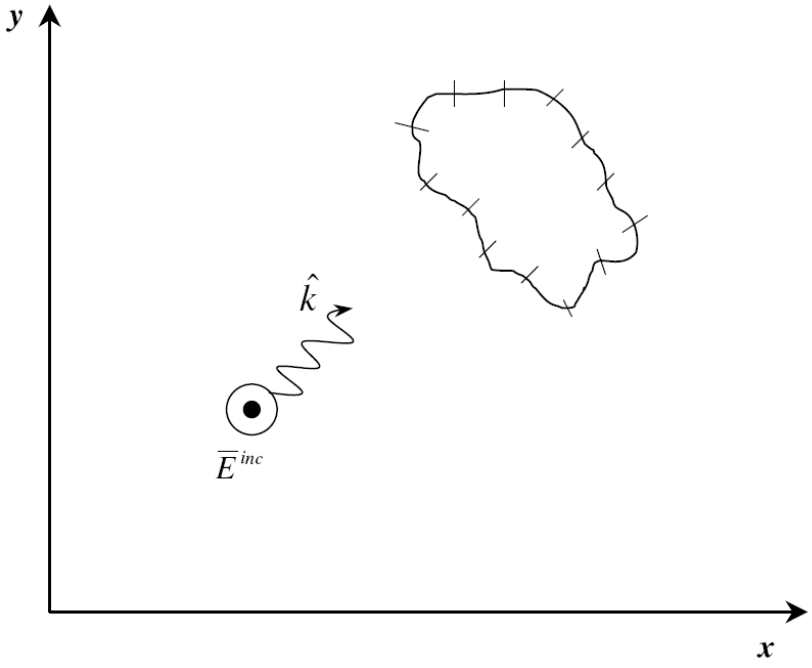

(b) The contour of the scatterer divided into cells

Figure 3.9: 2D PEC scatterer illuminated by a TM_z wave

3.2.2 Scattering from 3D Perfect Electric Conductors

Section (3.2.1) described the application of the MoM to the problem of scattering from 2D perfect electric objects. The discretisation of 3D scatterers is slightly more complex compared to the 2D scatterers. The scalar pulse basis functions are no longer employed in this case. In this work for the 3D case the basis functions are represented by vector fields defined on triangular patches. These basis functions are referred to as constant normal linear tangential CN/LT and are also known as triangular-cell rooftop or Rao - Wilton - Glisson (RWG) basis functions [8]. One advantage of these basis functions is the possibility of accurately discretising complex geometrical surfaces. Figure (3.10) depicts a PEC plate discretised using triangular patches.

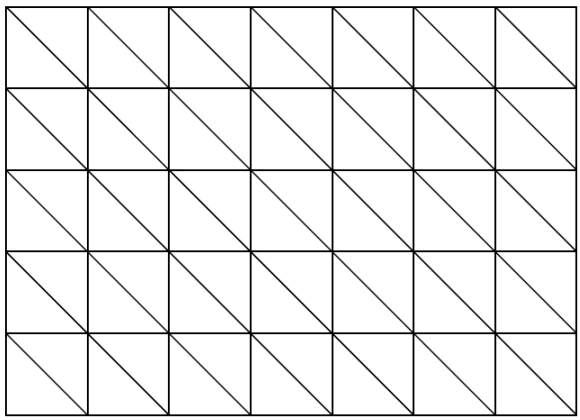

Figure 3.10: PEC plate discretised using triangular patches

The development of the RWG basis functions is thoroughly described by Rao, Wilton and Glisson in [8]. The surface of the scatterer is discretised into triangles and a basis function is defined for each interior edge. Each basis function thus has two triangles associated with it, T_m^+ and T_m^-, where the plus and the minus sign is determined by choosing a positive reference current direction [8].

The vector basis function can be defined as [3; 8]:

$$\mathbf{b}_m(\mathbf{r}) = \begin{cases} \frac{l_m}{2A_m^+}\boldsymbol{\rho}_m^+ & \text{for } \mathbf{r} \text{ in } T_m^+ \\ \frac{l_m}{2A_m^-}\boldsymbol{\rho}_m^- & \text{for } \mathbf{r} \text{ in } T_m^- \\ 0 & \text{otherwise} \end{cases} \tag{3.78}$$

where $\mathbf{r}$ is a position vector, l_m is the length of the interior edge associated with the basis function $\mathbf{b}_m$, A_m^+ and A_m^- are the areas of the attached triangles, $\boldsymbol{\rho}_m^+$ is a vector from the vertex to $\mathbf{r}$ (for $\mathbf{r}$ in T_m^+), and $\boldsymbol{\rho}_m^-$ is a vector from $\mathbf{r}$ to the vertex (for $\mathbf{r}$ in T_m^-).

The surface divergence of the basis function $\mathbf{b}_m$ is proportional to the surface charge density associated with it and can be written as [3; 8]:

$$\nabla \cdot \mathbf{b}_m = \begin{cases} \frac{l_m}{2A_m^+} & \text{for } \mathbf{r} \text{ in } T_m^+ \\ \frac{l_m}{2A_m^-} & \text{for } \mathbf{r} \text{ in } T_m^- \\ 0 & \text{otherwise} \end{cases} \tag{3.79}$$

As well as discretising the surface of the scatterer into basis functions, appropriate testing functions have to be defined. One of the testing functions that can be used for the triangular rooftop basis functions is the so-called razor blade testing function. For the basis function $\mathbf{b}_m$ in Figure (3.11) this testing function is defined along the straight path $\Delta\bar{t}_{m1}$, directed from the centroid of the T_m^+ triangle to the midpoint of the interior edge followed by the second straight path $\Delta\bar{t}_{m2}$, directed from the midpoint of the interior edge to the centroid of the T_m^- triangle [3; 8]. A testing function is associated with each such straight path and takes the value of the tangential vector along it [3; 8; 9].

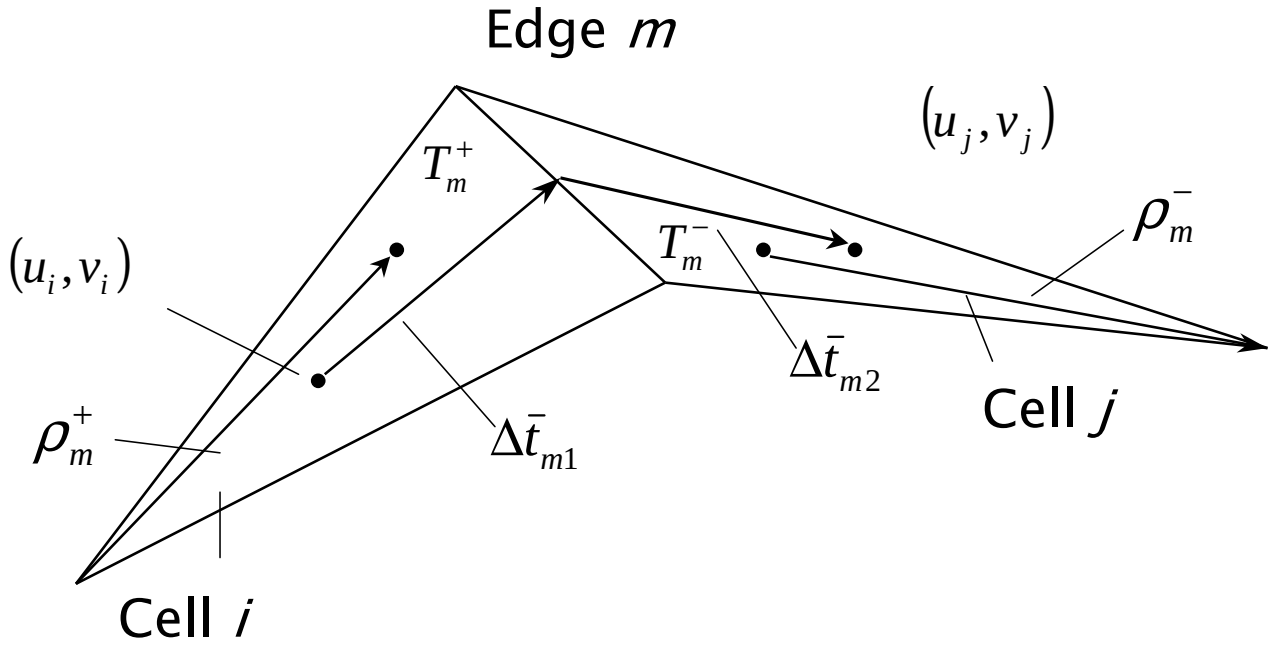

Figure 3.11: Triangular-cell rooftop basis function.

Applying the MoM with these basis and testing functions yields the matrix equation $\mathbf{ZJ} = \mathbf{V}$ where the entries of $\mathbf{Z}$ have the following formulation [3]:

$$Z_{mn} \cong jk\eta\Delta\bar{t}_{m1} \cdot \int\int \overline{\mathbf{b}}_m(u',v') \frac{e^{-jkR_m}}{4\pi R_m} du'dv'|_{u_i,v_i} \tag{3.80}$$

$$+ jk\eta\Delta\bar{t}_{m2} \cdot \int\int \overline{\mathbf{b}}_m(u',v') \frac{e^{-jkR_m}}{4\pi R_m} du'dv'|_{u_j,v_j} \tag{3.81}$$

$$+ \frac{\eta}{jk} \int\int \left[\nabla \cdot \overline{\mathbf{b}}_m\right] \frac{e^{-jkR_m}}{4\pi R_m} du'dv'|_{u_j,v_j} \tag{3.82}$$

$$- \frac{\eta}{jk} \int\int \left[\nabla \cdot \overline{\mathbf{b}}_m\right] \frac{e^{-jkR_m}}{4\pi R_m} du'dv'|_{u_i,v_i} \tag{3.83}$$

where $\bar{b}_m$ is the basis function associated with the edge m, (u_i, v_i) and (u_j, v_j) are the centroids of cell i and cell j respectively. It has to be noted that in cases when the source and observation regions are the same, $\frac{1}{R_m}$ singularities have to be integrated analytically [3]. The entries of the $\mathbf{V}$ vector are:

$$V_m = \int_{C_m} \overline{E}^{inc} \cdot d\bar{t} \tag{3.84}$$

3.2.3 Scattering from 2D homogeneous Dielectric Objects

Consider Figure (3.9) where a scatterer is illuminated by a TM_z wave. In this case the scatterer is a homogeneous dielectric object and is characterized by permittivity ε_d and permeability μ_d. In section (3.1) the surface equivalence principle for homogeneous dielectric scatterers was presented and the coupled EFIE equations (3.59-3.62) were derived in terms of the currents in the close proximity to the exterior and the interior of the scattering surface.

For a TM_z polarization the coupled EFIE was formulated in Section 3.1.5 and is given by:

$$E_z^{inc}(t) = K_t(t) + jk_0\mu_0 A_z^{(0)} + \{\frac{\partial F_y^{(0)}}{\partial x} - \frac{\partial F_x^{(0)}}{\partial y}\}_{S^+} \tag{3.85}$$

$$0 = -K_t(t) + jk_d\eta_d A_z^{(d)} + \{\frac{\partial F_y^{(d)}}{\partial x} - \frac{\partial F_x^{(d)}}{\partial y}\}_{S^-} \tag{3.86}$$

where

$$A_z^{(i)} = \int J_z(t^{'}) \frac{1}{4j} H_0^{(2)}(k_i R) dt^{'} \tag{3.87}$$

$$\bar{F}_t^{(i)} = \int \hat{t}(t^{'}) K_t(t^{'}) \frac{1}{4j} H_0^{(2)}(k_i R) dt^{'} \tag{3.88}$$

$$R = \sqrt{[x(t) - x(t^{'})]^2 + [y(t) - y(t^{'})]^2} \tag{3.89}$$

t is a variable that parameterises the surface of the scatterer, $\hat{t}$ represents the unit vector tangent to the scatterer contour. The parameters for the exterior of the body and the interior are denoted with the subscripts 0 and d: k_0 and k_d are the wavenumbers for the exterior and the interior of the body, η_0 and η_d are the intrinsic impedances for the exterior of the body and interior respectively.

Using the MoM with pulse basis functions and Dirac-delta testing functions, as can be seen in Figure (3.12), yields a matrix equation with a block structure given by:

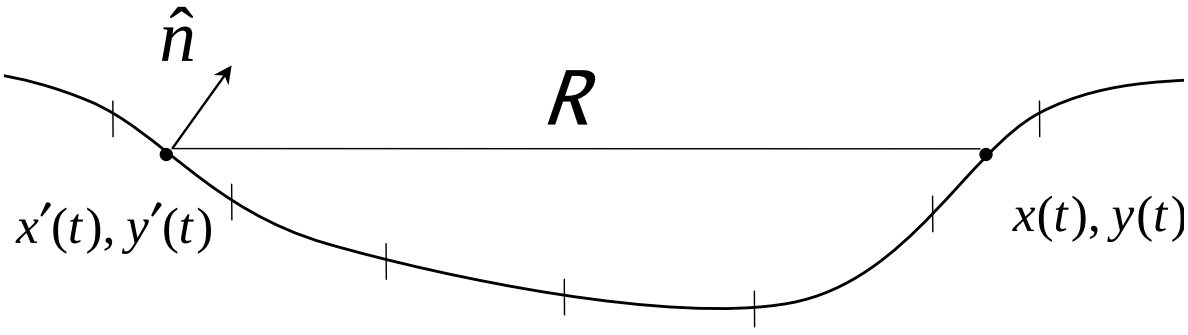

Figure 3.12: Discretised 2D scattering surface

$$\begin{bmatrix} \mathbf{E} \\ \mathbf{0} \end{bmatrix} = \begin{bmatrix} \mathbf{A} & \mathbf{B} \\ \mathbf{C} & \mathbf{D} \end{bmatrix} \begin{bmatrix} \mathbf{j} \\ \mathbf{k} \end{bmatrix} \tag{3.90}$$

each of the **A**, **B**, **C** and **D** matrices are of order N where:

$$A_{mn} = \frac{k_0\eta_0}{4}\int_{\text{cell }n} H_0^{(2)}(k_0R_m)dt' \tag{3.91}$$

$$B_{mn} = \frac{k_0}{4j}\int_{\text{cell }n}\left(\cos\phi_n\frac{\Delta x}{R_m}+\sin\phi_n\frac{\Delta y}{R_m}\right)H_1^{(2)}(k_0R_m)dt' \tag{3.92}$$

$$C_{mn} = \frac{k_d\eta_d}{4}\int_{\text{cell }n} H_0^{(2)}(k_dR_m)dt' \tag{3.93}$$

$$D_{mn} = \frac{k_d}{4j}\int_{\text{cell }n}\left(\cos\phi_n\frac{\Delta x}{R_m}+\sin\phi_n\frac{\Delta y}{R_m}\right)H_1^{(2)}(k_dR_m)dt' \tag{3.94}$$

where ϕ_n is the polar angle associated with the normal vector $\hat{n}$, and Δy and Δx are given by:

$$\Delta x = x_m - x(t') \tag{3.95}$$

$$\Delta y = y_m - y(t') \tag{3.96}$$

The self terms A_{mm} and C_{mm} can be calculated using the same approximation of the Hankel function as in Section 3.2.1 which gives us:

$$A_{mm} = \frac{k_0\eta_0 w_m}{4}\left\{1-j\frac{2}{\pi}\left[\ln\left(\frac{\gamma k_0 w_m}{4}\right)-1\right]\right\} \tag{3.97}$$

$$C_{mm} = \frac{k_d\eta_d w_m}{4}\left\{1-j\frac{2}{\pi}\left[\ln\left(\frac{\gamma k_d w_m}{4}\right)-1\right]\right\} \tag{3.98}$$

Correct treatment of the singularity for the B_{mm} and D_{mm} leads to:

$$B_{mm} = \frac{1}{2} \tag{3.99}$$

$$D_{mm} = -\frac{1}{2} \tag{3.100}$$

3.2.4 Scattering from 3D homogeneous Dielectric Object

When considering the problem of scattering from 3D homogeneous dielectric objects N *triangular-rooftop basis functions* and razor blade testing functions described in section 3.2.2 are used to implement the MoM [9].

In order to assess the performance of the BBFB method on a different formulation, the Combined Field Integral Equation formulation given by Equations (3.63-3.64) is employed when solving problems of wave scattering from 3D objects. The resulting equation after the discretization procedure is the following:

$$\begin{bmatrix} \mathbf{A} & \mathbf{B} \\ \mathbf{C} & \mathbf{D} \end{bmatrix} \begin{bmatrix} \mathbf{j} \\ \mathbf{k} \end{bmatrix} = \begin{bmatrix} \mathbf{e} \\ \mathbf{h} \end{bmatrix} \tag{3.101}$$

where the $\mathbf{A}$,$\mathbf{B}$,$\mathbf{C}$,$\mathbf{D}$ matrices are of size N and individual elements are given by:

$$\begin{aligned}
A_{mn} &= jk\eta \int_{C_m} \left\{ \iint \bar{\mathbf{b}}_n(u',v') \frac{e^{-jkR}}{4\pi R} du'dv' \right\} \cdot d\bar{t} && (3.102)\\
&+ \frac{\eta}{jk} \int_{C_m} \nabla \left\{ \iint [\nabla_s \cdot \bar{\mathbf{b}}_n] \frac{e^{-jkR}}{4\pi R} du'dv' \right\} \cdot d\bar{t} && (3.103)\\
&+ jk_d\eta_d \int_{C_m} \left\{ \iint \bar{\mathbf{b}}_n(u',v') \frac{e^{-jk_dR}}{4\pi R} du'dv' \right\} \cdot d\bar{t} && (3.104)\\
&+ \frac{\eta}{jk_d} \int_{C_m} \nabla \left\{ \iint [\nabla_s \cdot \bar{\mathbf{b}}_n] \frac{e^{-jk_dR}}{4\pi R} du'dv' \right\} \cdot d\bar{t} && (3.105)\\
B_{mn} &= -\int_{C_m} \left\{ \nabla \times \iint \bar{\mathbf{b}}_n(u',v') \frac{e^{-jkR}}{4\pi R} du'dv' \right\}_{S^+} \cdot d\bar{t} && (3.106)\\
&- \int_{C_m} \left\{ \nabla \times \iint \bar{\mathbf{b}}_n(u',v') \frac{e^{-jk_dR}}{4\pi R} du'dv' \right\}_{S^-} \cdot d\bar{t} && (3.107)
\end{aligned}$$

$$C_{mn} = \int_{C_m} \left\{ \nabla \times \iint \bar{\mathbf{b}}_n(u',v') \frac{e^{-jkR}}{4\pi R} du'dv' \right\}_{S^+} \cdot d\bar{t} \tag{3.108}$$

$$+ \int_{C_m} \left\{ \nabla \times \iint \bar{\mathbf{b}}_n(u',v') \frac{e^{-jk_dR}}{4\pi R} du'dv' \right\}_{S^-} \cdot d\bar{t} \tag{3.109}$$

$$D_{mn} = \frac{jk}{\eta} \int_{C_m} \left\{ \iint \bar{\mathbf{b}}_n(u',v') \frac{e^{-jkR}}{4\pi R} du'dv' \right\} \cdot d\bar{t} \tag{3.110}$$

$$+ \frac{1}{jk\eta} \int_{C_m} \nabla \left\{ \iint [\nabla_s \cdot \bar{\mathbf{b}}_n] \frac{e^{-jkR}}{4\pi R} du'dv' \right\} \cdot d\bar{t} \tag{3.111}$$

$$+ \frac{jk_d}{\eta_d} \int_{C_m} \left\{ \iint \bar{\mathbf{b}}_n(u',v') \frac{e^{-jk_dR}}{4\pi R} du'dv' \right\} \cdot d\bar{t} \tag{3.112}$$

$$+ \frac{1}{jk_d\eta_d} \int_{C_m} \nabla \left\{ \iint [\nabla_s \cdot \bar{\mathbf{b}}_n] \frac{e^{-jk_dR}}{4\pi R} du'dv' \right\} \cdot d\bar{t} \tag{3.113}$$

where $\bar{\mathbf{b}}_n$ is the basis function associated with the edge n and C_m is the path from the centroid of triangle T_m^+ to the centroid of T_m^- as seen in Figure (3.11). $\mathbf{e}$ and $\mathbf{h}$ are subvectors each of length N that describe the tested incident magnetic and electric fields, whereas $\mathbf{j}$ and $\mathbf{k}$ are the unknown subvectors each of length N.

3.3 Conclusion

The IE formulation and the MoM discretisation process for the 2D and 3D PECs and homogeneous dielectric scatterer cases have been presented in this Chapter. The matrix equation obtained in Section 3.2.2 is employed in Chapter 5 in order to compute the fields scattered from a wedge comprised of two P.E.C. plates. Chapter 6 focuses on the matrix equation derived in Section 3.2.3 for computing fields scattered from open and closed homogeneous dielectric surfaces. An extension of this is presented in Chapter 7 where the design of 2D TeraHertz band-gap waveguides is investigated. The problem of wave scattering from 3D homogeneous dielectric structures is solved in Chapter 8 by employing the matrix equation obtained in Section 3.2.4.

The scattering problems often involve objects that are quite large in terms of wavelengths. Hence the matrix equations obtained after applying the Method of Moments have a considerable number of elements. Due to the size of the matrix direct inversion can not be applied for solving the matrix equations and instead iterative techniques will be employed. A description of various available iterative methods is given in Chapter 4.

Chapter 4

Iterative Solvers

4.1 Introduction

The application of the Method of Moments to various integral equation formulations was described in the previous chapter. The resulting $\mathbf{ZJ} = \mathbf{V}$ matrix systems are usually of significant order, a consequence of the large number of discretisations needed to model the currents. Direct inversion is the most straightforward method to be used for solving a matrix equation. However, direct inversion is unfeasible when the $\mathbf{Z}$ matrix is of significant order. Instead iterative solvers are introduced in order to solve this problem [20; 15; 11; 13; 14; 10; 22; 63]. When using iterative solvers the $\mathbf{Z}$ matrix does not need to be explicitly stored, and they also reduce the computation times from $O(N^3)$ of the direct methods to $O(N^2)$, where N is the number of unknowns. When applying iterative techniques to electromagnetic wave scattering problems, a solution for the unknown vector $\mathbf{J}$ is refined over many iterations. The efficiency of the iterative solvers depends on various factors such as the geometry of the scatterer and the type of material, which in turn affects the composition of the $\mathbf{Z}$ matrix.

There are two main types of iterative methods: stationary and non stationary. These two classes are described in the current chapter. The stationary methods include Gauss-Seidel, Jacobi, Successive Overrelaxation and Symmetric Successive Overrelaxation. The most common non stationary algorithms are Conjugate Gradient (CG) and Generalised

Minimum Residual (GMRES). A history and overview of iterative solvers can be found in [15] and [10]. A comparison between various iterative solvers when applied to 2D scattering problems involving rough sea surfaces is described by West and Sturm in [20]. The conclusion of this work is that the non stationary techniques are less affected by the geometry of the scatterer which makes them more reliable for scattering problems involving objects that exhibit the possibility of multiple scattering. Nevertheless, when the stationary solvers work, they are more efficient in comparison to the non stationary ones.

4.2 Stationary Iterative Solvers

Consider the matrix equation:

$$\mathbf{Zx} = \mathbf{v} \tag{4.1}$$

where $\mathbf{Z}$ is a $N \times N$ matrix, $\mathbf{x}$ and $\mathbf{v}$ are both $N \times 1$ column vectors, where $\mathbf{x}$ is the unknown. The $\mathbf{Z}$ matrix can be decomposed using the matrix splitting [13]:

$$\mathbf{Z} = \mathbf{U} + \mathbf{L} + \mathbf{D} \tag{4.2}$$

where $\mathbf{U}$ is a $N \times N$ matrix containing the upper triangular portion of $\mathbf{Z}$ and the rest of the elements zero as can be seen in equation (4.3):

$$\mathbf{U} = \begin{bmatrix} 0 & z_{12} & \cdots & \cdots & z_{1N} \\ 0 & 0 & z_{23} & \cdots & \vdots \\ 0 & 0 & 0 & \cdots & z_{N-2,N} \\ \vdots & \vdots & \vdots & \ddots & z_{N-1,N} \\ 0 & 0 & \cdots & 0 & 0 \end{bmatrix} \tag{4.3}$$

$$\mathbf{L} = \begin{bmatrix} 0 & 0 & \cdots & \cdots & 0 \\ z_{21} & 0 & \cdots & \cdots & \vdots \\ z_{31} & z_{32} & \ddots & \cdots & 0 \\ \vdots & \vdots & \vdots & 0 & 0 \\ z_{N1} & z_{N2} & \cdots & z_{N,N-1} & 0 \end{bmatrix} \tag{4.4}$$

$\mathbf{L}$ is a $N \times N$ matrix containing the lower triangular portion of the $\mathbf{Z}$ matrix with the rest of the elements set to zero, as shown in equation (4.4). Subsequently $\mathbf{D}$ is a $N \times N$ matrix that contains only the diagonal of the $\mathbf{Z}$ matrix with the rest of the elements set to zero as in (4.5)

$$\mathbf{D} = \text{diag}(z_{11}, \cdots, z_{NN}) \tag{4.5}$$

An initial guess $\mathbf{x}^{(0)}$ is considered. Stationary iterative techniques update the estimate for $\mathbf{x}$ according to the rule [11]:

$$\mathbf{x}^{(k+1)} = \mathbf{M}\mathbf{x}^{(k)} + \boldsymbol{\beta} \tag{4.6}$$

where $\mathbf{x}^{(k+1)}$ is the $(k+1)st$ estimate of $\mathbf{x}$. The matrix $\mathbf{M}$ is called the iteration matrix. Both the iteration matrix $\mathbf{M}$ and the vector $\boldsymbol{\beta}$ are known and neither of them depends on the iteration step k. This is why these techniques are called stationary. The equation (4.6) describes all possible **stationary algorithms**. Each particular stationary technique is defined by its own iteration matrix $\mathbf{M}$.

The convergence of all stationary methods depends on the eigenvalues of the iteration matrix $\mathbf{M}$ [19], especially on its spectral radius ρ where

$$\rho(\mathbf{M}) = \max_{i=1}^{n}(|\lambda_i|) \tag{4.7}$$

where $\lambda_i \ldots \lambda_N$ are the eigenvalues of $\mathbf{M}$. The stationary methods have to satisfy the following condition in order to converge:

$$\rho(\mathbf{M}) < 1 \tag{4.8}$$

This can be proven by assuming that $\boldsymbol{\epsilon}^{(k+1)}$ is the error vector associated with the approximation $\mathbf{x}^{(k+1)}$, so that:

$$\boldsymbol{\epsilon}^{(k+1)} = \mathbf{x}^{(k+1)} - \mathbf{x} \tag{4.9}$$

By replacing Equation (4.6) into Equation (4.9) it is obvious that:

$$\boldsymbol{\epsilon}^{(k+1)} = \mathbf{M}\boldsymbol{\epsilon}^{(k)} \tag{4.10}$$

The eigenvectors of the iteration matrix $\mathbf{M}$ $\mathbf{e}_i$ satisfy:

$$\mathbf{M}\mathbf{e}_i = \lambda_i \mathbf{e}_i \tag{4.11}$$

If we express the initial error $\boldsymbol{\epsilon}^{(0)}$ as a linear combination of the iteration matrix eigenvector:

$$\boldsymbol{\epsilon}^{(0)} = \sum_{i=1}^{N} \alpha_i \mathbf{e}_i \tag{4.12}$$

then the error $\boldsymbol{\epsilon}^{(1)}$ can be expressed as:

$$\boldsymbol{\epsilon}^{(1)} = \sum_{i=1}^{N} \alpha_i \mathbf{M}\mathbf{e}_i \tag{4.13}$$

$$= \sum_{i=1}^{N} \alpha_i \lambda_i \mathbf{e}_i \tag{4.14}$$

Therefore, the error updated after each iteration can be written:

$$\boldsymbol{\epsilon}^{(k)} = \sum_{i=1}^{N} \alpha_i^k \lambda_i^k \mathbf{e}_i \tag{4.15}$$

so that $\left|\left|\boldsymbol{\epsilon}^{(k)}\right|\right| \to 0$ as $k \to \infty$, if $\lambda_i^k \to 0$ as $k \to \infty$.

Equation (4.15) shows that the overall error becomes smaller after each iteration only if the eigenvalues of the iteration matrix $\mathbf{M}$ are smaller than unity.

The stopping criteria for the stationary methods is formulated in terms of the residual vector $\mathbf{r}^{(k)}$ where:

$$\mathbf{r}^{(k)} = \left|\left|\mathbf{v} - \mathbf{Z}\mathbf{x}^{(k)}\right|\right| \tag{4.16}$$

A certain precision or tolerance is set and the stationary iteration will stop if:

$$\frac{||\mathbf{v} - \mathbf{Z}\mathbf{x}^{(k)}||}{||\mathbf{v}||} < \text{tolerance} \tag{4.17}$$

Equation (4.17) constrains the backward error of the solution and it should be similar to the accuracy of the computed elements of the impedance matrix $\mathbf{Z}$.

4.2.1 Jacobi Iterative Method

In order to derive the Jacobi method for the matrix equation $\mathbf{Z}\mathbf{x} = \mathbf{v}$ we re-arrange the matrix equation as follows [11]:

$$\mathbf{Z}\mathbf{x} = \mathbf{v} \tag{4.18}$$

$$(\mathbf{U} + \mathbf{L} + \mathbf{D})\mathbf{x} = \mathbf{v} \tag{4.19}$$

$$\mathbf{D}\mathbf{x} = -(\mathbf{U} + \mathbf{L})\mathbf{x} + \mathbf{v} \tag{4.20}$$

$$\mathbf{x} = -\mathbf{D}^{-1}(\mathbf{U} + \mathbf{L})\mathbf{x} + \mathbf{D}^{-1}\mathbf{v} \tag{4.21}$$

The iteration step $\mathbf{x}^{(k+1)}$ can then be defined as:

$$\mathbf{x}^{(k+1)} = -\mathbf{D}^{-1}(\mathbf{U} + \mathbf{L})\mathbf{x}^{(k)} + \mathbf{D}^{-1}\mathbf{v} \tag{4.22}$$

Therefore the iteration matrix is

$$\mathbf{M} = -\mathbf{D}^{-1}(\mathbf{U} + \mathbf{L}) \tag{4.23}$$

and vector $\boldsymbol{\beta}$ is given by:

$$\boldsymbol{\beta} = \mathbf{D}^{-1}\mathbf{v} \tag{4.24}$$

In order to illustrate the Jacobi iteration assume that $\mathbf{Z}\mathbf{x} = \mathbf{v}$ is a 3-by-3 system as shown

in (4.25)

$$\begin{bmatrix} z_{11} & z_{12} & z_{13} \\ z_{21} & z_{22} & z_{23} \\ z_{31} & z_{32} & z_{33} \end{bmatrix} \begin{bmatrix} x_1 \\ x_2 \\ x_3 \end{bmatrix} = \begin{bmatrix} v_1 \\ v_2 \\ v_3 \end{bmatrix} \tag{4.25}$$

This can be rewritten in the following form [13; 12]:

$$x_1 = (v_1 - z_{12}x_2 - z_{13}x_3)/z_{11} \tag{4.26}$$

$$x_2 = (v_2 - z_{21}x_1 - z_{23}x_3)/z_{22} \tag{4.27}$$

$$x_3 = (v_3 - z_{31}x_1 - z_{32}x_2)/z_{33} \tag{4.28}$$

Equations (4.29-4.31) describe how a new approximation $\mathbf{x}^{(k+1)}$ can be found in terms of $\mathbf{x}^{(k)}$ which was obtained after k iterations.

$$x_1^{(k+1)} = (v_1 - z_{12}x_2^{(k)} - z_{13}x_3^{(k)})/z_{11} \tag{4.29}$$

$$x_2^{(k+1)} = (v_2 - z_{21}x_1^{(k)} - z_{23}x_3^{(k)})/z_{22} \tag{4.30}$$

$$x_3^{(k+1)} = (v_3 - z_{31}x_1^{(k)} - z_{32}x_2^{(k)})/z_{33} \tag{4.31}$$

Therefore a general formulation for the Jacobi iteration can be represented by [13]:

$$x_i^{(k+1)} = \frac{v_i}{z_{ii}} - \frac{1}{z_{ii}} \sum_{j=1}^{i-1} z_{ij}x_j^{(k)} - \frac{1}{z_{ii}} \sum_{j=i+1}^{N} z_{ij}x_j^{(k)} \quad \text{for} \quad i = 1 \ldots N \tag{4.32}$$

In terms of the iteration matrix, the Jacobi iteration is captured by rewriting Equation (4.21) [11], [10], [14], which leads to Equation (4.33). Table (4.1) summarises the Jacobi technique.

$$\mathbf{x}^{(k+1)} = -\mathbf{D}^{-1}(\mathbf{U} + \mathbf{L})\mathbf{x}^{(k)} + \mathbf{D}^{-1}\mathbf{v} \tag{4.33}$$

Table 4.1: Jacobi Iteration

The Jacobi Iterative Algorithm to solve matrix equation $\mathbf{Zx} = \mathbf{v}$

$\mathbf{x}^{(0)} = 0$

for $k = 1, 2, \ldots$

  for $i = 1, 2, \ldots, N$

    $\sigma = 0$

    for $j = 1, 2, \ldots, N$

      if $i \neq j$

      $\sigma = \sigma + z_{ij} x_j^{(k-1)}$

      end if

    end

  $x_i^{(k)} = (v_i - \sigma)/z_{ii}$

  end

check if $\frac{||\mathbf{v} - \mathbf{Z}\mathbf{x}^{(k)}||}{||\mathbf{v}||} <$ tolerance

end

4.2.2 Gauss-Seidel Iterative Method

The matrix splitting for the Gauss-Seidel method is given by the following matrix re-arrangement of the matrix equation [11]:

$$\begin{aligned} \mathbf{Zx} &= \mathbf{v} && (4.34)\\ (\mathbf{U}+\mathbf{L}+\mathbf{D})\mathbf{x} &= \mathbf{v} && (4.35)\\ (\mathbf{L}+\mathbf{D})\mathbf{x} &= -\mathbf{Ux}+\mathbf{v} && (4.36)\\ \mathbf{x} &= -(\mathbf{L}+\mathbf{D})^{-1}\mathbf{Ux}+(\mathbf{L}+\mathbf{D})^{-1}\mathbf{v} && (4.37) \end{aligned}$$

As it can be seen from equation (4.37) the iteration matrix for the Gauss-Seidel method is:

$$\mathbf{M} = -(\mathbf{L}+\mathbf{D})^{-1}\mathbf{U} \tag{4.38}$$

Hence the approximation $\mathbf{x}^{(k+1)}$ is obtained from the $\mathbf{x}^{(k)}$ estimate by [11; 18]:

$$\mathbf{x}^{(k+1)} = -(\mathbf{L}+\mathbf{D})^{-1}\mathbf{U}\mathbf{x}^{(k)}+(\mathbf{L}+\mathbf{D})^{-1}\mathbf{v} \tag{4.39}$$

In terms of vector components the Gauss-Seidel method can be described by the following formula [11]:

$$x_i^{(k+1)} = \frac{v_i}{z_{ii}} - \frac{1}{z_{ii}}\sum_{j=1}^{i-1} z_{ij}x_j^{(k+1)} - \frac{1}{z_{ii}}\sum_{j=i+1}^{N} z_{ij}x_j^{(k)} \quad \text{for} \quad i=1,\ldots,N \tag{4.40}$$

where it can be noted that unlike the Jacobi method, the Gauss-Seidel method uses the most current estimate of x_i where available. The step by step algorithm for the Gauss-Seidel method is presented in Table (4.2) [17]. Generally the spectral radius for the *Gauss-Seidel* method is smaller that the spectral radius for the *Jacobi* method, therefore the *Gauss-Seidel* technique converges at a faster rate.

Table 4.2: Gauss-Seidel Iteration

The Gauss-Seidel iterative algorithm to solve matrix equation $\mathbf{Zx} = \mathbf{v}$

$\mathbf{x}^{(0)} = 0$

for $k = 1, 2, \ldots$

  for $i = 1, 2, \ldots, N$

    $\sigma = 0$

    for $j = 1, 2, \ldots, i-1$

      $\sigma = \sigma + z_{ij} x_j^{(k)}$

    end

    for $j = i+1, \ldots, N$

      $\sigma = \sigma + z_{ij} x_j^{(k-1)}$

    end

    $x_i^{(k)} = (v_i - \sigma)/z_{ii}$

  end

check if $\frac{||\mathbf{v} - \mathbf{Z}\mathbf{x}^{(k)}||}{||\mathbf{v}||} <$ tolerance

end

4.2.3 Successive Overrelaxation

In situations where the Gauss-Seidel spectral radius $\rho(\mathbf{M})$ is close to unity significant numbers of iterations are required. This drawback can be fixed by introducing a so called relaxation parameter $1 < \omega < 2$ which has the advantage of diminishing the eigenvalues of the iteration matrix $\mathbf{M}$. This algorithm is referred to as *Successive Overrelaxation* (*SOR*). According to this technique equation (4.40) becomes:

$$x_i^{(k+1)} = \omega \left(\frac{v_i}{z_{ii}} - \frac{1}{z_{ii}} \sum_{j=1}^{i-1} z_{ij} x_j^{(k+1)} - \frac{1}{z_{ii}} \sum_{j=i+1}^{N} z_{ij} x_j^{(k)}) \right) + (1-\omega) x_i^{(k)} \tag{4.41}$$

The general algorithm for the SOR method is described in Table (4.3) [17].
In terms of matrix decomposition the Successive Overrelaxation iteration becomes:

$$\mathbf{x}^{(k+1)} = (\mathbf{D} + \omega \mathbf{L})^{-1} \left([(1-\omega)\mathbf{D} - \omega \mathbf{U})] \, \mathbf{x}^{(k)} + \omega \mathbf{v} \right) \tag{4.42}$$

Hence the iteration matrix $\mathbf{M}$ for the SOR method is [11; 16]:

$$\mathbf{M} = (\mathbf{D} + \omega \mathbf{L})^{-1} \left((1-\omega)\mathbf{D} - \omega \mathbf{U} \right) \tag{4.43}$$

The advantage of the SOR method is that the spectral radius of the iteration matrix $\mathbf{M}$ is smaller than for the *Gauss-Seidel* method assuming good choice of ω, leading to faster convergence.

Table 4.3: SOR Iteration

The Successive Overelaxation Iterative Algorithm to solve matrix $\mathbf{Zx} = \mathbf{v}$

$\mathbf{x}^{(0)} = 0$

for $k = 1, 2, \ldots$

  for $i = 1, 2, \ldots, N$

    $\sigma = 0$

    for $j = 1, 2, \ldots, i-1$

      $\sigma = \sigma + z_{ij} x_j^{(k)}$

    end

    for $j = i+1, \ldots, N$

      $\sigma = \sigma + z_{ij} x_j^{(k-1)}$

    end

    $\sigma = (v_i - \sigma)/z_{ii}$

    $x_i^{(k)} = x_i^{(k-1)} + \omega(\sigma - x_i^{(k-1)})$

  end

check if $\frac{||\mathbf{v} - \mathbf{Z}\mathbf{x}^{(k)}||}{||\mathbf{v}||} <$ tolerance

end

A variation of the *Successive Overrelaxation* is *Symmetric Successive Overrelaxation* (*SSOR*). The *SSOR* approach combines two sweeps of the *SOR* technique. The forward sweep is equivalent to a regular *SOR* iteration, whereas the backward sweep represents the *SOR* iteration in reverse order [12]. The SSOR algorithm is described in Table (4.4) [17].

In terms of matrix decomposition the forward loop of the *SSOR* technique is [16]:

$$\mathbf{x}^{(k+\frac{1}{2})} = (\mathbf{D} + \omega\mathbf{L})^{-1} \left[(1-\omega)\mathbf{D} - \omega\mathbf{U}\right] \mathbf{x}^{(k)} + \omega\mathbf{v} \tag{4.44}$$

Consequently the formulation for the backward loop of the *SSOR* method is:

$$\mathbf{x}^{(k+1)} = (\mathbf{D} + \omega\mathbf{U})^{-1} \left[(1-\omega)\mathbf{D} - \omega\mathbf{L}\right] \mathbf{x}^{(k+\frac{1}{2})} + \omega\mathbf{v} \tag{4.45}$$

The iteration matrix $\mathbf{M}$ is obtained by combining the forward and backward steps of the *SSOR*. According to [15] the iteration matrix can be written as follows:

$$\mathbf{M} = (\mathbf{D} + \omega\mathbf{U})^{-1}[(1-\omega)\mathbf{D} - \omega\mathbf{L}](\mathbf{D} + \omega\mathbf{L})^{-1}[(1-\omega)\mathbf{D} - \omega\mathbf{U}] \tag{4.46}$$

The *Symmetric Successive Overrelaxation* algorithm with an optimal ω has in fact a slower convergence rate compared to the *Successive Overrelaxation* method with an optimal ω and it is mostly used as a preconditioning technique for other iterative solvers [17].

The SSOR technique lies at the basis of another method used in EM wave scattering computation, referred to as Forward-Backward. The Forward-Backward technique, also known as the Method of Ordered Multiple Interactions (MOMI) technique is equivalent to a SSOR with the relaxation parameter ω set to 1 [20; 64; 65; 66; 67; 68; 69]. The Buffered Block Forward Backward Method described in this thesis is in turn an extended formulation of the Forward-Backward technique.

Table 4.4: SSOR Iteration

The Symmetric Successive Overrelaxation Iterative Algorithm to solve matrix $\mathbf{Zx} = \mathbf{v}$

$\mathbf{x}^{(0)} = 0$

set $\mathbf{x}^{(\frac{1}{2})} = \mathbf{x}^{(0)}$

for $k = 1, 2, \ldots$

  for $i = 1, 2, \ldots, N$
    $\sigma = 0$

    for $j = 1, 2, \ldots, i-1$
      $\sigma = \sigma + z_{ij} x_j^{(k-\frac{1}{2})}$
    end

    for $j = i+1, \ldots, N$
      $\sigma = \sigma + z_{ij} x_j^{(k-1)}$
    end

    $\sigma = (v_i - \sigma)/z_{ii}$
    $x_i^{(k-\frac{1}{2})} = x_i^{(k-1)} + \omega(\sigma - x_i^{(k-1)})$
  end

  for $i = N, N-1, \ldots, 1$
    $\sigma = 0$

    for $j = 1, 2, \ldots, i-1$
      $\sigma = \sigma + z_{ij} x_j^{(k-\frac{1}{2})}$
    end

    for $j = i+1, \ldots, N$
      $\sigma = \sigma + z_{ij} x_j^{(k)}$
    end

    $x_i^{(k)} = x_i^{(k-\frac{1}{2})} + \omega(\sigma - x_i^{(k-\frac{1}{2})})$
  end

check if $\frac{||\mathbf{v} - \mathbf{Z}\mathbf{x}^{(k)}||}{||\mathbf{v}||} <$ tolerance

end

4.3 Non Stationary Iterative Solvers

Non stationary iterative methods represent another category of algorithms used to solve discretised electromagnetic scattering problems [15; 14; 10; 17]. These techniques are based on projection onto *Krylov* subspaces and they are currently considered to be the most robust available iterative solvers [3; 14; 13].

For the matrix equation $\mathbf{Zx} = \mathbf{v}$, expression (4.47) describes the *Krylov* subspace associated with the $\mathbf{Z}$ matrix [11; 14]:

$$\mathbf{K}_k = \text{span}\{\mathbf{v}, \mathbf{Zv}, \mathbf{Z}^2\mathbf{v}, \ldots, \mathbf{Z}^{k-1}\mathbf{v}\} \tag{4.47}$$

When solving the matrix equation $\mathbf{Zx} = \mathbf{v}$ using *non stationary* methods the kth iterate $\mathbf{x}^{(k)}$ lie within the subspace $\mathbf{K}_k$ and a satisfactory solution is usually found in $k \ll N$ iterations. In order to employ the *Krylov subspace* an initial solution $\mathbf{x}^{(0)}$ has to be chosen [11] within the subspace $\mathbf{K}_k$. The initial estimate is usually chosen to be $\mathbf{x}^{(0)} = 0$. The approximate solution $\mathbf{x}^{(k)}$ is chosen to be a value that minimizes the residual [11] :

$$||\mathbf{v} - \mathbf{Zx}|| \tag{4.48}$$

where $\mathbf{x}$ satisfies the condition $\mathbf{x} \in \mathbf{K}_k$. This leads to the following solution:

$$\mathbf{x}^{(k)} = \min_{x \in \mathbf{K}_k} ||\mathbf{v} - \mathbf{Zx}|| \tag{4.49}$$

Consider the estimated solution $\mathbf{x}^{(k)}$ to be of form $\mathbf{x}^{(0)} + \mathbf{y}^{(k)}$, where $\mathbf{x}^{(0)}$ is the initial approximation and $\mathbf{y}^{(k)}$ is an element of $\mathbf{K}_k$. Therefore $\mathbf{y}^{(k)}$ can be written as:

$$\mathbf{y}^{(k)} = \mathbf{x}^{(k)} - \mathbf{x}^{(0)} \tag{4.50}$$

and equation (4.49) can be rewritten:

$$\mathbf{y}^{(k)} = \min_{\mathbf{y}\in\mathbf{K}_k} \left|\left|\mathbf{v} - \mathbf{Z}(\mathbf{y} + \mathbf{x}^{(0)})\right|\right| \tag{4.51}$$

$$= \min_{\mathbf{y}\in\mathbf{K}_k} \left|\left|\mathbf{v} - \mathbf{Z}\mathbf{x}^{(0)} - \mathbf{Z}\mathbf{y}\right|\right| \tag{4.52}$$

$$= \min_{\mathbf{y}\in\mathbf{K}_k} \left|\left|\mathbf{r}^{(0)} - \mathbf{Z}\mathbf{y}\right|\right| \tag{4.53}$$

where $\mathbf{r}^{(0)}$ is referred to as the initial residual and has the form:

$$\mathbf{r}^{(0)} = \mathbf{v} - \mathbf{Z}\mathbf{x}^{(0)} \tag{4.54}$$

4.3.1 Generalised Minimum Residual

The Generalised Minimum Residual (GMRES) technique is based on the principle of identifying the smallest residual. The GMRES method is an effective one and is very popular in solving discretised electromagnetic wave scattering problems. This is due to the fact that it generally finds an acceptable solution in $k \ll N$ iterations, where k is the number of estimates and N is the order of the $\mathbf{Z}$ matrix.

The Arnoldi iteration is used in order to find the minimal residual vector. The Arnoldi algorithm reduces dense non-Hermitian matrices into Hessenberg form. This technique allows the approximation of the eigenvalues of the original matrix. The Hessenberg reduction has the form:

$$\mathbf{Q}^T\mathbf{Z}\mathbf{Q} = \mathbf{H} \tag{4.55}$$

where $\mathbf{Q}$ is the matrix of computed orthonormal vectors, given by $\mathbf{Q} = [\mathbf{q}_1, \ldots, \mathbf{q_k}]$, and $\mathbf{H}$ is given by:

$$\mathbf{H} = \begin{bmatrix} h_{1,1} & h_{1,2} & h_{1,3} & \dots & \dots & h_{1,k} & \dots & \dots & h_{1,m} \\ h_{2,1} & h_{2,2} & h_{2,3} & \dots & \dots & h_{2,k} & \dots & \dots & h_{2,m} \\ 0 & h_{3,2} & h_{3,3} & \dots & \dots & h_{3,k} & \dots & \dots & h_{3,m} \\ 0 & 0 & h_{4,3} & \ddots & \dots & \vdots & \dots & \dots & h_{4,m} \\ 0 & 0 & 0 & \ddots & h_{k-1,k-2} & \vdots & \dots & \dots & \vdots \\ \vdots & 0 & 0 & \ddots & h_{k,k-2} & h_{k,k} & \dots & \dots & \vdots \\ \vdots & \dots & \dots & \ddots & 0 & h_{k+1,k} & \dots & \vdots & \\ \vdots & \dots & \dots & \dots & \dots & 0 & \ddots & \ddots & \vdots \\ 0 & 0 & 0 & 0 & 0 & 0 & 0 & h_{m,m-1} & h_{m,m} \end{bmatrix} \tag{4.56}$$

The Arnoldi algorithm is used in order to construct a sequence of Krylov matrices $\mathbf{Q}_k$, where $[\mathbf{q}_1, \dots, \mathbf{q}_k]$ span the Krylov subspace $\mathbf{K}_k$. Now consider only part of the Hessenberg matrix, so that:

$$\mathbf{H}_k = \begin{bmatrix} h_{1,1} & h_{1,2} & h_{1,3} & \dots & \dots & h_{1,k} \\ h_{2,1} & h_{2,2} & h_{2,3} & \dots & \dots & h_{2,k} \\ 0 & h_{3,2} & h_{3,3} & \dots & \dots & h_{3,k} \\ 0 & 0 & h_{4,3} & \ddots & \dots & \vdots \\ 0 & 0 & 0 & \ddots & h_{k-1,k-2} & \vdots \\ \vdots & 0 & 0 & \ddots & h_{k,k-1} & h_{k,k} \\ 0 & \dots & \dots & \ddots & 0 & h_{k+1,k} \end{bmatrix} \tag{4.57}$$

Equation (4.55) yields:

$$\mathbf{Z}\mathbf{Q}_k = \mathbf{Q}_{k+1}\mathbf{H}_k \tag{4.58}$$

where $\mathbf{Q}_k = [\mathbf{q}_1, \dots, \mathbf{q_k}]$ and $\mathbf{Q}_{k+1} = [\mathbf{q}_1, \dots, \mathbf{q_k}, \mathbf{q}_{k+1}]$. Therefore we can write:

$$\mathbf{Z}\mathbf{q}_k = h_{1,k}\mathbf{q}_1 + h_{2,k}\mathbf{q}_2 + \dots + h_{k,k}\mathbf{q}_k + h_{k+1,k}\mathbf{q}_{k+1} \tag{4.59}$$

Hence the expression for the orthonormal $\mathbf{q}_k$ vector can be written:

$$\mathbf{q}_{k+1} = \frac{\mathbf{Z}\mathbf{q}_k - \sum_{i=1}^{k} h_{i,k}\mathbf{q}_i}{h_{k+1,k}} \tag{4.60}$$

Now the GMRES iterative method can be derived using the Arnoldi approach described in Table (4.5). Assume $\mathbf{x}^{(k)} = \mathbf{Q}_k\mathbf{y}$, so that the problem now is to find a vector $\mathbf{y}$ that minimises the following expression:

$$\min_{\mathbf{y}\in\mathbf{K}_k} ||\mathbf{v} - \mathbf{Z}\mathbf{Q}_k\mathbf{y}|| \tag{4.61}$$

instead of $\min_{\mathbf{y}\in\mathbf{K}_k} ||\mathbf{v} - \mathbf{Z}\mathbf{y}||$. Equation (4.61) will be much easier to handle, because $\mathbf{Q}_k$ is well-conditioned due to its orthonormal columns. Substituting (4.58) in (4.61) we obtain:

$$\mathbf{y}^{(k)} = \min_{\mathbf{y}\in\mathbf{K}_k} ||\mathbf{v} - \mathbf{Q}_{k+1}\mathbf{H}_k\mathbf{y}|| \tag{4.62}$$

Using the property that the 2-norm is not changed if multiplied by a unitary matrix we can write:

$$\mathbf{y}^{(k)} = \min_{\mathbf{y}\in\mathbf{K}_k} \left|\left|\mathbf{Q}_{k+1}^T\mathbf{v} - \mathbf{Q}_{k+1}^T\mathbf{Q}_{k+1}\mathbf{H}_k\mathbf{y}\right|\right| \tag{4.63}$$

which leads to:

$$\mathbf{y}^{(k)} = \min_{\mathbf{y}\in\mathbf{K}_k} \left|\left|\mathbf{Q}_{k+1}^T\mathbf{v} - \mathbf{H}_k\mathbf{y}\right|\right| \tag{4.64}$$

The vector $\mathbf{Q}_{k+1}^T\mathbf{v}$ is given by:

$$\mathbf{Q}_{k+1}^T\mathbf{v} = \begin{bmatrix} \mathbf{q}_1^T\mathbf{v} \\ \mathbf{q}_2^T\mathbf{v} \\ \vdots \\ \mathbf{q}_{k+1}^T\mathbf{v} \end{bmatrix} \tag{4.65}$$

It is known that the columns $\mathbf{q}_j$ of $\mathbf{Q}_k$ are orthonormal, therefore $\mathbf{q}_1 = \frac{\mathbf{v}}{||\mathbf{v}||}$, and $\mathbf{q}_j^T\mathbf{v} = 0$ for any $j > 1$. Thus we can write:

$$\mathbf{Q}_{k+1}^T\mathbf{v} = ||\mathbf{v}||\,\mathbf{e}_1 \tag{4.66}$$

where $\mathbf{e}_1$ is referred to as the first vector and is given by:

$$\mathbf{e}_1 = [1, 0, 0, \ldots, 0] \tag{4.67}$$

Equation (4.66) can now be replaced in (4.64):

$$\mathbf{y}^{(k)} = \min_{\mathbf{y} \in \mathbf{K}_k} ||||\mathbf{v}||\, \mathbf{e}_1 - \mathbf{H}_k \mathbf{y}|| \tag{4.68}$$

and $\mathbf{x}^{(k)} = \mathbf{Q}_k \mathbf{y}^{(k)}$. The GMRES algorithm is outlined in Table (4.6) [11].
The conventional termination criteria for the GMRES method is that the relative residual $\frac{||\mathbf{r}^{(k)}||}{||\mathbf{v}||}$ should be smaller than a previously assigned tolerance [11].

The GMRES method provides a generally acceptable solution for the $\mathbf{Zx} = \mathbf{v}$ matrix equation without requiring too many iterations. It requires extra computational resources when increasing the number of iterations due to the fact that in order to achieve an accurate result all the computed orthonormal vectors have to be stored[15].

Table 4.5: Arnoldi Iteration

The Arnoldi Algorithm to reduce $\mathbf{Z}$ to a Hessenberg form

set $\mathbf{q}_1 = \frac{\mathbf{v}}{||\mathbf{v}||}$

for $k = 1, 2, \ldots$

$\mathbf{w} = \mathbf{Z}\mathbf{q}_k$

for $j = 1, 2, \ldots, N$

$h_{j,k} = \mathbf{q}_j^T \mathbf{w}$

$\mathbf{w} = \mathbf{w} - h_{j,k}\mathbf{q}_j$

end

$h_{k+1,k} = ||\mathbf{w}||$

$\mathbf{q}_{k+1} = \frac{\mathbf{w}}{h_{k+1,k}}$

end

Table 4.6: GMRES Iteration

The Generalised Minimum Residual Iterative Algorithm

$\mathbf{q}_1 = \frac{\mathbf{v}}{||\mathbf{v}||}$

for $k = 1, 2, \ldots$

$\mathbf{w} = \mathbf{Z}\mathbf{q}_k$

for $j = 1, 2, \ldots, N$

$h_{j,k} = \mathbf{q}_j^T \mathbf{w}$

$\mathbf{w} = \mathbf{w} - h_{j,k}\mathbf{q}_j$

for $j = 1, 2, \ldots, i-1$

end

$h_{k+1,k} = ||\mathbf{w}||$

$\mathbf{q}_{k+1} = \frac{\mathbf{w}}{h_{k+1,k}}$

find $\mathbf{y}$ that minimises $||||\mathbf{v}||\,\mathbf{e}_1 - \mathbf{H}_k\mathbf{y}||$

set $\mathbf{x}^{(k)} = \mathbf{Q}_k\mathbf{y}^{(k)}$

check if $\frac{||\mathbf{v}-\mathbf{Z}\mathbf{x}^{(k)}||}{||\mathbf{v}||} <$ tolerance

end

4.3.2 Conjugate Gradient Method

The Conjugate Gradient (CG) method is another non-stationary iterative technique that is a part of a separate class of iterative solvers known as the Conjugate Direction Methods [11]. This method is used in order to solve the $\mathbf{Zx} = \mathbf{v}$ matrix equation where $\mathbf{Z}$ is Hermitian positive definite. Consider the quadratic function $F(\mathbf{x})$ [11]:

$$F(\mathbf{x}) = c - \mathbf{v}^T\mathbf{x} + \frac{1}{2}\mathbf{x}^T\mathbf{Z}\mathbf{x} \tag{4.69}$$

where $c \in \mathbb{R}$. The objective of the Conjugate Gradient method is to find a minimum of F. Assume that $c = 0$. Therefore it can be stated that [11]:

$$\nabla F(\mathbf{x}) = -\mathbf{v} + \mathbf{Z}\mathbf{x} \tag{4.70}$$

As the original equation is $\mathbf{Zx} = \mathbf{v}$, finding the F such that $\nabla F = 0$ will lead to the solution of the matrix equation.

The Conjugate Gradient method is based on finding a set of conjugate directions for $\mathbf{Z}$. The first direction is the *steepest descent* and has the following formulation [11]:

$$\mathbf{d}^{(0)} = -\nabla F(\mathbf{x}^{(0)}) \tag{4.71}$$

$$= \mathbf{v} - \mathbf{Z}\mathbf{x}^{(0)} \tag{4.72}$$

where $\mathbf{x}^{(0)}$ is the initial guess of the solution. A parameter α_0 is chosen in order to minimize F so that:

$$\mathbf{x}^{(1)} = \mathbf{x}^{(0)} + \alpha_0\mathbf{d}^{(0)} \tag{4.73}$$

Similarly at kth approximation α_k is chosen to optimise the distance travelled in the direction $\mathbf{d}^{(k)}$, leading to:

$$\mathbf{x}^{(k+1)} = \mathbf{x}^{(k)} + \alpha_k\mathbf{d}^{(k)} \tag{4.74}$$

The residual vector $\mathbf{r}^{(k)}$ given by $\mathbf{r}^{(k)} = \mathbf{v} - \mathbf{Z}\mathbf{x}^{(k)}$ indicates how far the current estimate is

from satisfying the matrix equation and it represents the direction of the steepest descent. The scalar parameter α_k can be computed by expressing $F(\mathbf{x}^{(k)})$ in terms of α_k:

$$F(\mathbf{x}^{(k+1)}) = \frac{1}{2}\left(\mathbf{x}^{(k)} + \alpha_k \mathbf{d}^{(k)}\right)^T \mathbf{Z}\left(\mathbf{x}^{(k)} + \alpha_k \mathbf{d}^{(k)}\right) - \mathbf{v}^T\left(\mathbf{x}^{(k)} + \alpha_k \mathbf{d}^{(k)}\right) \tag{4.75}$$

α_k minimises $F(\mathbf{x}^{(k+1)})$ when $\frac{\partial}{\partial \alpha_k} F(\mathbf{x}^{(k+1)}) = 0$, yielding:

$$\alpha_k = \frac{(\mathbf{r}^{(k)})^T \mathbf{r}^{(k)}}{(\mathbf{d}^{(k)})^T \mathbf{Z}\mathbf{d}^{(k)}} \tag{4.76}$$

In addition a scalar β is computed using the Gram-Schmidt process, which defines the direction $\mathbf{d}^{(k)}$. Consider a set of linearly independent vectors $\mathbf{u}^{(0)}, \ldots, \mathbf{u}^{(k)}$. Gram-Schmidt obtains Z-orthogonal vectors $\mathbf{d}^{(0)} \ldots, \mathbf{d}^{(k)}$ by subtracting any components $\mathbf{d}^{(k)}$ that are not Z-orthogonal to $\mathbf{d}^{(k-1)}$ from $\mathbf{u}^{(k)}$. Given a positive definite matrix $\mathbf{Z}$, two vectors $\mathbf{m}$ and $\mathbf{n}$ are said to be Z-orthogonal if

$$\mathbf{m}^T \mathbf{Z}\mathbf{n} = 0 \tag{4.77}$$

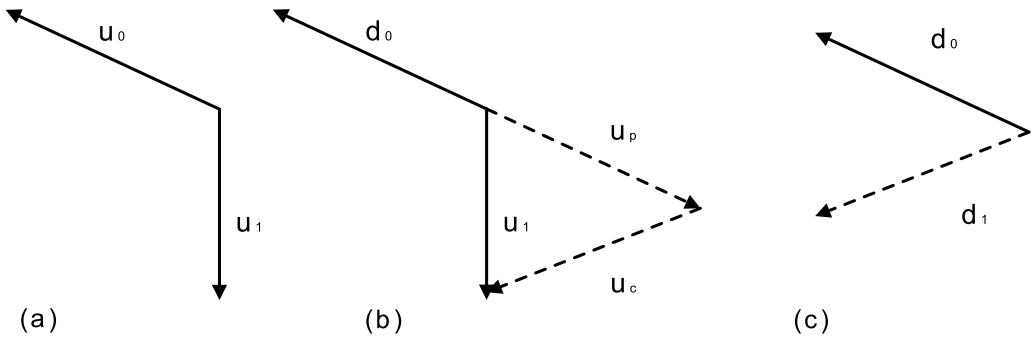

Figure 4.1: The Gram-Schmidt conjugate process

A schematic description of the Gram-Schmidt algorithm is presented in Figure (4.1). Two linearly independent vectors $\mathbf{u}^{(0)}$ and $\mathbf{u}^{(1)}$ are considered in Figure (4.1(a)). Set $\mathbf{d}^{(0)} = \mathbf{u}^{(0)}$. The two components of $\mathbf{u}^{(1)}$ are presented in Figure (4.1(b)), where $\mathbf{u}_c$ is Z-orthogonal to $\mathbf{d}^{(0)}$ and $\mathbf{u}_p$ is parallel to $\mathbf{d}^{(0)}$. After the Gram-Schmidt process only the Z-orthonormal component $\mathbf{u}_c$ remains, whereby $\mathbf{d}^{(1)} = \mathbf{u}_c$ as seen in (4.1(b)).

In general:

$$\mathbf{d}^{(k)} = \mathbf{u}^{(k)} + \sum_{i=0}^{k-1} \beta_{ik} \mathbf{d}^{(i)} \tag{4.78}$$

$$(\mathbf{d}^{(k)})^T = (\mathbf{u}^{(k)})^T + \sum_{i=0}^{k-1} \beta_{ik} (\mathbf{d}^{(i)})^T \tag{4.79}$$

where $\beta_i^{(k)}$ are defined for $k > i$. By multiplying both side with $\mathbf{Z}\mathbf{d}^{(j)}$ we obtain:

$$(\mathbf{d}^{(k)})^T \mathbf{Z}\mathbf{d}^{(j)} = (\mathbf{u}^{(k)})^T \mathbf{Z}\mathbf{d}^{(j)} + \sum_{i=0}^{k-1} \beta_{ik} (\mathbf{d}^{(i)})^T \mathbf{Z}\mathbf{d}^{(j)} \tag{4.80}$$

Since the vectors $\mathbf{d}$ are Z-orhtogonal, the property 4.77 can be applied, leading to:

$$0 = (\mathbf{u}^{(k)})^T \mathbf{Z}\mathbf{d}^{(j)} + \beta_{ik} (\mathbf{d}^{(k)})^T \mathbf{Z}\mathbf{d}^{(j)} \quad \text{for} \quad k > j \tag{4.81}$$

Therefore the scalar β can be expressed as

$$\beta_{ik} = -\frac{(\mathbf{u}^k)^T \mathbf{Z}\mathbf{d}^{(j)}}{(\mathbf{d}^{(j)})^T \mathbf{Z}\mathbf{d}^{(j)}} \tag{4.82}$$

Now set $\mathbf{r}^{(k)} = \mathbf{u}^{(\mathbf{k})}$. β_{ik} only exists for $i > k$ and is now referred to as β_k and it can be written in terms of the residual:

$$\beta_k = -\frac{(\mathbf{r}^k)^T \mathbf{Z}\mathbf{d}^{(j)}}{(\mathbf{d}^{(j)})^T \mathbf{Z}\mathbf{d}^{(j)}} \tag{4.83}$$

For each new iteration a new direction is computed [11]:

$$\mathbf{d}^{(k+1)} = \mathbf{r}^{(k+1)} + \beta_k \mathbf{d}^{(k)} \tag{4.84}$$

The residuals are given by:

$$\mathbf{r}^{(k)} = \mathbf{v} - \mathbf{Z}\mathbf{x}^{(k)} \tag{4.85}$$

$$= \mathbf{v} - \mathbf{Z}(\mathbf{x}^{(k-1)} + \alpha_{k-1}\mathbf{d}^{(k-1)}) \tag{4.86}$$

This leads to:

$$\mathbf{Z}\mathbf{d}^{(k-1)} = \frac{\mathbf{r}^{(k)} - \mathbf{r}^{(k-1)}}{\alpha_{k-1}} \tag{4.87}$$

By replacing Equation (4.87) in Equation (4.83) β can now be written as

$$\beta_k = -\frac{1}{\alpha_k} \frac{(\mathbf{r}^{(k)})^T(\mathbf{r}^{(k+1)} - \mathbf{r}^{(k)})}{(\mathbf{d}^{(k)})^T\mathbf{Z}\mathbf{d}^{(k)}} \tag{4.88}$$

And finally, replacing (4.76) in (4.88) β_k can be written in terms of residuals only:

$$\beta_k = \frac{(\mathbf{r}^{(k+1)})^T\mathbf{r}^{(k+1)}}{(\mathbf{r}^{(k)})^T\mathbf{r}^{(k)}} \tag{4.89}$$

Other methods have been developed from the CG algorithm, for example the Conjugate Gradient Normal Equations Residual Method (CGNR) which is applicable to non-symmetric systems. In order to apply the CGNR method a simple substitution is performed within the Conjugate Gradient $\mathbf{Z} \leftarrow \mathbf{Z}^H\mathbf{Z}$, where $\mathbf{Z}^H$ is the Hermitian transpose of $\mathbf{Z}$. This leads to the following equation to be solved:

$$\mathbf{Z}\mathbf{Z}^H\mathbf{x} = \mathbf{Z}^H\mathbf{v} \tag{4.90}$$

The Conjugate Gradient Normal Equations Error (CGNE) method is another variation of the CG technique where the matrix equation has the form:

$$\mathbf{Z}\mathbf{Z}^H\mathbf{y} = \mathbf{v} \tag{4.91}$$

so that $\mathbf{x} = \mathbf{Z}^H\mathbf{y}$. The Conjugate Gradient algorithm is presented in Table (4.7) [14].

Table 4.7: CG Iteration

The Conjugate Gradient Iterative Algorithm to solve the matrix equation **Zxv**

$\mathbf{x}^{(0)} = 0; \quad \mathbf{r}^{(0)} = \mathbf{v} - \mathbf{Z}\mathbf{x}^{(0)}; \quad \mathbf{d}^{(0)} = \mathbf{r}^{(0)}$

for $\quad k = 0, 1, \ldots$

$\alpha_k = \frac{(\mathbf{r}^{(k)})^T \mathbf{r}^k}{(\mathbf{d}^{(k)})^T \mathbf{Z}\mathbf{d}^{(k)}}$

$\mathbf{x}^{(k+1)} = \mathbf{x}^{(k)} + \alpha_k \mathbf{d}^{(k)}$

$\mathbf{r}^{(k+1)} = \mathbf{r}^{(k)} - \alpha_k \mathbf{Z}\mathbf{d}^{(k)}$

$\beta_k = \frac{(\mathbf{r}^{(k+1)})^T \mathbf{r}^{(k+1)}}{(\mathbf{r}^{(k)})^T \mathbf{r}^{(k)}}$

$\mathbf{d}^{(k+1)} = \mathbf{r}^{(k+1)} + \beta_k \mathbf{d}^{(k)}$

check if $\quad \frac{||\mathbf{r}^{(k+1)}||}{||\mathbf{v}||} < \text{tolerance}$

end

4.3.3 BiConjugate Gradient

The Conjugate Gradient method is only suitable for symmetrical systems. The CGNR method can be applied to non-symmetrical systems. However another variation of the CG, referred to as Biconjugate Gradient method (BiCG), can be employed instead. The BiCG is applicable to non-symmetrical systems but does not guarantee minimisation anymore. Instead it replaces the orthogonal sequence of residuals by two mutually orthogonal sequences. Hence the BiCG involves the computation of two different residuals and two different directions at each iteration. The BiCG requires a much smaller storage demand compared to the GMRES method which makes it more cost effective [17]. Two separate residuals are updated so that [17; 16]:

$$\mathbf{r}^{(k+1)} = \mathbf{r}^{(k)} - \alpha_k \mathbf{Z}\mathbf{d}^{(k)} \tag{4.92}$$

$$\bar{\mathbf{r}}^{(k+1)} = \bar{\mathbf{r}}^{(k)} - \alpha_k \mathbf{Z}^T \bar{\mathbf{d}}^{(k)} \tag{4.93}$$

and the search directions are given by:

$$\mathbf{d}^{(k+1)} = \mathbf{r}^{(k)} + \beta_k \mathbf{d}^{(k)} \tag{4.94}$$

$$\bar{\mathbf{d}}^{(k+1)} = \bar{\mathbf{r}}^{(k)} + \beta_k \bar{\mathbf{d}}^{(k)} \tag{4.95}$$

The parameters α_k and β_k are specified as:

$$\alpha_k = \frac{(\bar{\mathbf{r}}^{(k)})^T \mathbf{r}^{(k)}}{(\bar{\mathbf{d}}^{(k)})^T \mathbf{Z}\mathbf{d}^{(k)}} \tag{4.96}$$

$$\beta_k = \frac{(\bar{\mathbf{r}}^{(k+1)})^T \mathbf{r}^{(k+1)}}{(\bar{\mathbf{r}}^{(k)})^T \mathbf{r}^{(k)}} \tag{4.97}$$

The BiConjugate Gradient algorithm is described in Table (4.8) [14]. When the BiConjugate Gradient works, its convergence is comparable to that of GMRES, although requiring twice the number of matrix-vector multiplies per iteration. However the BiCG method has been shown to have an irregular performance in terms of convergence [16; 17; 21].

Table 4.8: BiCG Iteration

The BiConjugate Gradient Iterative Algorithm to solve matrix equation $\mathbf{Zx} = \mathbf{v}$

$\mathbf{x}^{(0)} = 0; \quad \mathbf{r}^{(0)} = \mathbf{v} - \mathbf{Z}\mathbf{x}^{(0)}$

choose $\quad \bar{\mathbf{r}}^{(0)} = \mathbf{r}^{(0)}$

set $\quad \mathbf{d}^{(0)} = \mathbf{r}^{(0)}; \quad \bar{\mathbf{d}}^{(0)} = \bar{\mathbf{r}}^{(0)}$

for $\quad k = 1, 2, \ldots$

$\alpha_k = \frac{(\bar{\mathbf{r}}^{(k-1)})^T \mathbf{r}^{(k-1)}}{(\bar{\mathbf{d}}^{(k)})^T \mathbf{Z}\mathbf{d}^{(k)}}$

$\mathbf{x}^{(k+1)} = \mathbf{x}^{(k)} + \alpha_k \mathbf{d}^{(k)}$

$\mathbf{r}^{(k+1)} = \mathbf{r}^{(k)} - \alpha_k \mathbf{Z}\mathbf{d}^{(k)}$

$\bar{\mathbf{r}}^{(k+1)} = \bar{\mathbf{r}}^{(k)} - \alpha_k \mathbf{Z}^T \bar{\mathbf{d}}^{(k)}$

$\beta_k = \frac{(\bar{\mathbf{r}}^{(k)})^T \mathbf{r}^{(k)}}{(\bar{\mathbf{r}}^{(k-1)})^T \mathbf{r}^{(k-1)}}$

$\mathbf{d}^{(k+1)} = \mathbf{r}^{(k)} + \beta_k \mathbf{d}^{(k)}$

$\bar{\mathbf{d}}^{(k+1)} = \bar{\mathbf{r}}^{(k)} + \beta_k \bar{\mathbf{d}}^{(k)}$

check if $\quad \frac{||\mathbf{r}^{(k+1)}||}{||\mathbf{v}||} < \text{tolerance}$

end

Other Conjugate Gradient method were also formulated, for example the Conjugate Gradient Squared Method (CGS) was introduced in order to avoid the use of $\mathbf{Z}^T$ in the BiConjugate Gradient algorithm and therefore obtaining a higher convergence rate at a similar computational cost. However the CGS method can introduce considerable rounding errors which lead to inaccurate results [17; 70].

This drawback of the CGS can be removed by another Krylov subspace method known as the Biconjugate Gradient Stabilised (BiCGSTAB). The BiCGSTAB employs the calculation of a steepest descent update, therefore leading to a much smoother convergence. It can be very effective. However its performance is quite irregular [17].

4.4 Preconditioning

The Krylov subspace methods, or the non stationary iterative techniques, have been described in Section 4.3. The convergence rate of these methods strongly depends on the spectral properties of the coefficient matrix [13; 16; 17; 21; 22]. It is possible to improve these spectral properties by using a preconditioner. A *preconditioner* is a matrix that transforms the original linear system into a system with better spectral properties, but such that the solution of the equivalent system remains the same. Consider the matrix equation $\mathbf{Zx} = \mathbf{v}$. Suppose $\mathbf{P}$ is the preconditioning matrix so that [17; 16; 21]:

$$\mathbf{P}^{-1}\mathbf{Zx} = \mathbf{P}^{-1}\mathbf{v} \tag{4.98}$$

It is obvious that this linear system has the same solution, but it may have the advantage of improved spectral properties for the new coefficient matrix $\mathbf{P}^{-1}\mathbf{Z}$. The convergence properties of the iterative methods used to solve the new equation will improve since they now depend on the eigenvalues of $\mathbf{P}^{-1}\mathbf{Z}$ and not the eigenvalues of $\mathbf{Z}$. When choosing a preconditioner it is important to ensure that it is somewhat an approximation of the matrix $\mathbf{Z}$ and that the construction of $\mathbf{P}^{-1}$ does not require excessive resources.

The effective design of preconditioners is still a challenging research area. There are various types of preconditioners. The iteration matrices of the stationary methods such as Jacobi or Gauss-Seidel are commonly employed as preconditioners.

The *Jacobi preconditioner* $\mathbf{P}_J$ is one of the simplest and most popular preconditioners used. $\mathbf{P}_J$ is constructed by the diagonal elements of $\mathbf{Z}$. A Block version is also available, where diagonal blocks are used in order to construct the preconditioner. The block Jacobi preconditioner is a block diagonal matrix [17]. The Jacobi preconditioner achieves a better conditioning of the coefficient matrix $\mathbf{P}_J^{-1}\mathbf{Z}$ without requiring large storage capacity.

Another well known preconditioning technique is the *SSOR preconditioner* and it has the following formulation [22; 18; 17]:

$$\mathbf{P}_{SSOR} = \frac{1}{2-\omega}\left(\frac{1}{\omega}\mathbf{D}+\mathbf{L}\right)\left(\frac{1}{\omega}\mathbf{D}\right)^{-1}\left(\frac{1}{\omega}\mathbf{D}+\mathbf{U}\right) \tag{4.99}$$

where $\mathbf{D}$ is the diagonal matrix containing the diagonal elements of $\mathbf{Z}$, $\mathbf{L}$ is the lower triangular portion of $\mathbf{Z}$ and $\mathbf{U}$ is the upper triangular portion of $\mathbf{Z}$. Block versions of the SSOR preconditioner can be used in the same manner as the Jacobi preconditioner. It has been observed that both Jacobi and SSOR preconditioners can significantly improve the convergence characteristics of the Krylov iterative methods [22; 71; 72; 73; 74].

Another class of preconditioners is represented by Incomplete Factorization Preconditioners or Incomplete LU Factorization (ILU). These methods are based on ignoring small elements contained in the $\mathbf{L}$ and $\mathbf{U}$ matrices. The $\mathbf{L}$ and $\mathbf{U}$ matrices are not composed of the lower or upper portions of the $\mathbf{Z}$ matrix. Consider $\mathbf{L}_{ILU}$ and $\mathbf{U}_{ILU}$ the new approximate lower and upper triangular portions of $\mathbf{Z}$. This leads to the following decomposition [11]:

$$\mathbf{Z} = \mathbf{L}_{ILU}\mathbf{U}_{ILU} + \mathbf{E} \tag{4.100}$$

where $\mathbf{E}$ contains the eliminated elements, therefore $||\mathbf{E}||$ is small. The preconditioner $\mathbf{P}_{ILU}$ has the form [11]:

$$\mathbf{P}_{ILU} = \mathbf{L}_{ILU}\mathbf{U}_{ILU} \tag{4.101}$$

The new term $\mathbf{P}_{ILU}^{-1}\mathbf{Z}$ can be expected to be very close to the identity matrix if $\mathbf{E}$ contains insignificantly small elements. The efficiency of the ILU preconditioner is much higher when $\mathbf{P}_{ILU}$ is close to the original $\mathbf{Z}$ matrix, as this requires less iteration for the iterative solvers. It is a popular method due to its simplicity, however it has a major drawback

caused by the high memory resources required for creating and storing $\mathbf{L}_{ILU}$ and $\mathbf{U}_{ILU}$ [75].

4.5 Application of the stationary methods to EM wave scattering

Many iterative methods have been developed for EM wave scattering problems in recent years. In many cases they are based on the stationary methods discussed in this chapter. In this section a few of these techniques are presented.

In [68] the Method of Ordered Multiple Interactions (MOMI) was presented. This method is based on the idea of superimposing a grid over the scattering surface and calculating the interactions between separate points on the grid. This iterative technique was applied to 2D perfectly electric conducting rough scatterers and it has been shown that the unknown currents could be calculated at a much faster rate as well as requiring much less storage capacity compared to direct inversion. Rino *et al.* have applied this method together with source-directed slice sampling to 3D scatterers in [76], concluding that it achieves poor convergence rate when applied to 3D objects. Tran [77] performs another study on the MOMI technique applied to 2D scatterers and observes that the MOMI depends on the ordering of the current elements and it tends to have a slower convergence rate for surfaces that exhibit the possibility of multiple scattering. A variation of MOMI referred to as the Forward-Backward (FB) method was introduced by Holliday *et al.* in [69]. This new algorithm is based on the idea of marching an estimate of surface currents forward and backward in order to build up a solution. West and Sturm have proven in [20] that both the MOMI and the FB methods for perfect electric conductors are equivalent to the Successive Symmetric Overrelaxation with the relaxation parameter set to 1.

The Forward-Backward method was initially applied to the Magnetic Field Integral Equation Formulation (MFIE) showing satisfactory results after only a few iterations when used to solve problems of electromagnetic wave scattering from closed perfect electric conductors. The efficiency of the FB method used in conjunction with the MFIE was again described in [78], this time applied to imperfect conductors.

The Forward-Backward technique employed in solving the EFIE is firstly presented in [69]. The FB approach combined with the EFIE is further investigated by Pino *et al.*

in [79], where a Generalised Forward-Backward (GFB) is applied to a PEC surface that contains one or more large arbitrarily shaped obstacles. The GFB represents a combination of Forward-Backward and MoM, whereby the fields along most of the scattering surface are computed using the FB approach, whereas MoM is applied around the obstacle. The GFB has been shown to provide high accuracy levels and low computational cost. However, this was shown to be true only for small problems, proving to be too inefficient for large obstacles.

Iodice [67] applied the Forward-Backward scheme to scattering from rough surfaces with arbitrary complex dielectric constants, proving that it delivers a high accuracy when applied to more difficult problems. He further investigated the applications of the Forward-Backward method for solving electromagnetic wave scattering problems from rough dielectric surfaces in [66], where he showed that the FB for dielectrics is equivalent to the Successive Symmetric Overrelaxation method as well as evaluating its convergence for a large number of realistic problems. In [64] and [65] it was shown that the number of iterations is highly dependent on the roughness of the surface. Therefore for relatively smooth surfaces a satisfactory result can be obtained after only a few iterations. A comparison between Jacobi preconditioned generalised FB, BiCGSTAB and GMRES is performed when solving the same problem as described by Pino *et al.* in [79], showing that the FB converges at a faster rate.

Another range of methods based on the splitting of the scattering surface include the Spatial Decomposition Technique [80], the Progressive Numerical Method [81] and the Multiple Sweep Method of Moments [82]. The Spatial Decomposition Technique (SDT) is a method based on the idea of splitting the surface of the scatterer into subregions, where the surface currents are calculated separately for each subregion. It introduces the advantage of not having to deal with one large matrix, but with a few smaller matrices. This technique is described by Umashankar in [80] and [83], where the SDT was applied to 2D perfect electric conductors and homogeneous dielectrics, showing that the SDT diminishes significantly the required computer resources compared to the MoM. The Progressive Numerical Method (PNM) is a similar technique based on the principle of splitting the surface of the scatterer into subregions. When applying the PNM the field distribution is calculated for the first

region, then this solution is used for the next subregion, then moving on to the next one, using the solution form the previous region and so on. This method is suggested by Shafai in [81]. This technique of splitting the surface of the scatterer into regions causes the error to increase towards the edges of the regions due to a lack of coupling effects from neighbouring regions. The PNM removes this disadvantage by overlapping the subregions. A comparison between the SDT and PNM when applied to 2D conducting objects is presented in [63] and [31], concluding that PNM is a more efficient and reliable method compared to the SDT. The PNM combined with a wideband analysis has been presented in [84], allowing to solve the scattering problem over a wide range of frequencies, where it is shown that not only does PNM provide efficient results, but it also decreases the CPU-time.

In [82] the Multiple Sweep Method of Moments (MSMM) is presented, which, similarly to the PNM and SDT, splits the scattering object into subsections and performs forward-backward current marching from subregion to subregion, rather than from point to point.

An improved Forward Backward method is presented in [85] referred to as hybridized Forward Backward, whereby an optimally sized correction step is introduced in the approximate direction of the largest eigenvector associated with the iteration matrix. The hybridized Forward Backward is shown to improve the convergence of the classical forward backward when applied to problems of electromagnetic wave scattering from P.E.C. structures.

In this work the Buffered Block Forward Backward (BBFB) Method is applied to solve the wave scattering problem. The BBFB introduces the novelty of computing the interactions between the neighbouring regions, therefore reducing the artificially induced edge effects.

4.6 Conclusion

A description of various iterative methods used to solve the matrix equation obtained after applying the MoM to the IE formulation has been presented in this Chapter. Both stationary and the non stationary iterative techniques have been described. A brief description of recent methods based on the surface splitting of the scatterer has also been presented. The main focus of this thesis is the Buffered Block Forward Backward method which is based on the Forward Backward algorithm, which in turn represents a version of the stationary Successive Symmetric Overrelaxation method. In the following chapters the Buffered Block Forward Backward Method will be applied to solving problems of EM scattering from perfect electric conductors, closed and open 2D homogeneous structures and 3D homogeneous dielectric objects. The convergence rate of the Buffered Block Forward Backward technique will also be compared to that of the non stationary iterative solvers.

Chapter 5

Buffered Block Forward Backward Method applied to Perfectly Conducting structures

5.1 Introduction

The efficient solution of the matrix equations produced when the method of moments is applied to the Electric Field Integral Equation (EFIE) is an essential topic in Computational Electromagnetics. In Chapter 4 the stationary and nonstationary iterative techniques used for solving this problem were presented. In this chapter the Buffered Block Forward Backward (BBFB) method is introduced. It is applied to problems of electromagnetic scattering from perfectly conducting structures and is compared to other Krylov methods.

The BBFB is based on the Forward Backward technique. The Forward Backward (FB) method has been presented in [69]. The FB method has been shown to be equivalent to the Symmetric Successive Overrelaxation (SSOR) methods when the relaxation parameter is $\omega = 1$ [20]. Extensive research has been performed on the efficiency of the FB technique when applied to various 2D scatterers ranging from perfect electric conductors to dielectrics [78; 64; 65; 66; 67] and it has been shown that the FB method achieves high convergence

speed when applied to appropriate 2D scatterers. The Block Forward Backward is another technique based on the FB approach whereby the currents are calculated not from point to point, but the scatterer is divided into subregions and the currents are marched from subregion to subregion. By partitioning the scattering surface false edges are introduced. [86] presents a modified block forward-backward approach based on overlapping subregions. When applying this technique the neighboring regions are considered as well in order to dampen any spurious diffraction caused by the false edges. Here this method is referred to as Buffered Block Forward Backward (BBFB) algorithm.

5.2 Review of Buffered Forward Backward Method

The Electric Field Integral Equation (EFIE) formulation has been presented in Chapter 3. The Method of Moments (MoM) with N basis and testing functions is then applied to the EFIE in order to obtain the matrix equation that is to be solved in order to calculate the unknown current density. For the matrix equation $\mathbf{ZJ} = \mathbf{V}$ the forward sweep of the Forward Backward method is given by:

$$Z_{ii}J_i^{k+\frac{1}{2}} = V_i - \sum_{j<i} Z_{ij}J_j^{(k+\frac{1}{2})} - \sum_{j>i} Z_{ij}J_j^{(k)} \quad \text{for} \quad i = 1, \ldots, N \tag{5.1}$$

while the backward sweep is given by:

$$Z_{ii}J_i^{(k+1)} = V_i - \sum_{j<i} Z_{ij}J_j^{(k+\frac{1}{2})} - \sum_{j>i} Z_{ij}J_j^{(k+1)} \quad \text{for} \quad i = N, \ldots, 1 \tag{5.2}$$

where N is the number of basis functions used to discretise the scatterer.

When considering a Block Forward Backward method the basis functions are grouped into M non-overlapping groups, numbered 1 to M, as can be seen in Figure (5.1). The currents are no longer calculated from point to point, but from subregion to subregion.

The interactions between groups m and n are given by the impedance submatrix $\tilde{\mathbf{Z}}_{mn}$. The subvector $\tilde{\mathbf{V}}_m$ represents the incident field on group m. Obviously, the groups chosen define a unique decomposition of the impedance matrix $\mathbf{Z}$ into blocks or submatrices.

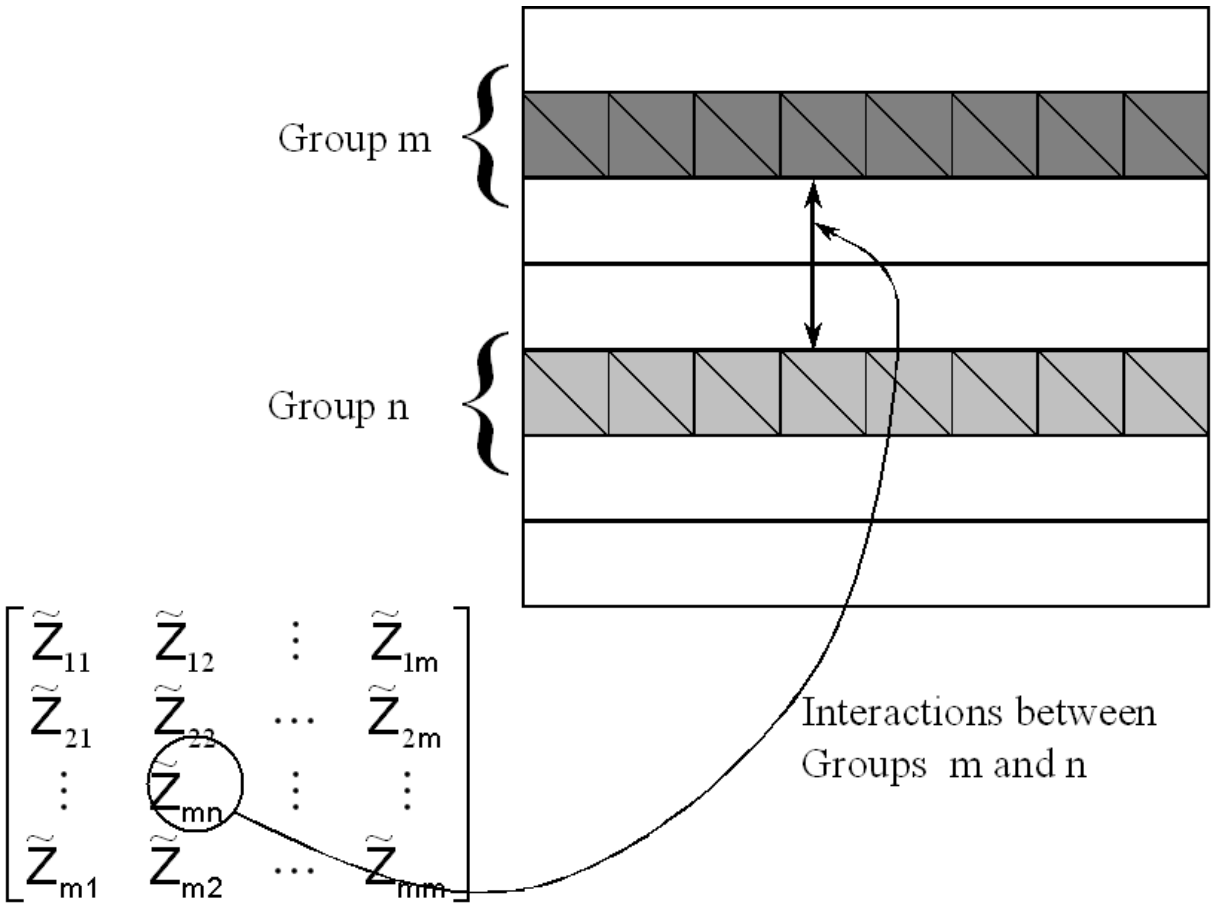

Figure 5.1: Metallic plate divided into subregions. The interactions between regions m and n are in the sub matrix $\tilde{\mathbf{Z}}_{mn}$

The Block Forward Backward method marches the solution from group to group, computes the fields scattered from other groups and updates the currents within each group, as described in Figure (5.2). The forward sweep of the BFB technique is described in equation (5.3):

$$\tilde{\mathbf{Z}}_{mm}\tilde{\mathbf{J}}_m^{(k+\frac{1}{2})} = \tilde{\mathbf{V}}_m - \sum_{n<m} \tilde{\mathbf{Z}}_{mn}\tilde{\mathbf{J}}_n^{(k+\frac{1}{2})} - \sum_{n>m} \tilde{\mathbf{Z}}_{mn}\tilde{\mathbf{J}}_n^{(k)} \quad \text{for} \quad m = 1, \ldots, M \tag{5.3}$$

The backward sweep of the BFB method is shown in equation (5.4)

$$\tilde{\mathbf{Z}}_{mm}\tilde{\mathbf{J}}_m^{(k+1)} = \tilde{\mathbf{V}}_m - \sum_{n<m} \tilde{\mathbf{Z}}_{mn}\tilde{\mathbf{J}}_n^{(k+\frac{1}{2})} - \sum_{n>m} \tilde{\mathbf{Z}}_{mn}\tilde{\mathbf{J}}_n^{(k+1)} \quad \text{for} \quad m = M, \ldots, 1 \tag{5.4}$$

Note that in Equations (5.3) and (5.4) the first part of the right hand side, namely $\tilde{\mathbf{V}}_m - \sum_{n<m} \tilde{\mathbf{Z}}_{mn}\tilde{\mathbf{J}}_n^{(k+\frac{1}{2})}$, is the same for the forward and the backward sweep. Therefore it needs to be calculated only once, thus reducing the computational effort of the method.

However the artificially introduced edges between each subregion produce unwanted edge effects which can cause the divergence of the method. This problem can be alleviated by including the interactions from the neighbouring regions, which yields the Buffered Block Forward Backward (BBFB) method. The neighbouring regions are referred to as buffers. Note that it is possible to develop the algorithm using buffer regions of arbitrary size. Indeed if we chose a buffer region of size zero it reduces to a standard Block Forward Backward algorithm. In what follows we assume the buffer region consists of the immediately neighbouring group in the forward or backward directions. This procedure is described in figure (5.3)

The BBFB $(k+1)^{st}$ iteration takes place in two steps. During the forward sweep the following matrix equation is sequentially solved for $i = 1...M-1$

$$\begin{bmatrix} \tilde{\mathbf{Z}}_{ii} & \tilde{\mathbf{Z}}_{i(i+1)} \\ \tilde{\mathbf{Z}}_{(i+1)i} & \tilde{\mathbf{Z}}_{(i+1)(i+1)} \end{bmatrix} \begin{bmatrix} \tilde{\mathbf{J}}_i^{(k+\frac{1}{2})} \\ \tilde{\mathbf{B}}_{i+1} \end{bmatrix} = \begin{bmatrix} \tilde{\mathbf{V}}_i \\ \tilde{\mathbf{V}}_{i+1} \end{bmatrix} - \begin{bmatrix} \tilde{\mathbf{L}}_i \\ \tilde{\mathbf{L}}_{i+1} \end{bmatrix} - \begin{bmatrix} \tilde{\mathbf{U}}_i \\ \tilde{\mathbf{U}}_{i+1} \end{bmatrix}$$

$\tilde{\mathbf{Z}}_{ij}$ is the submatrix of $\mathbf{Z}$ containing interactions between basis groupings i and j. $\tilde{\mathbf{J}}_i^{(k+\frac{1}{2})}$ is the $(k+\frac{1}{2})$ iterate estimate of the basis amplitudes in basis grouping i. $\tilde{\mathbf{L}}_i$ and $\tilde{\mathbf{U}}_i$ contain

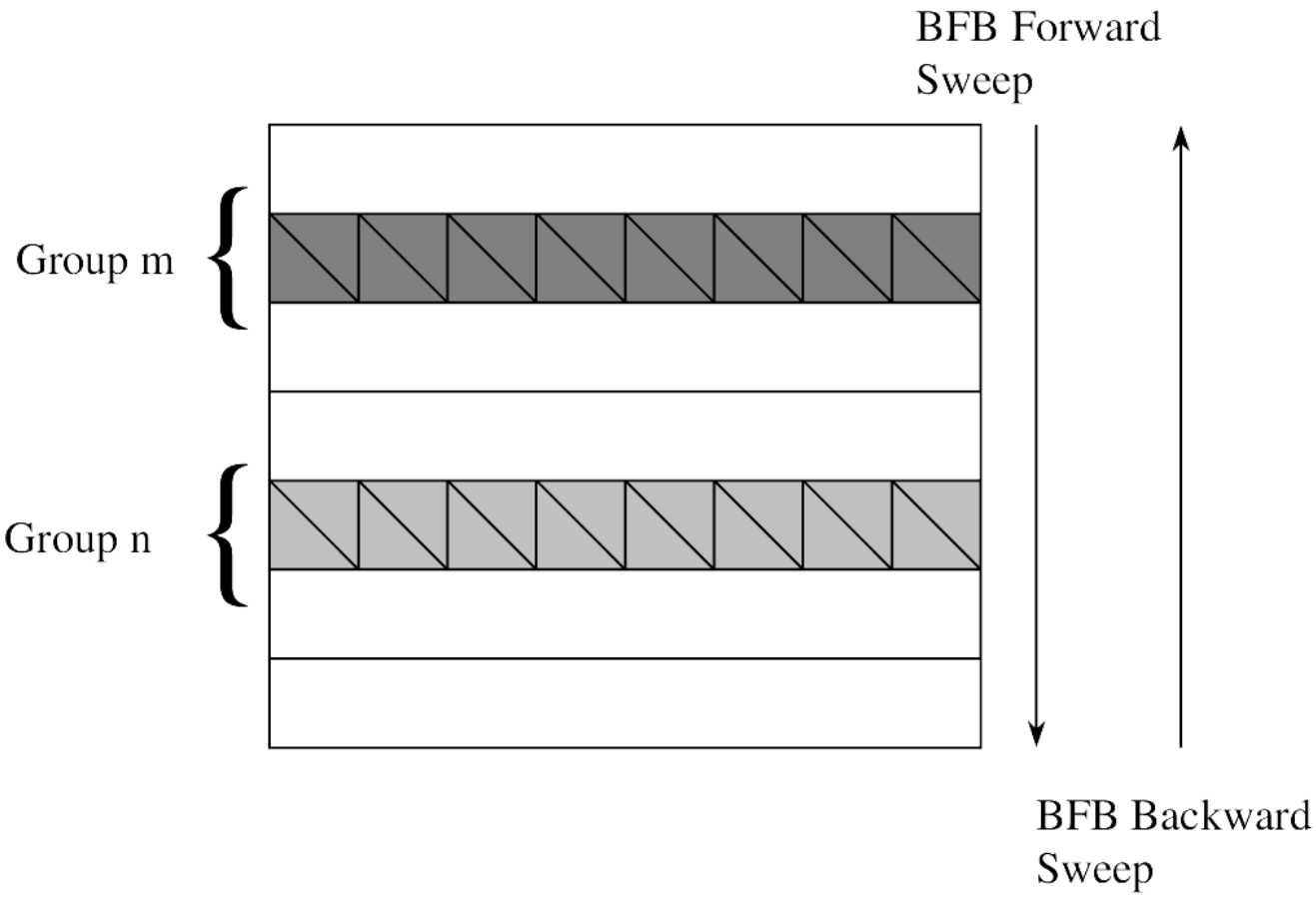

Figure 5.2: The Block Forward Backward method applied to a P.E.C. plate

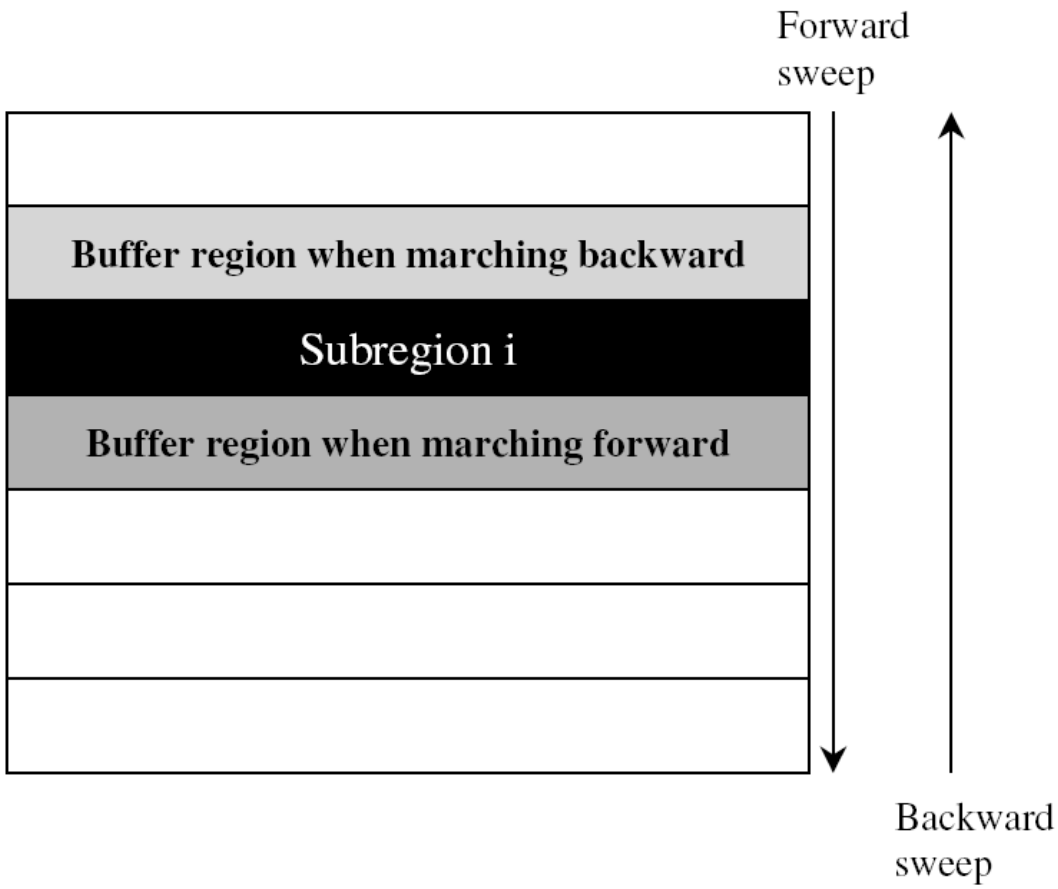

Figure 5.3: The Buffered Block Forward Backward Method applied to a P.E.C. plate.

information about fields scattered from other groups to group i.

$$\tilde{\mathbf{L}}_i = \sum_{j=1}^{i-1} \tilde{\mathbf{Z}}_{ij} \tilde{\mathbf{J}}_j^{(k+\frac{1}{2})} \tag{5.5}$$

$$\tilde{\mathbf{U}}_i = \sum_{j=i+2}^{M} \tilde{\mathbf{Z}}_{ij} \tilde{\mathbf{J}}_j^{(k)} \tag{5.6}$$

It is clear that group $(i+1)$ acts as a buffer region for group i in this forward sweep. The buffer region unknown $\tilde{\mathbf{B}}_{i+1}$, is a subvector of size n_{i+1}, where n_i is the number of unknowns in the ith group. Its role is to hold a temporary approximate solution for the currents in group $(i+1)$ in order to allow these currents to accurately couple with the currents in group i, removing, or at least damping, any spurious edge effects within this group. Group M does not require a buffer during the forward sweep and so the M^{th} problem to be solved in the forward sweep is given by:

$$\tilde{\mathbf{Z}}_{MM} \tilde{\mathbf{J}}_M^{(k+\frac{1}{2})} = \tilde{\mathbf{V}}_M - \sum_{j=1}^{M-1} \tilde{\mathbf{Z}}_{Mj} \tilde{\mathbf{J}}_j^{(k+\frac{1}{2})} \tag{5.7}$$

During the backward sweep the following matrix equation is sequentially solved for $i = M, ...2$:

$$\begin{bmatrix} \tilde{\mathbf{Z}}_{(i-1)(i-1)} & \tilde{\mathbf{Z}}_{(i-1)i} \\ \tilde{\mathbf{Z}}_{i(i-1)} & \tilde{\mathbf{Z}}_{ii} \end{bmatrix} \begin{bmatrix} \tilde{\mathbf{B}}_{i-1} \\ \tilde{\mathbf{J}}_i^{(k+1)} \end{bmatrix} = \begin{bmatrix} \tilde{\mathbf{V}}_{i-1} \\ \tilde{\mathbf{V}}_i \end{bmatrix} - \begin{bmatrix} \tilde{\mathbf{L}}_{i-1} \\ \tilde{\mathbf{L}}_i \end{bmatrix} - \begin{bmatrix} \tilde{\mathbf{U}}_{i-1} \\ \tilde{\mathbf{U}}_i \end{bmatrix}$$

where

$$\tilde{\mathbf{L}}_i = \sum_{j=1}^{i-2} \tilde{\mathbf{Z}}_{ij} \tilde{\mathbf{J}}_j^{(k+\frac{1}{2})} \tag{5.8}$$

$$\tilde{\mathbf{U}}_i = \sum_{j=i+1}^{M} \tilde{\mathbf{Z}}_{ij} \tilde{\mathbf{J}}_j^{(k+1)} \tag{5.9}$$

Group 1 does not require a buffer during the backward sweep and so the final problem to

be solved during the backward sweep is given by:

$$\tilde{\mathbf{Z}}_{11}\tilde{\mathbf{J}}_1^{(k+1)} = \tilde{\mathbf{V}}_1 - \sum_{j\geq 2} \tilde{\mathbf{Z}}_{1j}\tilde{\mathbf{J}}_j^{(k+1)} \tag{5.10}$$

5.2.1 Convergence Analysis

Given the matrix equation $\mathbf{ZJ} = \mathbf{V}$ where $\mathbf{Z}$ has the form:

$$\mathbf{Z} = \begin{bmatrix} \tilde{\mathbf{Z}}_{11} & \tilde{\mathbf{Z}}_{12} & \tilde{\mathbf{Z}}_{13} & \dots & \tilde{\mathbf{Z}}_{1m} \\ \tilde{\mathbf{Z}}_{21} & \tilde{\mathbf{Z}}_{22} & \tilde{\mathbf{Z}}_{23} & \dots & \tilde{\mathbf{Z}}_{2m} \\ \tilde{\mathbf{Z}}_{31} & \tilde{\mathbf{Z}}_{32} & \tilde{\mathbf{Z}}_{33} & \dots & \tilde{\mathbf{Z}}_{3m} \\ \tilde{\mathbf{Z}}_{41} & \tilde{\mathbf{Z}}_{42} & \tilde{\mathbf{Z}}_{43} & \dots & \tilde{\mathbf{Z}}_{4m} \\ \vdots & \vdots & \vdots & \vdots & \vdots \\ \tilde{\mathbf{Z}}_{m1} & \tilde{\mathbf{Z}}_{42} & \tilde{\mathbf{Z}}_{m3} & \dots & \tilde{\mathbf{Z}}_{mm} \end{bmatrix} \tag{5.11}$$

It is straightforward to verify that each forward sweep of the BBFB is equivalent to a forward sweep of an *unbuffered* block forward-backward method applied to the augmented matrix equation

$$\mathbf{Z}^f\mathbf{J}^f = \mathbf{V}^f \tag{5.12}$$

where

$$\mathbf{Z}^f = \left[\begin{array}{cc|cc|cc|c|c} \tilde{\mathbf{Z}}_{11} & \tilde{\mathbf{Z}}_{12} & 0 & 0 & \tilde{\mathbf{Z}}_{13} & 0 & \cdots & \tilde{\mathbf{Z}}_{1m} \\ \tilde{\mathbf{Z}}_{21} & \tilde{\mathbf{Z}}_{22} & 0 & 0 & \tilde{\mathbf{Z}}_{23} & 0 & \cdots & \tilde{\mathbf{Z}}_{2m} \\ \hline \tilde{\mathbf{Z}}_{21} & 0 & \tilde{\mathbf{Z}}_{22} & \tilde{\mathbf{Z}}_{23} & 0 & 0 & \cdots & \tilde{\mathbf{Z}}_{2m} \\ \tilde{\mathbf{Z}}_{31} & 0 & \tilde{\mathbf{Z}}_{32} & \tilde{\mathbf{Z}}_{33} & 0 & 0 & \cdots & \tilde{\mathbf{Z}}_{3m} \\ \hline \tilde{\mathbf{Z}}_{31} & 0 & \tilde{\mathbf{Z}}_{32} & 0 & \tilde{\mathbf{Z}}_{33} & \tilde{\mathbf{Z}}_{34} & \cdots & \tilde{\mathbf{Z}}_{3m} \\ \tilde{\mathbf{Z}}_{41} & 0 & \tilde{\mathbf{Z}}_{42} & 0 & \tilde{\mathbf{Z}}_{43} & \tilde{\mathbf{Z}}_{44} & \cdots & \tilde{\mathbf{Z}}_{4m} \\ \hline \vdots & \vdots & \vdots & \vdots & \vdots & \vdots & \vdots & \vdots \\ \hline \tilde{\mathbf{Z}}_{m1} & 0 & \tilde{\mathbf{Z}}_{m2} & 0 & \tilde{\mathbf{Z}}_{m3} & 0 & \cdots & \tilde{\mathbf{Z}}_{mm} \end{array}\right] \tag{5.13}$$

and

$$\mathbf{J}^f = \left[\begin{array}{cc|cc|c|c} \tilde{\mathbf{J}}_1 & \tilde{\mathbf{B}}_2 & \tilde{\mathbf{J}}_2 & \tilde{\mathbf{B}}_3 & \cdots & \tilde{\mathbf{J}}_M \end{array} \right]^T \tag{5.14}$$

$$\mathbf{V}_f = \left[\begin{array}{cc|cc|c|c} \tilde{\mathbf{V}}_1 & \tilde{\mathbf{V}}_2 & \tilde{\mathbf{V}}_2 & \tilde{\mathbf{V}}_3 & \cdots & \tilde{\mathbf{V}}_M \end{array} \right]^T \tag{5.15}$$

Horizontal and vertical lines are used to make explicit the blocks of $\mathbf{Z}_f$,$\mathbf{J}_f$ and $\mathbf{V}_f$ to be used during the unbuffered block forward sweep. In turn, it is straightforward to show that the unbuffered block forward sweep applied to equation (5.12) is equivalent to a forward sweep of the standard (point by point, rather than block by block) forward-backward method applied to a preconditioned version of equation (5.13). The preconditioner is a block diagonal matrix composed of the diagonal blocks of matrix (5.13).

From the resultant preconditioned matrix we can extract the following equation for $\mathbf{J}$.

$$\mathbf{YJ} = \mathbf{A} \tag{5.16}$$

The matrix $\mathbf{Y}$ has a block structure reflecting the basis groupings that have been imposed. Specifically, for $i < M$, $\tilde{\mathbf{Y}}_{ii}$ is a $n_i \times n_i$ identity matrix while $\tilde{\mathbf{Y}}_{i(i+1)} = 0$. For $j \notin \{i, i+1\}$ $\tilde{\mathbf{Y}}_{ij}$ is obtained by taking the first n_i rows of the $(n_i + n_{i+1}) \times n_j$ matrix

$$\left[\begin{array}{cc} \tilde{\mathbf{Z}}_{ii} & \tilde{\mathbf{Z}}_{i(i+1)} \\ \tilde{\mathbf{Z}}_{(i+1)i} & \tilde{\mathbf{Z}}_{(i+1)(i+1)} \end{array} \right]^{-1} \left[\begin{array}{c} \tilde{\mathbf{Z}}_{ij} \\ \tilde{\mathbf{Z}}_{(i+1)j} \end{array} \right] \tag{5.17}$$

For the special case $i = M$ we have

$$\tilde{\mathbf{Y}}_{ij} = \tilde{\mathbf{Z}}_{ii}^{-1} \tilde{\mathbf{Z}}_{ij} \tag{5.18}$$

It can be shown in a similar manner that the backward sweep of the BBFB is equivalent to a backward sweep of the standard (point by point, not block by block) forward - backward method applied to the matrix equation

$$\mathbf{WJ} = \mathbf{B} \tag{5.19}$$

For $i > 1$ $\tilde{\mathbf{W}}_{ii}$ is a $n_i \times n_i$ identity matrix while $\tilde{\mathbf{W}}_{i(i-1)} = 0$. For $j \notin \{i-1, i\}$ $\tilde{\mathbf{W}}_{ij}$ is obtained by taking the last n_i rows of the $(n_{i-1} + n_i) \times n_j$ matrix

$$\begin{bmatrix} \tilde{\mathbf{Z}}_{(i-1)(i-1)} & \tilde{\mathbf{Z}}_{(i-1)i} \\ \tilde{\mathbf{Z}}_{i(i-1)} & \tilde{\mathbf{Z}}_{ii} \end{bmatrix}^{-1} \begin{bmatrix} \tilde{\mathbf{Z}}_{(i-1)j} \\ \tilde{\mathbf{Z}}_{ij} \end{bmatrix} \tag{5.20}$$

For the special case $i = 1$ we have

$$\tilde{\mathbf{W}}_{ij} = \tilde{\mathbf{Z}}_{ii}^{-1} \tilde{\mathbf{Z}}_{ij} \tag{5.21}$$

The structure of the vectors $\mathbf{A}$ and $\mathbf{B}$ are similar but unimportant as they do not affect the convergence properties of the method. The iteration matrix $\mathbf{M}$ is defined as:

$$\mathbf{M} = (\mathbf{D}_W - \mathbf{U}_W)^{-1} \mathbf{L}_W (\mathbf{D}_Y - \mathbf{L}_Y)^{-1} \mathbf{U}_Y \tag{5.22}$$

where $\mathbf{D}_W$, $\mathbf{L}_W$ and $\mathbf{U}_W$ are the diagonal, lower triangular and upper triangular parts of the matrix $\mathbf{W}$ with similar definitions applying to $\mathbf{D}_Y$, $\mathbf{L}_Y$ and $\mathbf{U}_Y$. It is thus possible to state that $\boldsymbol{\epsilon}^{(k)}$ (defined as $\mathbf{J} - \mathbf{J}^{(k)}$, the error vector after the k^{th} complete BBFB iteration) evolves as

$$\boldsymbol{\epsilon}^{(k+1)} = \mathbf{M} \epsilon^{(k)} \tag{5.23}$$

Hence it is shown that the BBFB method will converge if the eigenvalues of $\mathbf{M}$ all have a magnitude less than 1. The convergence of the method is thus independent on the source location. The numerical experiments carried out for this thesis suggest that the convergence rate can be improved by choosing larger buffer regions, though at the cost of increased computation times.

5.2.2 Results

A wedge is created by joining two perfectly conducting flat plates of side $3\lambda \times 3\lambda$ (at $f = 300MHz$) along a common edge. One plate is in the xy plane with opposite corners at $(-0.5, -0.5, 0)$ and $(2.5, 2.5, 0)$. The common edge runs from $(-0.5, 2.5, 0)$ to $(2.5, 2.5, 0)$

and the inclination of the second plate is allowed to vary by setting the wedge interior angle α as can be seen in figure (5.4). A vertical half wavelength dipole source was placed at $(0, -11/\sqrt{3}, 10)$.

The 4200 basis functions were divided into 18 groups of roughly equal size, each strip running in the x direction as can be seen in figure (5.4). The BBFB method described in this chapter was compared to a conjugate gradient normal equations (CGNE) solver. The CGNE solver used a block diagonal preconditioner, where each block was based on three BBFB basis groupings, whereby each main subregion contained 3 groups and the buffer for each subregion contained one neighbouring group

$$\mathbf{P} = \begin{bmatrix}
\tilde{\mathbf{Z}}_{(1)(1)} & \tilde{\mathbf{Z}}_{(1)(2)} & \tilde{\mathbf{Z}}_{(1)(3)} & 0 & \dots & \dots & \dots & \dots & \dots & \dots & 0 \\
\tilde{\mathbf{Z}}_{(2)(1)} & \tilde{\mathbf{Z}}_{(2)(2)} & \tilde{\mathbf{Z}}_{(2)(3)} & 0 & \dots & \dots & \dots & \dots & \dots & \dots & 0 \\
\tilde{\mathbf{Z}}_{(3)(1)} & \tilde{\mathbf{Z}}_{(3)(2)} & \tilde{\mathbf{Z}}_{(3)(3)} & 0 & \dots & \dots & \dots & \dots & \dots & \dots & 0 \\
0 & 0 & 0 & \tilde{\mathbf{Z}}_{(4)(4)} & \tilde{\mathbf{Z}}_{(4)(5)} & \tilde{\mathbf{Z}}_{(4)(6)} & 0 & \dots & \dots & \dots & 0 \\
0 & 0 & 0 & \tilde{\mathbf{Z}}_{(5)(4)} & \tilde{\mathbf{Z}}_{(5)(5)} & \tilde{\mathbf{Z}}_{(5)(6)} & 0 & \dots & \dots & \dots & 0 \\
0 & 0 & 0 & \tilde{\mathbf{Z}}_{(6)(4)} & \tilde{\mathbf{Z}}_{(6)(5)} & \tilde{\mathbf{Z}}_{(6)(6)} & 0 & \dots & \dots & \dots & 0 \\
\vdots & \vdots & \vdots & \dots & \dots & \dots & \ddots & \dots & \vdots & \dots & \vdots \\
\dots & \vdots & \vdots & \vdots & \vdots & \vdots & \vdots & \vdots & \tilde{\mathbf{Z}}_{(16)(16)} & \tilde{\mathbf{Z}}_{(16)(17)} & \tilde{\mathbf{Z}}_{(16)(18)} \\
0 & \dots & \dots & \dots & \dots & \vdots & \vdots & \vdots & \tilde{\mathbf{Z}}_{(17)(16)} & \tilde{\mathbf{Z}}_{(17)(17)} & \tilde{\mathbf{Z}}_{(17)(18)} \\
0 & \dots & \dots & \dots & \dots & \dots & \vdots & \dots & \tilde{\mathbf{Z}}_{(18)(16)} & \tilde{\mathbf{Z}}_{(18)(17)} & \tilde{\mathbf{Z}}_{(18)(18)}
\end{bmatrix} \tag{5.24}$$

Figures (5.5) and (5.6) depict the normalised error $\log_{10} \frac{||\mathbf{V}-\mathbf{Z}\mathbf{J}^{BBFB}||}{||\mathbf{V}||}$, where $\mathbf{J}^{BBFB}$ is the surface current density calculated using the BBFB approach. In order to provide a fair comparison between the two methods, the normalised errors are plotted against the number of complex multiplications required per iteration. It can be seen that the BBFB converges significantly quicker than the CGNE though the convergence rate slows as the wedge angle diminishes as can be seen in Figure (5.6(a)).

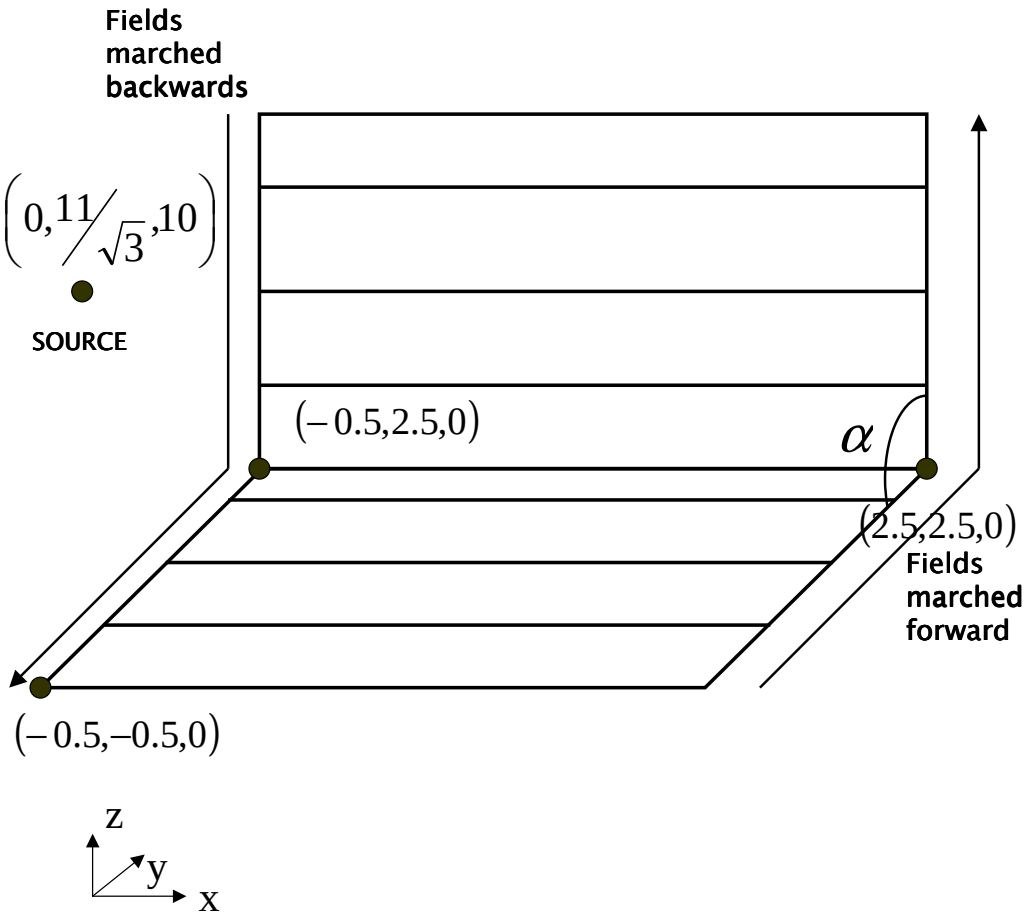

Figure 5.4: Buffered Block Forward Backward Method applied to a wedge of perfectly conducting plates.

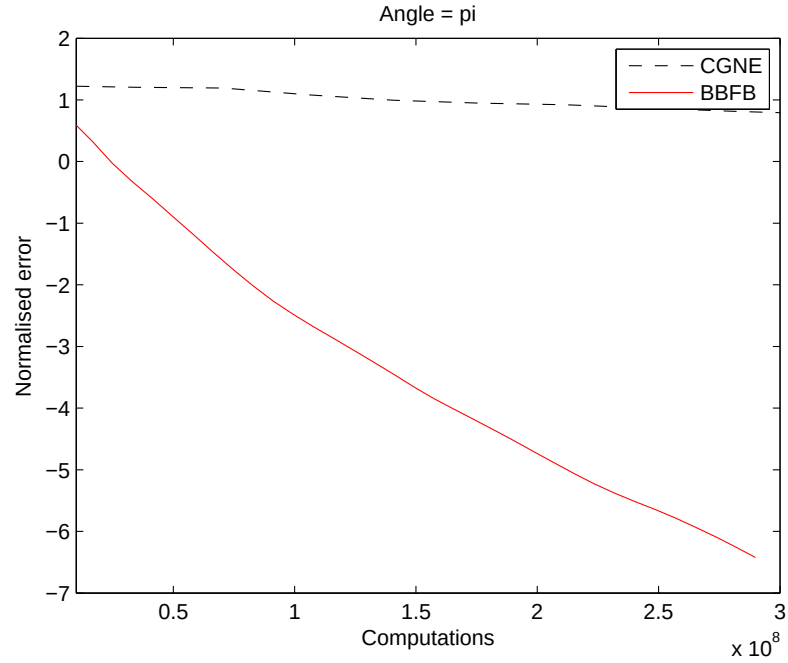

(a) Wedge angle $\alpha = \pi$

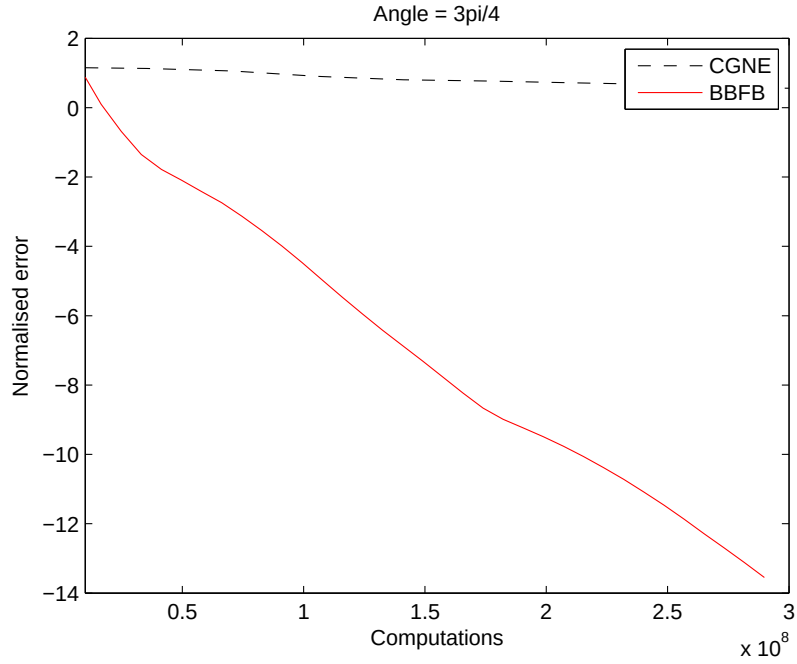

(b) Wedge angle $\alpha = 3\pi/4$

Figure 5.5: Average boundary condition error against number of computations

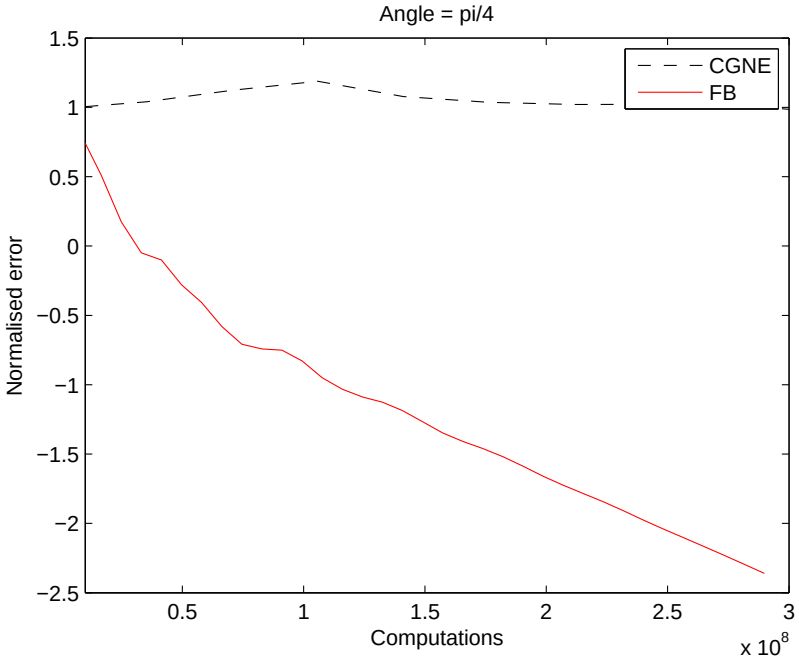

(a) Wedge angle $\alpha = \pi/4$

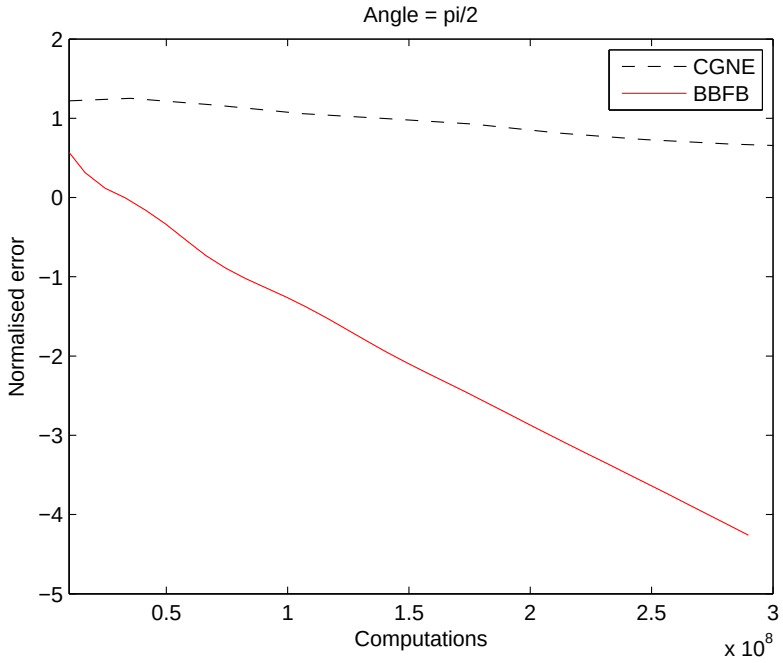

(b) Wedge angle $\alpha = \pi/2$

Figure 5.6: Average boundary condition error against number of computations

5.3 Conclusion

In this Chapter the Buffered Block Forward Backward Method is introduced. The BBFB technique is a variation of the Forward Backward method, which in turn is equivalent to Symmetric Successive Overrelaxation with the relaxation parameter ω set to 1. The Block Forward Backward Method is a block variation of the Forward Backward solver, whereby the basis functions are grouped into subregions and the BFB marches the currents from subregion to subregion, rather than from basis function to basis function. The Buffered Block Forward Backward technique introduces the novelty of computing the interactions between the neighbouring subregions as well, thus reducing the edge effects induced artificially when grouping the basis functions. It is shown that the BBFB technique is independent of incident source positioning

The BBFB is applied to a wedge composed of two perfectly conducting plates. The structure is partitioned into 18 subregions, which are grouped together in groups of 3. Each group has 1 neighbouring subregion acting as a buffer. The angle between the plates is modified in order to assess the performance of the BBFB. The results suggest the the BBFB is very effective in terms of normalised error. It reaches satisfactory error even when the angle between the plates is diminishing. The BBFB was also compared against preconditioned CGNE and it is shown that the BBFB has a much higher convergence rate.

Chapter 6

BBFB applied to 2D dielectric scatterers

6.1 Introduction

The Buffered Block Forward Backward method applied to a P.E.C. structure was presented in Chapter 5. In this Chapter the BBFB is extended to the problem of scattering from 2D homogeneous dielectric objects. The coupled Electric Field Integral Equation (EFIE) formulation is used. While scattering from a perfectly conducting object can be described in terms of a single integral equation describing fields external to the scatterer, scattering from a homogeneous dielectric body is described in terms of Coupled Electric Field Integral Equations involving expressions for both interior and exterior fields.

6.1.1 Coupled Electric Field Integral Equations for homogeneous dielectric bodies

The problem of scattering from a dielectric homogeneous body can be formulated using the Coupled Electric Field Integral Equations. The derivation of these equations has been presented in Sections 3.1.5 and 3.2.3 and they are briefly summarised below.

$$E_z^{inc}(t) = K^t(t) + jk_0\eta_0 A_z^{(0)} + \{\frac{\partial F_y^{(0)}}{\partial x} - \frac{\partial F_x^{(0)}}{\partial y}\}_{S^+} \tag{6.1}$$

$$0 = -K^t(t) + jk_d\eta_d A_z^{(d)} + \{\frac{\partial F_y^{(d)}}{\partial x} - \frac{\partial F_x^{(d)}}{\partial y}\}_{S^-} \tag{6.2}$$

The formulation invokes the surface equivalence principle and expresses the fields interior and exterior to the scatterer in terms of vector potentials **A** and **F** [3]:

$$A_z^{(i)} = \int J_z(t^{'})\frac{1}{4j}H_0^{(2)}(k_i R)dt^{'} \tag{6.3}$$

$$\bar{\mathbf{F}}_t^{(i)} = \int \hat{t}(t^{'})K_t(t^{'})\frac{1}{4j}H_0^{(2)}(k_i R)dt^{'} \tag{6.4}$$

These potentials are written in terms of tangential magnetic field (electric current **J**) and the tangential electric field (the so called magnetic current **K**). $\hat{t}(t')$ represents a unit vector tangent to the contour of the 2D scatterer.

Consider a homogeneous dielectric scatterer as presented in Figure (6.1). The method of moments with N pulse basis functions and Dirac Delta testing functions is applied whereby the scatterer is now described by flat segments as presented in Figure (6.2(a)). This yields:

$$\begin{bmatrix} \mathbf{A} & \mathbf{B} \\ \mathbf{C} & \mathbf{D} \end{bmatrix} \begin{bmatrix} \mathbf{j} \\ \mathbf{k} \end{bmatrix} = \begin{bmatrix} \mathbf{E} \\ \mathbf{0} \end{bmatrix} \tag{6.5}$$

Each of **A**, **B**, **C**, **D** is a $N \times N$ matrix having the elements [3]:

$$A_{mn} = \frac{k_0\eta_0}{4}\int_{\text{cell n}} H_0^{(2)}(k_0 R)dt^{'} \tag{6.6}$$

$$B_{mm} = \frac{1}{2} \tag{6.7}$$

$$B_{mn} = \frac{k_0}{4j}\int_{\text{cell n}} (\cos\phi_n\frac{\Delta x}{R_m} + \sin\phi_n\frac{\Delta y}{R_m})H_1^{(2)}(k_0 R_m)dt^{'} \tag{6.8}$$

$$C_{mn} = \frac{k_d \eta_d}{4} \int_{\text{cell n}} H_0^{(2)}(k_d R) dt' \tag{6.9}$$

$$D_{mm} = -\frac{1}{2} \tag{6.10}$$

$$D_{mn} = \frac{k_d}{4j} \int_{\text{cell n}} (\cos\phi_n \frac{\Delta x}{R_m} + \sin\phi_n \frac{\Delta y}{R_m}) H_1^{(2)}(k_d R_m) dt' \tag{6.11}$$

(x_m, y_m) is the centre of segment m, and ϕ_n is the polar angle of the normal vector $\hat{\mathbf{n}}$ to the segment n and these parameters are schematically presented in Figure (6.2(b)). Δx and Δy are given by:

$$\Delta x = x_m - x(t') \tag{6.12}$$

$$\Delta y = y_m - y(t') \tag{6.13}$$

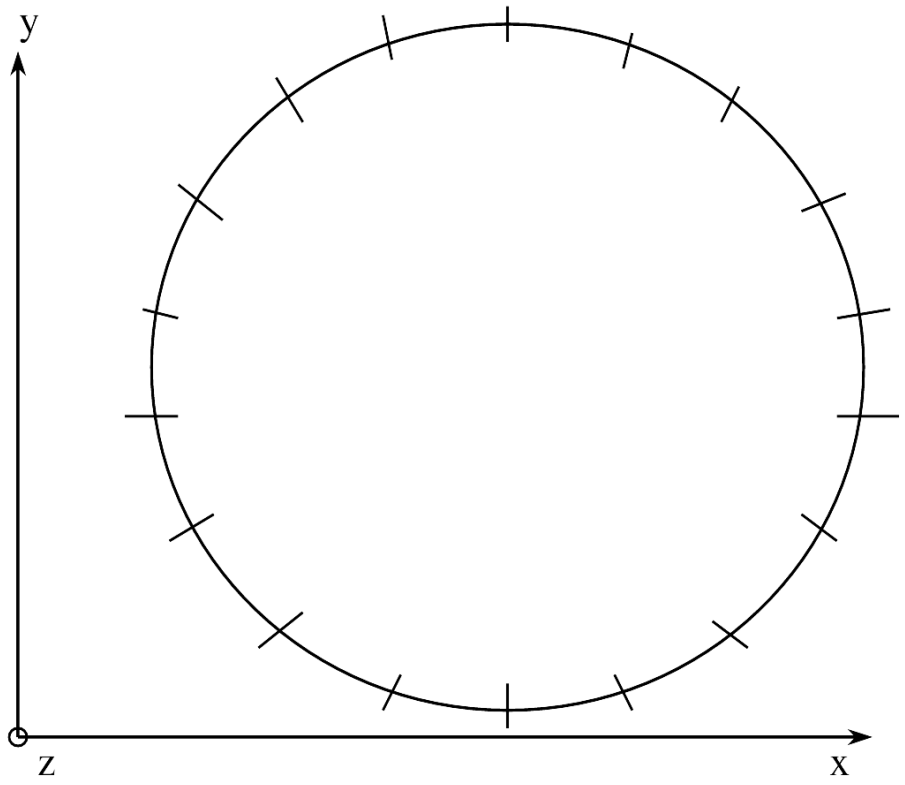

Figure 6.1: Homogeneous Dielectric scatterer.

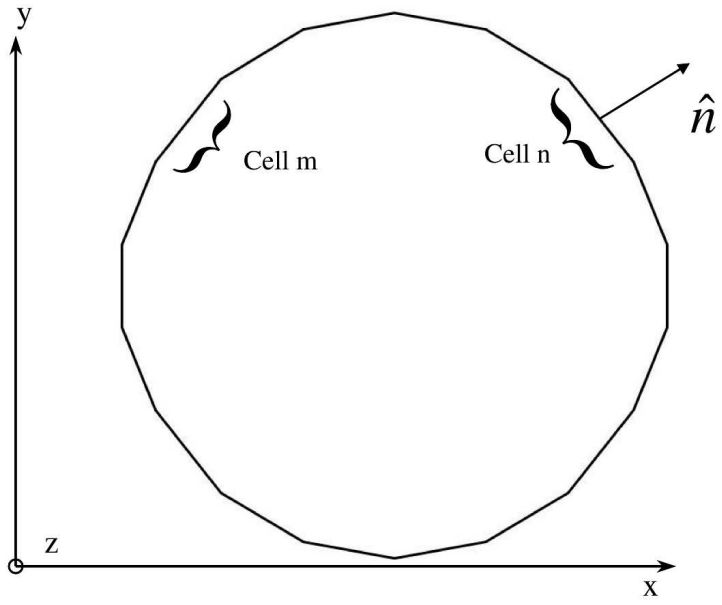

(a)

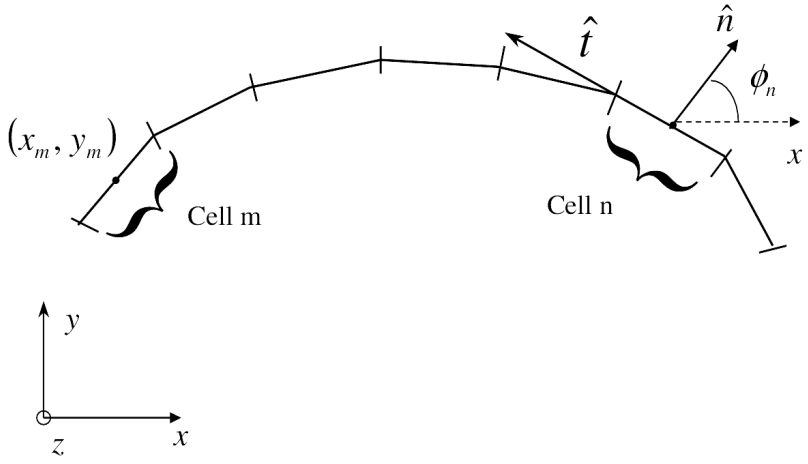

(b) Cells m and n of the discretised homogeneous scatterer

Figure 6.2: A homogeneous dielectric scatterer discretised into flat cells.

6.2 Buffered Block Forward Backward Method

In order to best describe the BBFB method we explicitly rewrite equation (6.5) illustrating the matrix entries:

$$\begin{bmatrix} A_{11} & A_{12} & A_{13} & \dots & A_{1N} & B_{11} & B_{12} & B_{13} & \dots & B_{1N} \\ A_{21} & A_{22} & A_{23} & \dots & A_{2N} & B_{21} & B_{22} & B_{23} & \dots & B_{2N} \\ \vdots & \vdots & \vdots & \vdots & \vdots & \vdots & \vdots & \vdots & \vdots & \vdots \\ A_{N1} & A_{N2} & A_{N3} & \dots & A_{NN} & B_{N1} & B_{N2} & B_{N3} & \dots & B_{NN} \\ C_{11} & C_{12} & C_{13} & \dots & C_{1N} & D_{11} & D_{12} & D_{13} & \dots & D_{1N} \\ C_{21} & C_{22} & C_{23} & \dots & C_{2N} & D_{21} & D_{22} & D_{23} & \dots & D_{2N} \\ \vdots & \vdots & \vdots & \vdots & \vdots & \vdots & \vdots & \vdots & \vdots & \vdots \\ C_{N1} & C_{N2} & C_{N3} & \dots & C_{NN} & D_{N1} & D_{N2} & D_{N3} & \dots & D_{NN} \end{bmatrix} \begin{bmatrix} j_1 \\ j_2 \\ \vdots \\ j_N \\ k_1 \\ k_2 \\ \vdots \\ k_N \end{bmatrix} = \begin{bmatrix} E_1 \\ E_2 \\ \vdots \\ E_N \\ 0 \\ 0 \\ \vdots \\ 0 \end{bmatrix}$$

The unknowns can be rearranged to sequentially run through the unknowns in each domain j_1, k_1, j_2, k_2,..., j_N, k_N rather than first running through the unknown electric current amplitudes j_1, j_2,..., j_N and then the magnetic current amplitudes k_1, k_2,..., k_N. This rearrangement yields:

$$\begin{bmatrix} A_{11} & B_{11} & A_{12} & B_{12} & A_{13} & B_{13} & \dots & A_{1N} & B_{1N} \\ C_{11} & D_{11} & C_{12} & D_{12} & C_{13} & D_{13} & \dots & C_{1N} & D_{1N} \\ A_{21} & B_{21} & A_{22} & B_{22} & A_{23} & B_{23} & \dots & A_{2N} & B_{2N} \\ C_{21} & D_{21} & C_{22} & D_{22} & C_{23} & D_{23} & \dots & C_{2N} & D_{2N} \\ \vdots & \vdots & \vdots & \vdots & \vdots & \vdots & \vdots & \vdots & \vdots \\ A_{N1} & B_{N1} & A_{N2} & B_{N2} & A_{N3} & B_{N3} & \dots & A_{NN} & B_{NN} \\ C_{N1} & D_{N1} & C_{N2} & D_{N2} & C_{N3} & D_{N3} & \dots & C_{NN} & D_{NN} \end{bmatrix} \begin{bmatrix} j_1 \\ k_1 \\ j_2 \\ k_2 \\ \vdots \\ j_N \\ k_N \end{bmatrix} = \begin{bmatrix} E_1 \\ 0 \\ E_2 \\ 0 \\ \vdots \\ E_N \\ 0 \end{bmatrix}$$

This can be re-written more compactly as:

$$\begin{bmatrix} \mathbf{Z}_{11} & \mathbf{Z}_{12} & \dots & \mathbf{Z}_{1N} \\ \mathbf{Z}_{21} & \mathbf{Z}_{22} & \dots & \mathbf{Z}_{2N} \\ \vdots & \vdots & \vdots & \vdots \\ \mathbf{Z}_{N1} & \mathbf{Z}_{N2} & \dots & \mathbf{Z}_{NN} \end{bmatrix} \begin{bmatrix} \mathbf{J}_1 \\ \mathbf{J}_2 \\ \vdots \\ \mathbf{J}_N \end{bmatrix} = \begin{bmatrix} \mathbf{V}_1 \\ \mathbf{V}_2 \\ \vdots \\ \mathbf{V}_N \end{bmatrix} \tag{6.14}$$

where $\mathbf{Z}_{mn}$ is a 2×2 matrix containing interactions between the unknowns j_m, k_m and j_n, k_n.

$$\mathbf{Z}_{mn} = \begin{bmatrix} A_{mn} & B_{mn} \\ C_{mn} & D_{mn} \end{bmatrix} \tag{6.15}$$

If we group basis function domains together into M groupings each containing $\frac{N}{M}$ basis functions we can write a block version of equation (6.14) as:

$$\begin{bmatrix} \tilde{\mathbf{Z}}_{11} & \tilde{\mathbf{Z}}_{12} & \dots & \tilde{\mathbf{Z}}_{1M} \\ \tilde{\mathbf{Z}}_{21} & \tilde{\mathbf{Z}}_{22} & \dots & \tilde{\mathbf{Z}}_{2M} \\ \vdots & \vdots & \vdots & \vdots \\ \tilde{\mathbf{Z}}_{M1} & \tilde{\mathbf{Z}}_{M2} & \dots & \tilde{\mathbf{Z}}_{MM} \end{bmatrix} \begin{bmatrix} \tilde{\mathbf{J}}_1 \\ \tilde{\mathbf{J}}_2 \\ \vdots \\ \tilde{\mathbf{J}}_M \end{bmatrix} = \begin{bmatrix} \tilde{\mathbf{V}}_1 \\ \tilde{\mathbf{V}}_2 \\ \vdots \\ \tilde{\mathbf{V}}_M \end{bmatrix} \tag{6.16}$$

where $\tilde{\mathbf{Z}}_{mn}$ contains the interactions between all basis functions in groups m and n. A forward-backward solver finds a global solution by solving a sequence of problems, each one describing the surface current in one grouping. By "marching" the currents forward and backward from group to group a solution can be found in a manner that can be more efficient than using other iterative solvers. A block forward backward proceeds by:

$$\tilde{\mathbf{Z}}_{mm}\tilde{\mathbf{J}}_m^{(k+\frac{1}{2})} = \tilde{\mathbf{V}}_m - \sum_{n<m} \tilde{\mathbf{Z}}_{mn}\tilde{\mathbf{J}}_n^{(k+\frac{1}{2})} - \sum_{n>m} \tilde{\mathbf{Z}}_{mn}\tilde{\mathbf{J}}_n^{(k)} \tag{6.17}$$

$$\tilde{\mathbf{Z}}_{mm}\tilde{\mathbf{J}}_m^{(k+1)} = \tilde{\mathbf{V}}_m - \sum_{n<m} \tilde{\mathbf{Z}}_{mn}\tilde{\mathbf{J}}_n^{(k+\frac{1}{2})} - \sum_{(n>m)} \tilde{\mathbf{Z}}_{mn}\tilde{\mathbf{J}}_n^{(k+1)} \tag{6.18}$$

In Chapter 5 the Buffer Block Forward Backward method was presented. This algo-

rithm was firstly introduced in [86] and [87] and it represents a variation of the block successive overrelaxation method. As has been described in Section 5.2, rather than solving for the unknowns in each group individually the interactions with neighboring groups (referred to as buffer regions) are included in order to suppress spurious diffraction effects that would otherwise arise and cause the solution to diverge. Recall that the forward sweep of the BBFB scheme is given by [87]:

$$\begin{bmatrix} \tilde{\mathbf{Z}}_{mm} & \tilde{\mathbf{Z}}_{m(m+1)} \\ \tilde{\mathbf{Z}}_{(m+1)m} & \tilde{\mathbf{Z}}_{(m+1)(m+1)} \end{bmatrix} \begin{bmatrix} \tilde{\mathbf{J}}_m^{(k+\frac{1}{2})} \\ \tilde{\mathbf{B}}_{m+1} \end{bmatrix} = \begin{bmatrix} \tilde{\mathbf{V}}_m \\ \tilde{\mathbf{V}}_{m+1} \end{bmatrix} - \begin{bmatrix} \tilde{\mathbf{L}}_m \\ \tilde{\mathbf{L}}_{m+1} \end{bmatrix} - \begin{bmatrix} \tilde{\mathbf{U}}_m \\ \tilde{\mathbf{U}}_{m+1} \end{bmatrix}$$

In the forward sweep group $m+1$ acts as a buffer zone for group m. $\tilde{\mathbf{B}}_{m+1}$ is a dummy unknown used to temporarily compute the unknowns in group $m+1$ in order to allow their accurate interaction with the unknowns in group m. The last two quantities on the right incorporate scattering from other groups and are given by:

$$\begin{bmatrix} \tilde{\mathbf{L}}_m \\ \tilde{\mathbf{L}}_{m+1} \end{bmatrix} = \begin{bmatrix} \sum_{n<m} \tilde{\mathbf{Z}}_{mn} \tilde{\mathbf{J}}_n^{(k+\frac{1}{2})} \\ \sum_{n<m} \tilde{\mathbf{Z}}_{(m+1)n} \tilde{\mathbf{J}}_n^{(k+\frac{1}{2})} \end{bmatrix} \tag{6.19}$$

$$\begin{bmatrix} \tilde{\mathbf{U}}_m \\ \tilde{\mathbf{U}}_{m+1} \end{bmatrix} = \begin{bmatrix} \sum_{n>m+1} \tilde{\mathbf{Z}}_{mn} \tilde{\mathbf{J}}_n^{(k+\frac{1}{2})} \\ \sum_{n>m+1} \tilde{\mathbf{Z}}_{(m+1)n} \tilde{\mathbf{J}}_n^{(k+\frac{1}{2})} \end{bmatrix} \tag{6.20}$$

In the backward sweep the group $m-1$ acts as a buffer for group m and the process is updated as:

$$\begin{bmatrix} \tilde{\mathbf{Z}}_{(m-1)(m-1)} & \tilde{\mathbf{Z}}_{(m-1)m} \\ \tilde{\mathbf{Z}}_{m(m-1)} & \tilde{\mathbf{Z}}_{mm} \end{bmatrix} \begin{bmatrix} \tilde{\mathbf{B}}_{m-1} \\ \tilde{\mathbf{J}}_m^{(k+1)} \end{bmatrix} = \begin{bmatrix} \tilde{\mathbf{V}}_{m-1} \\ \tilde{\mathbf{V}}_m \end{bmatrix} - \begin{bmatrix} \tilde{\mathbf{L}}_{m-1} \\ \tilde{\mathbf{L}}_m \end{bmatrix} - \begin{bmatrix} \tilde{\mathbf{U}}_{m-1} \\ \tilde{\mathbf{U}}_m \end{bmatrix} \tag{6.21}$$

where the lower sum in $\tilde{\mathbf{L}}$ is now over $n < m-1$ and upper sum in $\tilde{\mathbf{U}}$ is over $n > m$ given

by:

$$\tilde{\mathbf{L}}_m = \sum_{n<m-1} \tilde{\mathbf{Z}}_{mn}\tilde{\mathbf{J}}_n^{(k+\frac{1}{2})} \tag{6.22}$$

$$\tilde{\mathbf{U}}_m = \sum_{n>m} \tilde{\mathbf{Z}}_{mn}\tilde{\mathbf{J}}_n^{(k+1)} \tag{6.23}$$

6.2.1 Mie series

In order to validate our implementation of the MoM, we choose to compare it against the analytical Mie series approach. The Mie series allows the computation of the exact fields at any point interior or exterior to a sphere. In particular we use it to compute the surface fields and hence current densities. The Mie series approach can only be applied to 2D and 3D spheres [88], although other modal solutions are available for other canonical surfaces.

Consider a homogeneous dielectric 2D sphere and a TM^z plane wave incident field propagating in the x direction as shown in Figure (6.3), where r is the radius of the cylinder, and (P, ϕ) is the coordinate of the field point in cylindrical coordinates. The region exterior to the scatterer is free space described by the parameters ε_0 and μ_0 and the sphere has material parameters ε and μ. The total field at point P can be expressed as:

$$E^{tot} = E^{inc} + E^s \tag{6.24}$$

where the subscript z is omitted as it is understood that all electric fields are in the $\hat{k}$ direction

The incident field can be expressed as:

$$E^{inc} = e^{-\jmath k_0 \rho \cos\phi} = \sum_{n=-\infty}^{\infty} \jmath^{-n} J_n(k_0\rho) e^{\jmath n\phi} \tag{6.25}$$

where $J_n(k_0\rho)$ is the Bessel function of nth order and k_0 is the wavenumber in free space. The scattered field external to the cylinder can be described by equation (6.26)

$$E^s = \sum_{n=-\infty}^{\infty} \jmath^{-n} A_n H_n^{(2)}(k_0\rho) e^{\jmath n\phi} \tag{6.26}$$

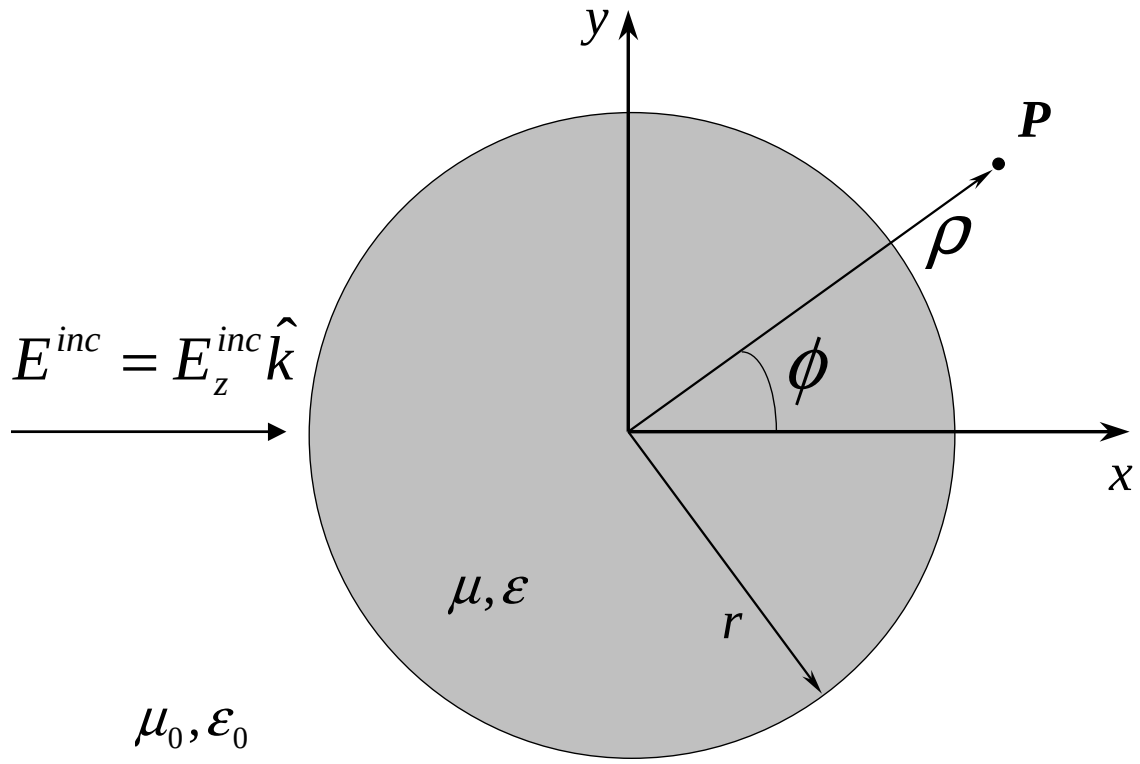

Figure 6.3: Incident plane wave on a dielectric circle with radius r.

where $H_n^{(2)}(k_0\rho)$ is the Hankel function of order n of the second kind which can be expressed in terms of the Bessel function of the first kind of order n (J_n) and the Bessel function of the second kind of order n (Y_n) shown in Equation (6.27):

$$H_n^{(2)}(k_0\rho) = J_n(k_0\rho) - \jmath Y_n(k_0\rho) \tag{6.27}$$

The term A_n is given by:

$$A_n = \frac{\frac{\eta_0}{\eta_d} J_n(k_0 r) J'(k_d r) - J'(k_0 r) J_n(k_d r)}{J_n(k_d r) H_n^{(2)'}(k_0 r) - \frac{\eta_0}{\eta_d} J_n'(k_d r) H_n^{(2)}(k_0 r)} \tag{6.28}$$

where k_d is the wavenumber associated with the interior of the scattering object, η_0 is the wave impedance in free space and η_d is the wave impedance of the dielectric cylinder. The E^{tot} field interior to the scatterer can be expressed as:

$$E^{tot} = \sum_{n=-\infty}^{\infty} \jmath^{-n} B_n J_n(k_d\rho) e^{\jmath n\phi} \tag{6.29}$$

where

$$B_n = \frac{\frac{-2\jmath}{\pi k_0 r}}{J_n(k_d r)H_n^{(2)'}(k_0 r) - \frac{\eta_0}{\eta_d}J_n'(k_d r)H_n^{(2)}(k_0 r)} \tag{6.30}$$

In order to compare the Mie series and our implementation of the MoM, a 2D cylinder with radius $r = 2m$ is considered. The frequency is 300 MHz. The MoM implementation uses 10 discretisations per wavelength, leading to 280 basis functions. The Mie series approach uses 30 terms, whereby the infinite series is truncated at $n = -15$ and $n = +15$. The relative dielectric permittivity of the cylinder is $\varepsilon_r = 5$. The surface currents are computed using both techniques and Figure (6.4) shows that very good agreement is achieved between both the real and the imaginary parts of the surface magnetic current. Good agreement is also achieved for the surface electric current shown in Figure (6.5).

Since the results obtained using the Integral Equation formulation match very well the Mie series formulation, it can be concluded that the MoM implementation is correct. Therefore the Buffered Block Forward Backward Method can be applied to the matrix equation in order to compute the surface currents. The comparison between the MoM formulation and the Mie series was performed for many cases, for various relative permittivity values and for various values of the cylinder radius. For brevity only one example is presented in this section. Nevertheless it should be noted that very good agreement between the two formulations has been achieved for all the case studies.

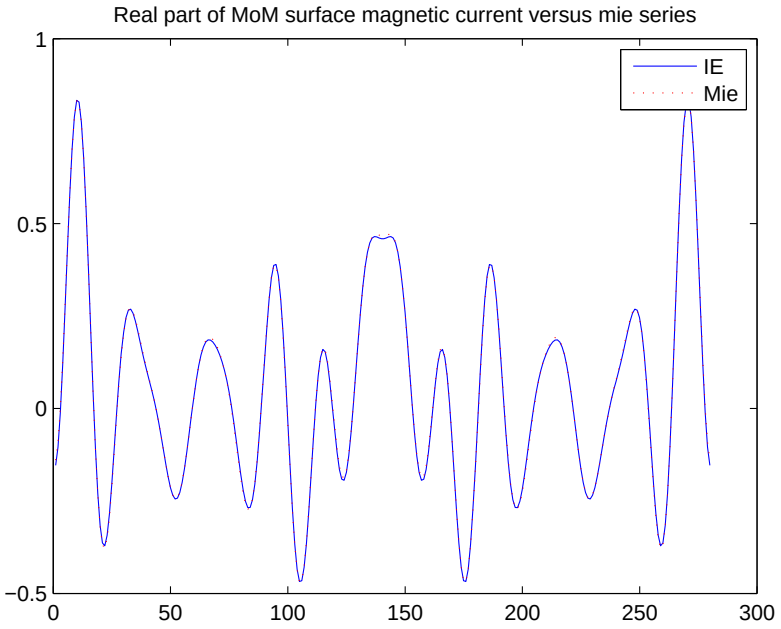

(a) Real component of the Magnetic Current computed using the IE and the Mie series formulations

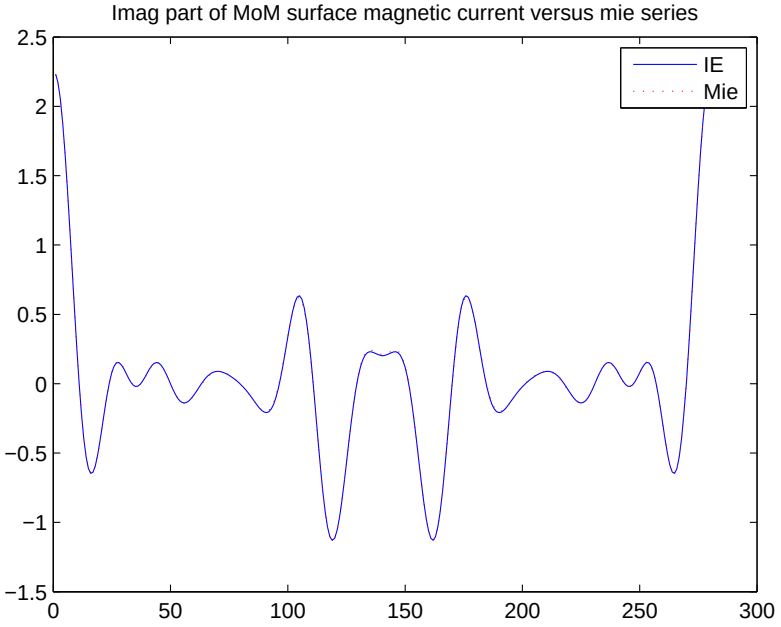

(b) Imaginary component of the Magnetic Current computed using the IE and Mie series formulations

Figure 6.4: Surface Magnetic Current computed for a homogeneous dielectric cylinder with radius $r = 2m$ using the IE and the Mie formulations.

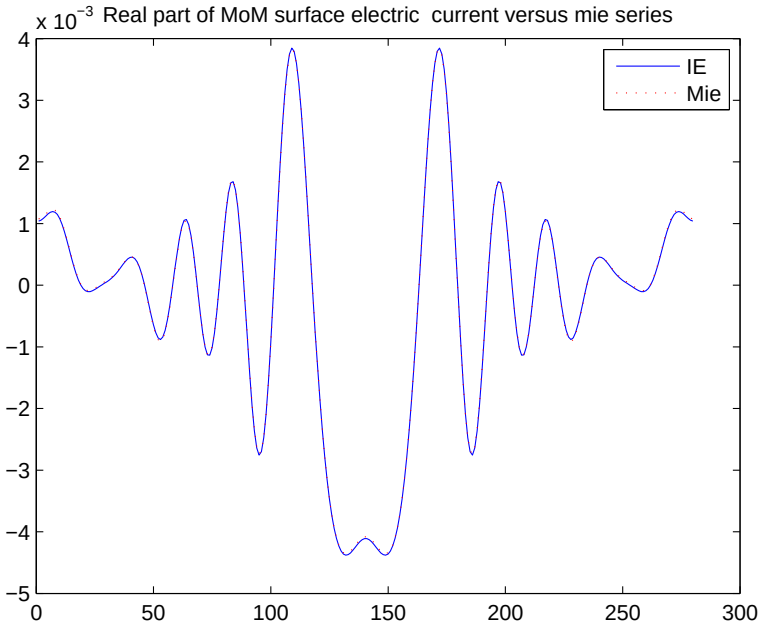

(a) Real component of the Electric Current computed using the IE and the Mie series formulations

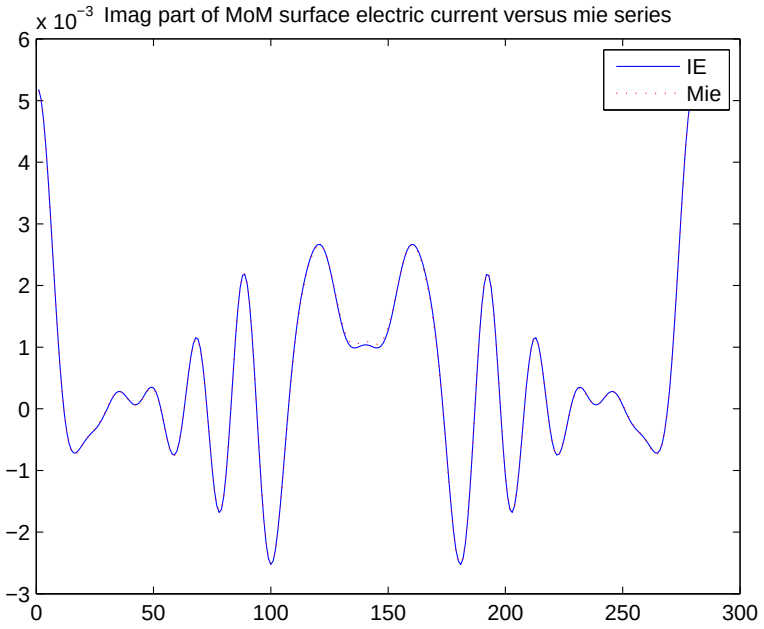

(b) Imaginary component of the Electric Current computed using the IE and Mie series formulations

Figure 6.5: Surface Electric Current computed for a homogeneous dielectric cylinder with radius $r = 2m$ using the IE and the Mie formulations.

6.2.2 Results

Open homogeneous dielectric scatterers

Recent work suggests that stationary methods are very effective when applied to surface scattering problems. Hence the first example involves the computation of scattering from an infinite surface separating a homogeneous dielectric from free-space. The surface is illuminated by fields from a line-source radiating at $300MHz$ as depicted in Figure (6.6).

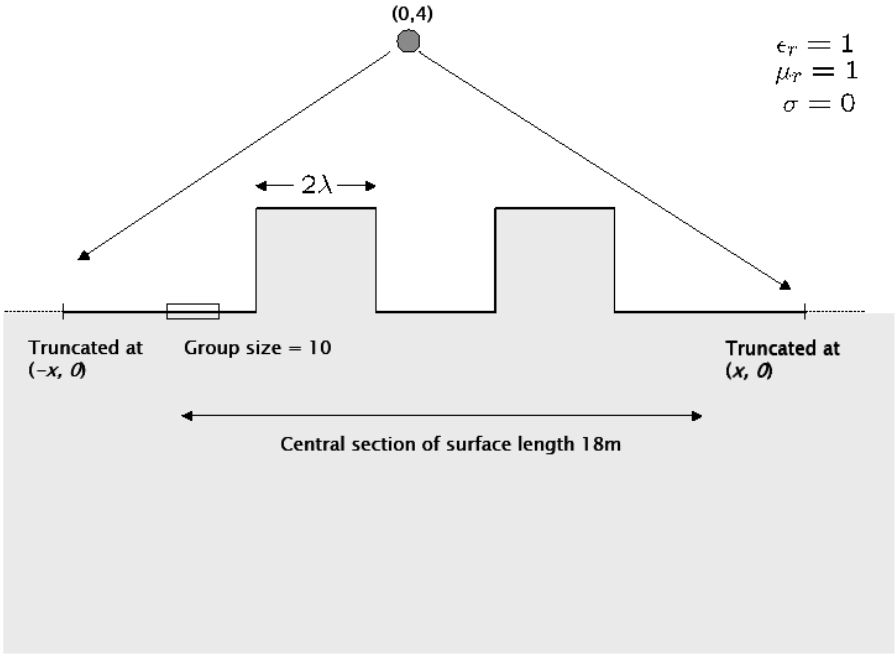

Figure 6.6: Dielectric Homogeneous Surface Closed at Infinity.

A number of corrugations are included on the surface in order to generate multiple scattering effects. It is obvious that the currents cannot be numerically calculated for an infinite surface. Therefore the scatterer has to be truncated. A few tests were performed in order to determine how far the truncation should be carried without affecting the accuracy of the field in the central region. It was concluded that truncating the surface at $(-6, 0)$ and $(6, 0)$ gives results that are practically identical to those which would be obtained for an infinite surface. The source is located at point $(0, 4)$, each side of the corrugation

Table 6.1: BFB applied to a non-lossy truncated surface with side length $2m$, total length $18m$

Permittivity	Order of $\mathbf{Z}$	$\psi^{(10)}$	$\psi^{(20)}$	$\psi^{(50)}$	$\psi^{(100)}$	Time (s)
$\varepsilon_r = 5$	810	-2	-2.9	-5.6	-10	130.21
$\varepsilon_r = 6$	882	-1.7	-2.26	-4	-6.77	151.6
$\varepsilon_r = 7$	954	-2.8	-4.3	-8.7	-14.7	197.24
$\varepsilon_r = 8$	1026	-2.45	-3.93	-8.36	-14.67	211.19
$\varepsilon_r = 9$	1080	-1.7	-2.32	-4.12	-7.7	238.64
$\varepsilon_r = 10$	1152	-2.78	-4.58	-9.98	-14.66	257.07
$\varepsilon_r = 20$	1620	-1.55	-1.88	-2.93	-4.68	310.44
$\varepsilon_r = 50$	2556	-1.66	-2.07	-3.36	-5.51	717

is of length $2m$ and the overall length of the surface is $18m$. Firstly the Block Forward Backward (BFB) was applied to a series of problems where the scatterer was considered to be a non lossy homogeneous dielectric with $\varepsilon = 5, \ldots, 50$. For the purpose of applying the BFB method the unknowns were grouped together into groups of 10. No buffer zones were used. These results are presented in Table 6.1, where column 1 represents the relative premittivity ε_r values and the order of the $\mathbf{Z}$ matrix is given in column 2. Columns $3-6$ depict the normalised error $\psi = \log_{10} \frac{||\mathbf{V}-\mathbf{Z}\mathbf{J}_{BFB}||}{||\mathbf{V}||}$. $\psi^{(k)}$ is the normalised error after iteration (k) and is computed in terms of $\mathbf{J}_{BFB}^{(k)}$, which represents the surface fields computed using k iterations of the BFB technique. Column 7 depicts the time required to complete 100 BFB iterations. It can be noted that the BFB achieves low error values after 50 iterations for most of the tested surfaces. It appears to slow down for the relative permittivities $\varepsilon_r = 6, 9, 20, 50$. However good accuracy is still achieved in these cases. Another important characteristic of the BFB method is the time it takes to complete its sweeps. It can be seen that the BFB takes an average of $1.3s$ to $7.2s$ per iteration depending on the order of the $\mathbf{Z}$ matrix.

Next the BFB was applied to a truncated homogeneous surface with the same side length of $2m$. However the relative permittivity of the homogeneous surface is now set to be a complex one with the values $\varepsilon = 5 - 0.1j, \ldots, 50 - 0.1j$. The source remains in the same position at $(0, 4)$ and the unknowns are grouped together in groups of 10. A summary of the results is given in Table 6.2. When comparing these results with Table 6.1, it can be

Table 6.2: BFB applied to a lossy truncated surface with side length $2m$, total length $18m$

Permittivity	Order of $\mathbf{Z}$	$\psi^{(10)}$	$\psi^{(20)}$	$\psi^{(50)}$	$\psi^{(100)}$	Time (s)
$\varepsilon_r = 5 - 0.1j$	810	-2.6	-4.1	-8.57	-14.75	131.7
$\varepsilon_r = 6 - 0.1j$	882	-2.43	-3.71	-7.98	-14.68	153.1
$\varepsilon_r = 7 - 0.1j$	954	-3.83	-6.71	-14.7	-14.7	198.3
$\varepsilon_r = 8 - 0.1j$	1026	-2.53	-4.1	-8.81	-14.69	215.15
$\varepsilon_r = 9 - 0.1j$	1080	-2.15	-3.16	-6.19	-11.25	241
$\varepsilon_r = 10 - 0.1j$	1152	-3.19	-5.61	-12.87	-14.67	263
$\varepsilon_r = 20 - 0.1j$	1620	-1.76	-2.3	-4.04	-6.9	317.1
$\varepsilon_r = 50 - 0.1j$	2556	-1.78	-2.3	-3.9	-6.58	719.3

noted that the BFB achieves lower errors compared to the non lossy examples presented in Table 6.1. This is due to the fact that the lossy dielectrics will dampen some of the multiple interactions within the scatterer. For example the BFB reaches an error of -14.68 when applied to a homogeneous surface with the relative permittivity of $\varepsilon_r = 6 - 0.1j$, whereas for the real value relative permittivity of $\varepsilon_r = 6$ the BFB reached and error of only -6.77 after 100 iterations. Time wise, the BFB performs in a similar manner to the nonlossy homogeneous wave scattering problems.

Next the BFB is applied to the truncated surface, whereby the relative permittivity is fixed at $\varepsilon_r = 7 - 0.1j$ and the side-length of each corrugation is modified between $1m, \ldots, 10m$, where the total length of the surface is between $9m$ and $90m$. By increasing the side length of the truncated surface, the number of multiple interactions within the structure is increased. The results for these truncated surfaces are given in Table 6.3. It can be noted that very low errors are achieved for the smaller scatterers, where the side length is $1m$ and $2m$. The BFB slows down as the side length increases, reaching a values of -4.65 after 100 iterations when applied to a problem of wave scattering from a truncated surface with the side length of $10m$. However, as it can be seen in Figure 6.3 this is more than satisfactory as the surface currents computed using the BFB after only 20 iterations achieve good agreement with the currents obtained by direct matrix inversion. Both the electric current in Figure (6.7(a)) and the magnetic current in Figure (6.7(b)) display excellent agreement, although the normalised error $\psi^{(20)}$ is -2.34.

Table 6.3: BFB applied to a truncated surface, relative permittivity $\varepsilon_r = 7 - 0.01j$

Side Length	Order of $\mathbf{Z}$	$\psi^{(10)}$	$\psi^{(20)}$	$\psi^{(50)}$	$\psi^{(100)}$	Time (s)
side length $= 1m$	570	-3.92	-7.39	-14.78	-14.8	95.1
side length $= 2m$	1142	-2.96	-4.61	-9.48	-14.67	237.2
side length $= 3m$	1714	-2.44	-3.01	-4.09	-6.18	352
side length $= 4m$	1908	-2.64	-3.21	-4.82	-7.52	471
side length $= 6m$	2862	-2.19	-2.58	-3.63	-5.31	811
side length $= 10m$	4770	-1.95	-2.34	-3.23	-4.65	2112

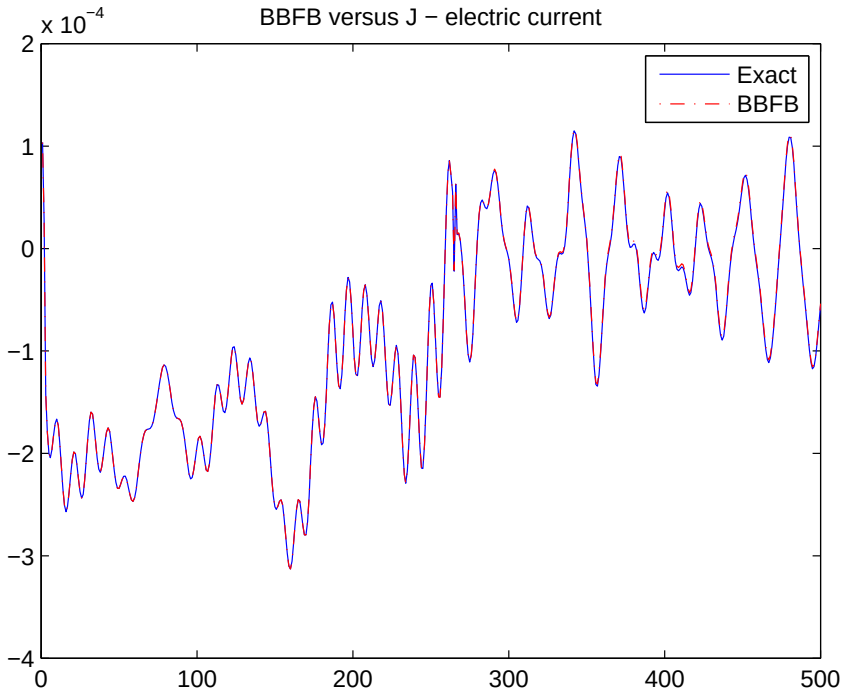

(a) Electric Current

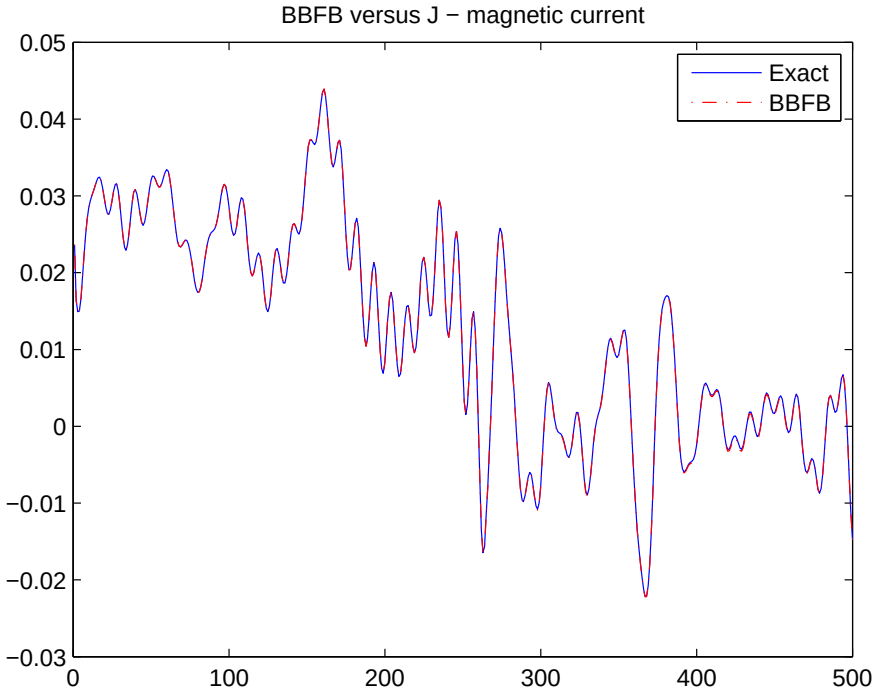

(b) Magnetic Current

Figure 6.7: Results for Electric Current and Magnetic Current for a truncated dielectric surface with relative permittivity $\varepsilon_r = 7 - 0.1j$ and side length= $10m$ obtained using the BFB method after 20 iterations. The index on the x-axis refers to the index number of the basis functions used.

Closed homogeneous dielectric scatterers

Having verified that the BFB is effective when applied to surface scattering problems, BBFB is applied to closed homogeneous dielectric scatterers as schematically described in Figure (6.8). In this section the BBFB is applied to a series of problems involving homogeneous 2D cylinders of varying sizes and constructive parameters illuminated by a plane wave.

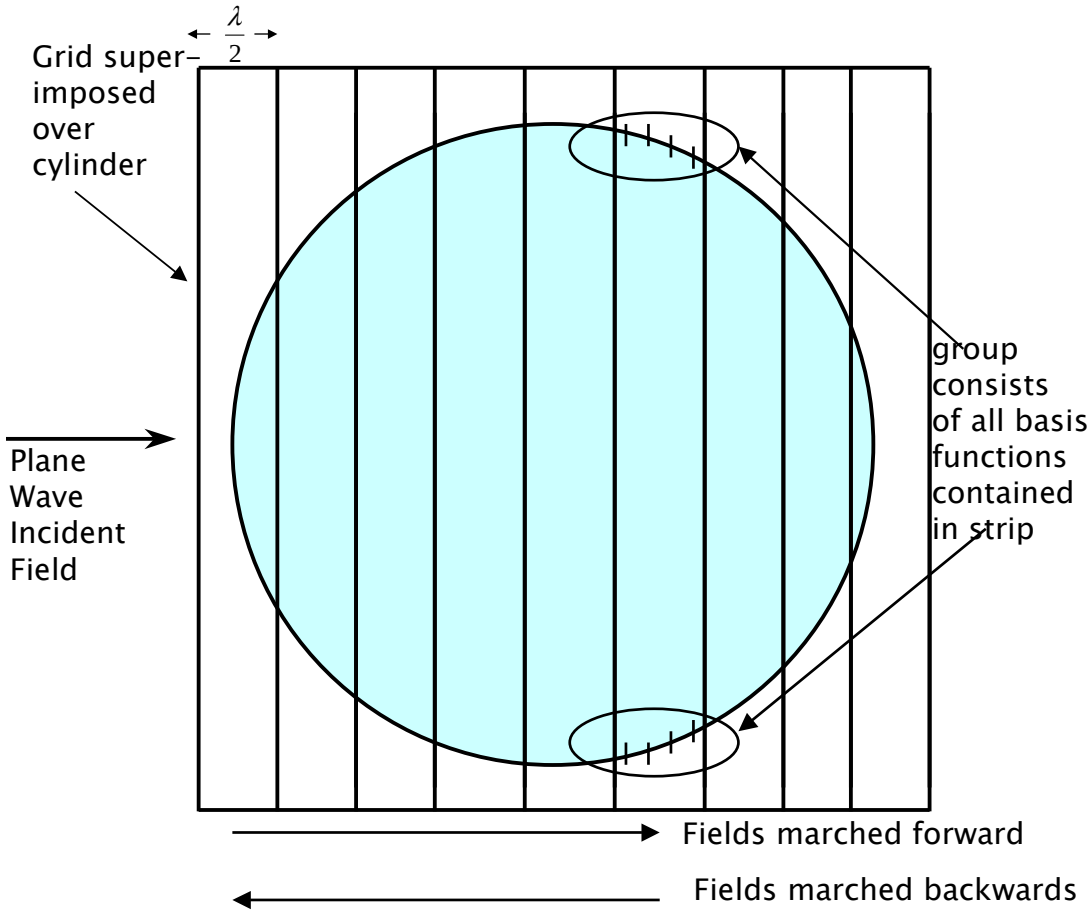

Figure 6.8: Closed Homogeneous Dielectric Body Illuminated by a plane wave.

Firstly 2D cylinders with the relative permittivity of $\varepsilon_r = 10$ and relative permeability $\mu_r = 1$ are considered. The radii of the cylinders are varied between $2m$ and $10m$. The cylinders are discretised at a rate of 10 unknowns per wavelength, whereas the BBFB groups were identified by imposing a rectangular grid over the cylinder as depicted in Figure (6.8). Each strip in the rectangular grid is set to $\frac{\lambda_0}{2} = 0.5m$ in width and each group consists of all the basis functions in that particular strip. The BBFB was then applied and the fields were marched forwards and backwards through the structure, whereby one main region includes between 1 and 3 strips and the buffer is composed of 1 to 3 strips neighbouring the main region.

The performance of the BBFB for these non lossy problems is depicted in Table 6.4. The first column of Table 6.4 depicts the radius of the scatterer and the second column represents the order of the $\mathbf{Z}$ matrix associated with it. Column number 3 represents the total number of strips of the grid superimposed over the 2D cylinder and configuration of the groups and buffers is given in column 4 (e.g 1/2 means that the main region contains one strip of the grid and the buffer contains the 2 adjacent strips). Columns $5-8$ depict the error $\psi^{(k)}$ after 5, 10, 20 and 50 iterations. The time required for the BBFB to complete 50 forward-backward iterations is given in column 9. The average per BBFB iteration varies between $3s$ and $30s$, depending on the order of $\mathbf{Z}$ and the grouping configuration chosen. It can be noted that the BBFB applied to the non lossy 2D cylinders reaches normalised errors of around -2.5 after 10 iterations, the lowest errors being achieved for the larger cylinders. The error improves slightly when one increases the size of the main groups and the buffer groups. However it tends to slowly diverge after 50 iterations.

Table 6.4: BBFB applied to a 2D cylinder with relative permittivity $\varepsilon_r = 10$

Radius	Order of **Z**	No. of strips	Gr./Buf. regions	$\psi^{(5)}$	$\psi^{(10)}$	$\psi^{(20)}$	$\psi^{(50)}$	Time (s)
r $= 2m$	794	8	1/1	-1.367	-1.523	-1.533	-1.4	98.1
r $= 2m$	794	8	1/2	-1.397	-1.55	-1.59	-1.5	101.2
r $= 2m$	794	8	2/1	-1.365	-1.42	-1.4	-1.3	110.1
r $= 2m$	794	8	2/2	-1.45	-1.49	-1.4	-1.39	127.3
r $= 2m$	794	8	3/1	-1.5	-2.1	-2.4	-1.9	155.1
r $= 2m$	794	8	3/2	-2.1	-2.4	-2	-1.95	179.2
r $= 2m$	794	8	3/3	-2.5	-2.6	-2.4	-2.1	180.3
r $= 4m$	1588	16	1/1	-1.47	-1.51	-1.4	-1.38	189.3
r $= 4m$	1588	16	1/2	-1.49	-1.52	-1.5	-1.37	210.1
r $= 4m$	1588	16	2/1	-1.46	-1.47	-1.4	-1.37	235.3
r $= 4m$	1588	16	2/2	-1.48	-1.52	-1.41	-1.39	269.1
r $= 4m$	1588	16	3/1	-1.9	-1.95	-1.8	-1.7	297.6
r $= 4m$	1588	16	3/2	-2	-2.1	-2.2	-2	305.5
r $= 4m$	1588	16	3/3	-2.1	-2.3	-2	-1.9	325.1
r $= 6m$	2384	24	1/1	-1.6	-1.71	-1.7	-1.5	371
r $= 6m$	2384	24	1/2	-1.61	-1.73	-1.65	-1.6	396.2
r $= 6m$	2384	24	2/1	-1.57	-1.65	-1.6	-1.55	401.3
r $= 6m$	2384	24	2/2	-1.62	-1.65	-1.59	-1.5	423.1
r $= 6m$	2384	24	3/1	-2.2	-2.4	-2.1	-1.9	491
r $= 6m$	2384	24	3/2	-2.1	-2.6	-2.3	-2	516
r $= 6m$	2384	24	3/3	-2.2	-2.71	-2.15	-2.1	558.3
r $= 10m$	3972	40	1/1	-1.65	-1.72	-1.7	-1.45	1012.3
r $= 10m$	3972	40	1/2	-1.68	-1.78	-1.77	-1.65	1158.1
r $= 10m$	3972	40	2/1	-1.675	-1.76	-1.75	-1.5	1298.8
r $= 10m$	3972	40	2/2	-1.69	-1.78	-1.7	-1.6	1351
r $= 10m$	3972	40	3/1	-2.19	-2.25	-2.21	-1.85	1301.8
r $= 10m$	3972	40	3/2	-2.21	-2.26	-2.16	-1.9	1356.3
r $= 10m$	3972	40	3/3	-2.23	-2.27	-2.19	-2.01	1496.6

A similar behaviour of the BBFB is observed when applied to lossy 2D cylinders, where the relative permittivity has the value $\varepsilon_r = 10 - 0.1j$. These results are depicted in Table 6.5. In a similar manner as for the non lossy scatterers, the radius is varied between $2m$ and $10m$. The BBFB method achieves slightly smaller errors compared to the non lossy scattering problems, due to the damping of the multiple diffractions with the scatterer. The error is smaller for larger group and buffer regions. It also achieves lower values for larger cylinders.

Next the BBFB is employed in order to solve problems of wave scattering from 2D cylinders of radius $4m$ and a varying relative permittivity $\varepsilon_r = 5 - 0.1j, \ldots, 50 - 0.1j$. These results are depicted in Table 6.6. It can be noted that the performance of the BBFB improves with higher relative permittivity.

In order to assess how the algorithm performed as the problem size grew, the BBFB method was also applied to very large 2D homogeneous dielectric objects. Consider a 2D cylinder with the radius of $40m$, the dielectric permittivity $\varepsilon_r = 5 - 0.1j$, where each primary subregion contains 2 strips with the buffer of the same size. The number of discretisations is 5027 leading to a $\mathbf{Z}$ matrix of size 10054×10054 which could not be stored on the machine available. The $\mathbf{Z}$ subblocks were created instead and used to perform the BBFB iterations. Figure (6.9) depicts $\psi^{(k)}$ when applied to such a large cylinder, where it can be noted that the error again stagnates around the $10^{-2.7}$ value.

As it can be seen in Tables 6.4 - 6.6, the normalised error obtained after applying the BBFB to 2D lossy and non lossy cylinders does not reach machine precision. However the surface currents obtained using the BBFB method are quite acceptable when compared to direct matrix inversion. For example in Table 6.6 it can be noted that for a 2D cylinder with a radius of $4m$ and dielectric permittivity $\varepsilon_r = 10 - 0.1j$ the normalised error $\psi^{(k)}$ reaches values around -2 when applying the BBFB using one main region and 2 neighboring regions as buffers. Figures (6.10) and (6.11) depict the real and imaginary parts of the surface electric and magnetic currents obtained using the Mie series, direct matrix inversion and BBFB after 5 iterations. Excellent agreement between the currents is achieved. Therefore it can be concluded that a normalised error of -2 represents an acceptably accurate result. In certain instances this level of accuracy would be not sufficient, for example when very

small Radar Cross Sections are to be found. However this accuracy is sufficient for the problems discussed in this work.

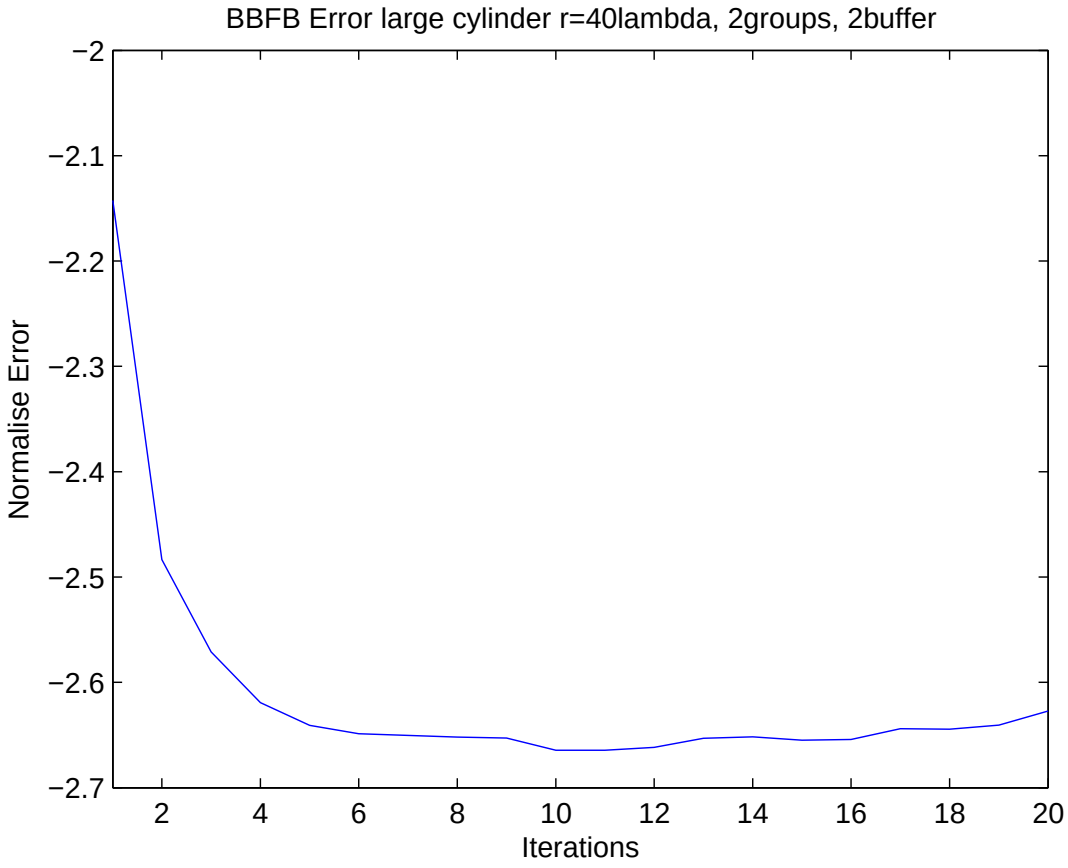

Figure 6.9: BBFB applied to large 2D closed homogeneous scatterer.

Table 6.5: BBFB applied to a 2D cylinder with relative permittivity $\varepsilon_r = 10 - 0.1j$

Radius	Order of **Z**	No. of strips	Gr./Buf. regions	$\psi^{(5)}$	$\psi^{(10)}$	$\psi^{(20)}$	$\psi^{(50)}$	Time (s)
r $= 2m$	794	8	1/1	-1.7	-1.8	-1.61	-1.5	101.3
r $= 2m$	794	8	1/2	-1.8	-1.9	-1.89	-1.79	107.1
r $= 2m$	794	8	2/1	-1.91	-1.96	-1.86	-1.6	117
r $= 2m$	794	8	2/2	-1.93	-1.96	-1.8	-1.7	127.1
r $= 2m$	794	8	3/1	-1.95	-1.99	-1.8	-1.71	136.3
r $= 2m$	794	8	3/2	-2.3	-2.6	-2.3	-1.9	158.4
r $= 2m$	794	8	3/3	-2.41	-2.68	-2.39	-2.1	179.3
r $= 4m$	1588	16	1/1	-1.85	-1.9	-1.7	-1.45	185.1
r $= 4m$	1588	16	1/2	-1.96	-1.99	-1.86	-1.75	199.3
r $= 4m$	1588	16	2/1	-1.95	-1.97	-1.88	-1.78	212.1
r $= 4m$	1588	16	2/2	-1.975	-1.99	-1.8	-1.7	251.3
r $= 4m$	1588	16	3/1	-2	-2.19	-1.95	-1.6	275.5
r $= 4m$	1588	16	3/2	-2.15	-2.24	-1.9	-1.65	291.1
r $= 4m$	1588	16	3/3	-2.21	-2.3	-2.1	-1.8	315.5
r $= 6m$	2384	24	1/1	-1.95	-1.96	-1.91	-1.71	369.4
r $= 6m$	2384	24	1/2	-1.96	-1.99	-1.89	-1.68	381.3
r $= 6m$	2384	24	2/1	-1.93	-1.95	-1.88	-1.78	396.5
r $= 6m$	2384	24	2/2	-1.99	-2	-1.9	-1.8	4011.5
r $= 6m$	2384	24	3/1	-2.15	-2.26	-2.1	-1.85	431.5
r $= 6m$	2384	24	3/2	-2.195	-2.3	-2.25	-1.96	471.6
r $= 6m$	2384	24	3/3	-2.21	-2.34	-2.15	-2	526.3
r $= 10m$	3972	40	1/1	-2.1	-2.15	-2.06	-1.85	1027
r $= 10m$	3972	40	1/2	-2.15	-2.19	-2.155	-2.04	1131
r $= 10m$	3972	40	2/1	-2.114	-2.21	-2.09	-2.01	1226
r $= 10m$	3972	40	2/2	-2.2	-2.22	-2	-1.9	1295.4
r $= 10m$	3972	40	3/1	-2.3	-2.5	-2.2	-1.9	1382
r $= 10m$	3972	40	3/2	-2.5	-2.9	-2.8	-2.6	1473
r $= 10m$	3972	40	3/3	-2.7	-2.9	-2.85	-2.65	1531

Table 6.6: BBFB applied to a 2D cylinder of radius $4m$

ε_r	Order of $\mathbf{Z}$	No. of strips	Gr./Buf. regions	$\psi^{(5)}$	$\psi^{(10)}$	$\psi^{(20)}$	$\psi^{(50)}$	Time (s)
$5-0.1j$	1124	8	1/1	-1.87	-1.91	-1.67	-1.5	201.1
$5-0.1j$	1124	8	1/2	-1.91	-1.97	-1.85	-1.7	225.6
$5-0.1j$	1124	8	2/1	-1.89	-1.9	-1.76	-1.71	237.2
$5-0.1j$	1124	8	2/2	-1.93	-1.937	-1.75	-1.74	258.1
$5-0.1j$	1124	8	3/1	-1.91	$-.921$	-1.89	-1.73	271.4
$5-0.1j$	1124	8	3/2	-1.93	-1.95	-1.86	-1.8	293
$5-0.1j$	1124	8	3/3	-2.1	-2.3	$1-2.05$	-2	310.9
$8-0.1j$	1420	16	1/1	-1.88	-1.91	-1.73	-1.71	296.3
$8-0.1j$	1420	16	1/2	-1.95	-1.97	-1.89	-1.82	315.1
$8-0.1j$	1420	16	2/1	-1.89	-1.9	-1.85	-1.73	321.3
$8-0.1j$	1420	16	2/2	-1.96	-1.98	-1.85	-1.71	344.8
$8-0.1j$	1420	16	3/1	-1.9	-2.1	-1.87	-1.73	351
$8-0.1j$	1420	16	3/2	-2.1	-2.19	-1.96	-1.79	367.2
$8-0.1j$	1420	16	3/3	-2.25	-2.4	-2.3	-2.21	381.3
$10-0.1j$	1588	16	1/2	-1.96	-1.99	-1.86	-1.75	199.3
$10-0.1j$	1588	16	2/1	-1.95	-1.97	-1.88	-1.78	212.1
$10-0.1j$	1588	16	2/2	-1.975	-1.99	-1.8	-1.7	251.3
$10-0.1j$	1588	16	3/1	-2	-2.19	-1.95	-1.6	275.5
$10-0.1j$	1588	16	3/2	-2.15	-2.24	-1.9	-1.65	291.1
$10-0.1j$	1588	16	3/3	-2.21	-2.3	-2.1	-1.8	315.5
$20-0.1j$	2246	40	1/1	-1.96	-1.99	-1.8	-1.75	378.2
$20-0.1j$	2246	40	1/2	-1.99	-2	-1.95	-1.89	392.6
$20-0.1j$	2246	40	2/1	-1.97	-1.99	-1.89	-1.8	399.2
$20-0.1j$	2246	40	2/2	-1.99	-2.1	-1.96	-1.91	418.8
$20-0.1j$	2246	40	3/1	-1.99	-2.01	-1.9	-1.75	429.1
$20-0.1j$	2246	40	3/2	-2.15	-2.19	-1.98	-1.81	451.3
$20-0.1j$	2246	40	3/3	-2.36	-2.4	-2.1	-2	493.9
$50-0.1j$	3554	40	1/1	-1.98	-1.99	-1.8	-1.75	916.7
$50-0.1j$	3554	40	1/2	-2.05	-2.1	-1.95	-1.8	1082.8
$50-0.1j$	3554	40	2/1	-2.1	-2.18	-1.99	-1.9	1098.3
$50-0.1j$	3554	40	2/2	-2.3	-2.5	-2.25	-2.01	1164.9
$50-0.1j$	3554	40	3/1	-2.03	-2.16	-2.09	-1.98	1198.3
$50-0.1j$	3554	40	3/2	-2.15	-2.21	-2.13	-2	1278
$50-0.1j$	3554	40	3/3	-2.37	-2.41	-2.28	-2.11	1393.3

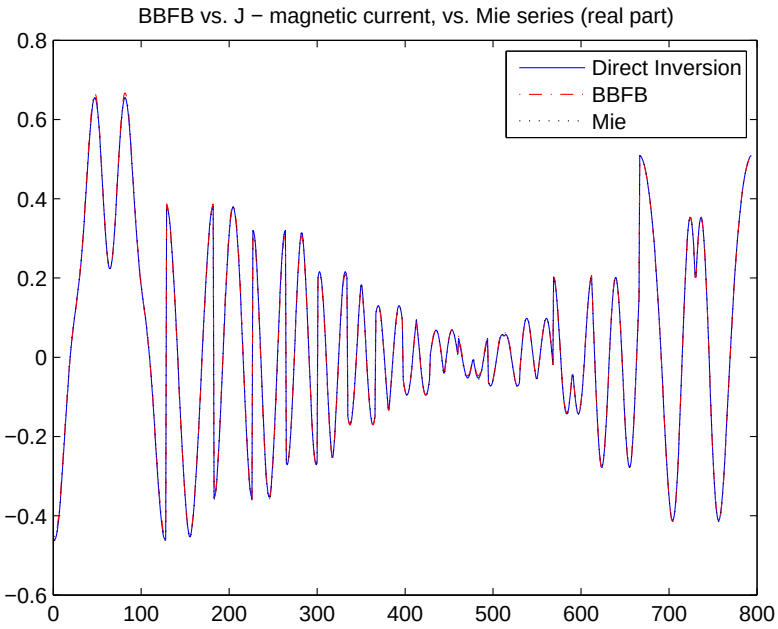

(a) Magnetic Current (real part)

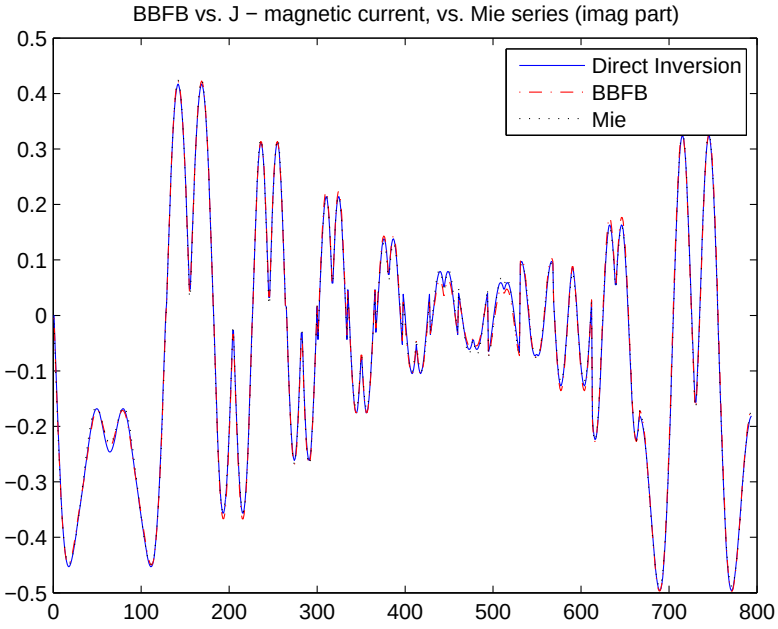

(b) Magnetic Current (imag part)

Figure 6.10: Results for Magnetic Current for a closed homogeneous dielectric cylinder with radius $4m$, $\varepsilon_r = 10 - 0.1j$ illuminated by a plane wave after 5 iterations. The main group contains 2 strips and the buffer contains 2 strips. The index on the x-axis refers to the index number of the basis functions used.

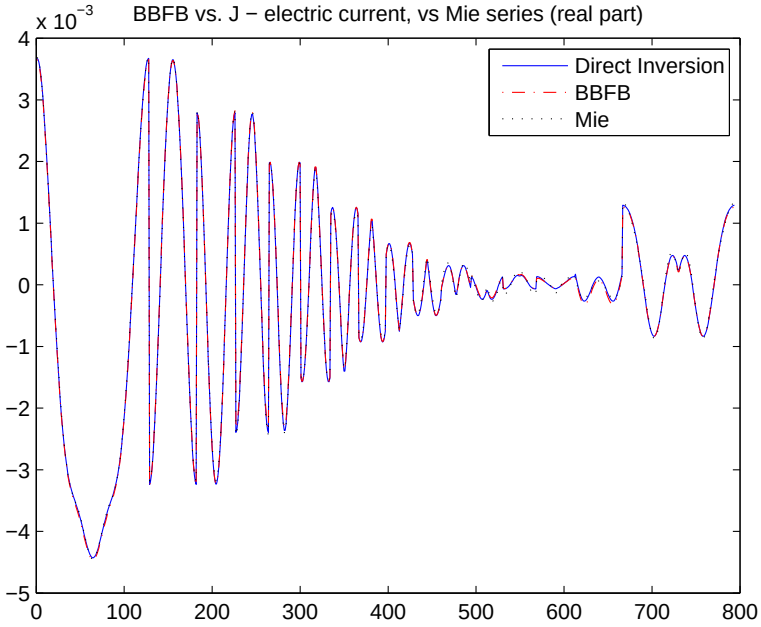

(a) Electric Current (real part)

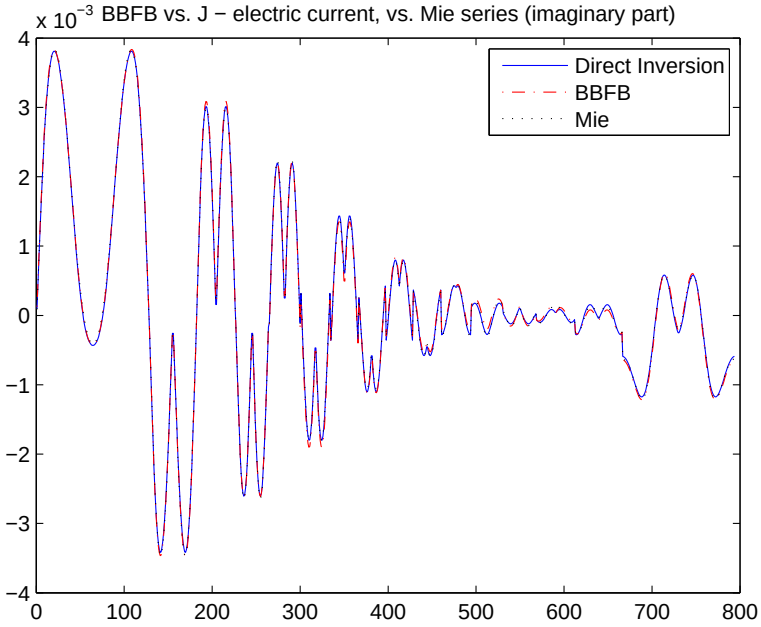

(b) Magnetic Current (imag part)

Figure 6.11: Results for Electric Current for a closed homogeneous dielectric cylinder with radius $4m$, $\varepsilon_r = 10 - 0.1j$ illuminated by a plane wave after 5 iterations. The main group contains 2 strips and the buffer contains 2 strips. The index on the x-axis refers to the index number of the basis functions used.

Buffered Block Forward Backward Method against other Iterative solvers

In order to gauge the usefulness of the BBFB and BFB, their performance was also compared against some of the Krylov subspace based iterative techniques.

Figure (6.12(a)) presents the convergence characteristics of the BFB method against the preconditioned GMRES and BiCGSTAB techniques when applied to a truncated surface. The surface considered has a corrugation length of $2m$ and total length $18m$, and relative permittivity $\varepsilon_r = 50 - 0.1j$. The unknowns are grouped into groups of 10, and no buffer is used. In order to provide a fair comparison a preconditioner was used for the Krylov methods. Noting that Block Forward Backward is just Forward Backward with a block Jacobi preconditioner, it was decided to use this preconditioner for the Krylov methods. The normalised error is plotted against the number of computations, expressed in terms of complex multiplications. It can be noted that although the BFB method converges, both the GMRES and the BiCGSTAB ultimately reach a better solution. The GMRES outperforms both the BFB and BiCGSTAB methods in terms of convergence, requiring similar computation time.

Figure (6.12(b)) depicts the convergence rates of the BBFB method for the first 150 iterations against the preconditioned GMRES, CGNE and BiCGSTAB techniques when applied to a 2D closed homogeneous scatterer with the radius of $r = 10m$ and dielectric permittivity $\varepsilon = 10 - 0.1j$, where each primary subregion contains 3 out of the total 40 strips and each buffer region contains 2 strips. The preconditioner used for the GMRES, BiCGSTAB and CGNE is a block diagonal preconditioner containing the inverses of the diagonal blocks of $\mathbf{Z}$ associated with each group. The Krylov solvers and the BBFB method require a similar computational time per iteration. It can be noted that the BBFB performs better than the preconditioned BiCGSTAB and the CGNE algorithms. However the GMRES algorithm clearly achieves machine precision, in contrast to the BBFB method which stagnates.

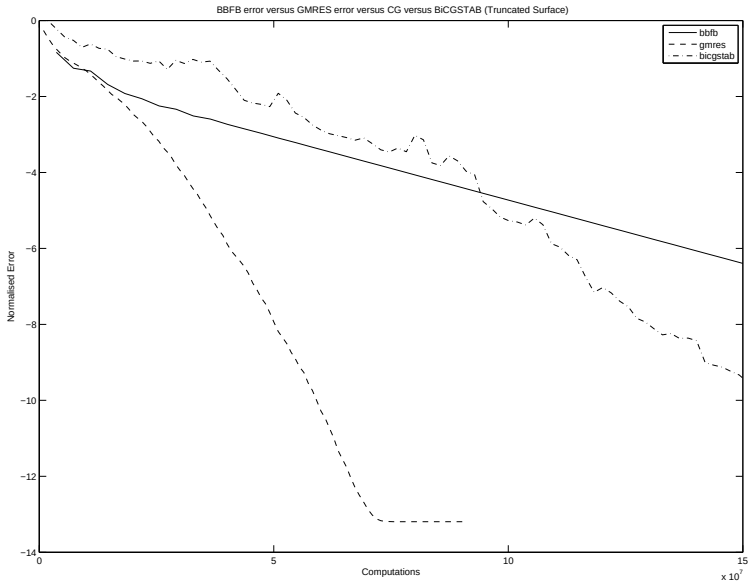

(a) Truncated Surface

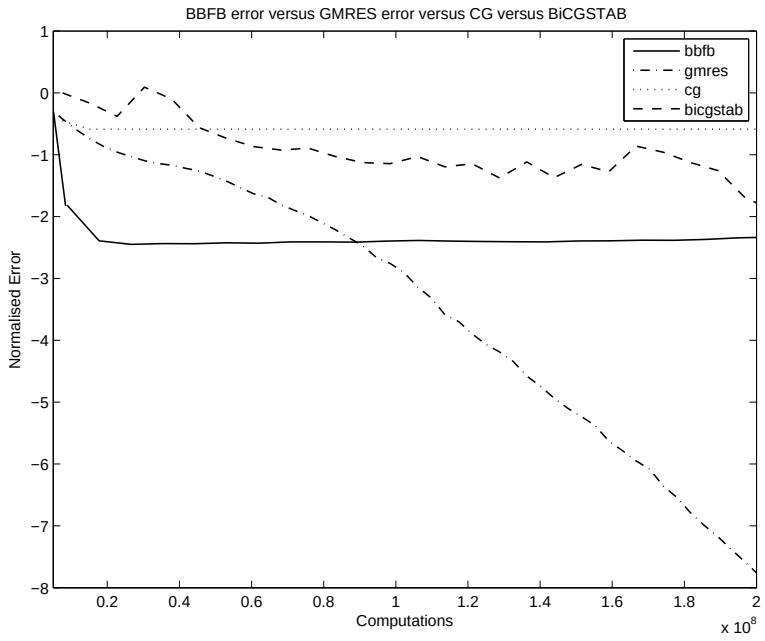

(b) Cylinder

Figure 6.12: BBFB against Krylov Solvers applied to 2D homogeneous scatterers

6.2.3 Conclusion

In this chapter the Block Forward Backward and Buffered Block Forward Backward methods applied to the matrix equation obtained after applying the MoM to the Coupled EFIE.

The Block Forward Backward Method was used in order to compute the fields scattered from open 2D homogeneous dielectric surfaces. The numerical results suggest that the BFB algorithm produces quickly convergent results when applied to scattering from the truncated surfaces. A comparison between the BFB and other Krylov solvers was performed, showing that the GMRES is not as effective as the BFB in terms of computation time.

The Buffered Block Forward Backward method was employed in order to solve problems of wave scattering from 2D closed homogeneous dielectrics. It was shown that the BBFB does not achieve machine precision. However the surface currents obtained using the BBFB match very closely the currents obtained by direct matrix inversion and Mie series even though the normalised error was only between -2 and -3. The BBFB was compared to preconditioned GMRES, CGNE and BiCGSTAB. It was shown that the BBFB reaches a lower error compared to the CGNE and BiCGSTAB. However it is ultimately outperformed by GMRES in terms of convergence.

Chapter 7

Design of 2D TeraHertz band-gap photonic waveguides using the Buffered Block Forward Backward Method

7.1 Introduction

In Chapter 6 the Buffered Block Forward Backward Method was applied to solving problems of electromagnetic wave scattering from 2D closed homogeneous dielectric bodies. In this chapter the same formulation is applied to a new research area, namely the development of 2D models of TeraHertz photonic band-gap waveguides. TeraHertz (THz) technologies are in the early stages of their development. In the electromagnetic spectrum THz waves or T-rays lie between the radio and the infrared frequencies. Therefore THz frequencies have potential in a wide range of application areas such as chemical recognition of substances, tomography, and biomedical imaging [89]. The latter application is particularly interesting as THz radiation does not damage biological tissue and therefore can be used to identify benign and malignant human tissue while being cheaper than MRI and,

unlike ultrasound, not requiring contact with the skin [90]. Another biomedical application of THz waves is early detection of dental cavities [91]. Security applications such as identifying illegal substances are also of great interest. For instance identification of drugs or explosives can be performed using spectroscopic fingerprints [89]. Quality control of medical substances is an additional application.

Further advances in these areas are contingent on the availability of reliable THz waveguiding structures. While much progress has been made in the production of T-rays that can propagate in free-space a major challenge remains in designing structures to guide and otherwise manipulate them. Free space propagation is currently the main transmission method of THz waves, which is not very feasible due to the attenuation caused by vapour absorption of the THz signal. The design of effective THz waveguides is still an important challenge. This chapter focuses on the 2D modelling of TeraHertz (THz) dielectric band-gap photonic waveguides using the Buffered Block Forward Backward (BBFB) method.

7.2 Photonic band-gap waveguides

The early ideas for Photonic Band Gap (PBG) structures were introduced in the mid 1980s by Yablonovitch [92] and John [93]. They suggested that periodic dielectric structures have the capability of controlling the radiation so that there are no electromagnetic modes available in the dielectric structure within certain parameter ranges or *band gaps*. In certain frequency ranges, these devices are able to confine the EM radiation within a hollow in the PBG lattice, therefore transmitting the electromagnetic wave across a path with minimal losses [94].

Various types of PBG structures have been designed and investigated over time. A periodic structure of dielectric spheres in a diamond configuration was found to possess a complete photonic band gap in [95] whereby certain frequencies become forbidden regardless of the direction of propagation of the incident wave. Another important breakthrough was made by Yablonovitch in [96; 97] in designing microwave face-centred-cubic photonic

crystals by drilling a slab of dielectric material in a criss-cross manner. Photonic band gap structures that combined both metals and dielectrics were also designed. Brown and McMahon have suggested the availability of large photonic band gaps in face-centred-cubic structures of unconnected metal spheres arranged in a dielectric support [98]. This idea was later investigated in [99] where Fan et al. proved the existence of very large band gaps in such structures depending on the size of the metal spheres. Another class of photonic band-gap structure is the layer by layer configuration introduced in [100]. This device consists of layers of parallel dielectric rods, where each stack of rods is rotated by an angle other than 90° with respect to the previous layer. The sequence repeats every fourth layer. This type of dielectric band gap structure was initially designed for the microwave regime. However it is also suitable for the infrared and optical region.

While much progress has been in designing microwave, infrared and optical photonic band gap waveguides, the design of TeraHertz waveguides remains a major challenge. This interest was motivated by the many possible applications of the TeraHertz wave, in particular in biomedical imaging and chemical recognition of substances. Since the T-rays lie between the microwave and the visible frequency ranges it was assumed that the PBG structures suitable for the microwave and optical modes or a combination of them would be suitable for manipulating the THz radiation.

Initially metallic photonic band-gap structures were favoured when designing waveguides for the TeraHertz frequency range. A honeycomb metallic photonic band gap structure is presented and investigated in [101] showing that it exhibits full band gaps in the TeraHertz range. A PBG constructed with Ni-coated silica cylinders arranged in a linear lattice in air background was presented in [102] and it was shown that large PBGs are available for this type of structure. A rectangular waveguide with metal photonic crystal sidewalls is described in [103] showing low losses and high efficiency. Jian *et al.* [104] investigated a metalo-dielectric waveguide designed by inserting a patterned dielectric slab between two parallel metal plates. The dielectric slab in this experiment was a Silicon one and consisted of an array of holes etched through it. The Silicon was chosen due to its low absorption properties. A similar design was investigated in [105], where the waveguiding structure consisted of a triangular array of holes in a GaAs dielectric background and it was shown

that this device structure is suitable for biochemical sensing applications.

Photonic Crystal Fiber is another type of structure suitable for guiding the THz wave. It is constructed using a dielectric rod as core and dielectric tubes as cladding. In [106] a teflon PCF is presented and shown to have low loss characteristics and therefore to be suitable for THz radiation of high intensity. A polyethylene PCF with a square lattice is introduced in [107] and is shown to be more efficient than a polyethylene triangular lattice PCF in terms of dispersion and confinement loss. More recently a hollow core photonic band gap fibre was designed in [108] using two different polymer materials - teflon and High-Density Polyethylene (HDPE), both shown to exhibit low loss an low dispersion properties over a wide range of frequencies. Both the core and the claddings were constructed using hollow hexagonal tubes with rounded corners. Both materials exhibited very good characteristics, the teflon offering a wider low-loss and low-dispersion band. Another advantage of the Photonic Band Gap fibre is its high flexibility.

A different type of photonic band gap structures is presented in [109], where instead of holes etched in a dielectric material, the PBG structure is designed using dielectric cylinders on a metal coated silicon wafer. A similar structure of silicon rods aligned in a square array surrounded by air is investigated in [110] showing that efficient splitters can be designed using this PBG structure. Very high permittivity microwave ceramics rods having quadratic cross sections have been used in designing waveguides in [111], whereby the rods are arranged in a square lattice. These structures were proven to be efficient for microwave radiation and, by scaling the rods, can be modified accordingly, in order to be suitable for THz radiation.

This chapter focuses on designing photonic band-gap TeraHertz waveguides consisting of cylindrical dielectric rods surrounded by air. A typical square lattice photonic band-gap device structure consists of periodically aligned dielectric rods as can be seen in Figure (7.5) [112]. Other typical structures are hexagonal and honeycomb lattices as can be seen in Figure (7.2). This structure can ensure a complete reflection of the incident wave for certain values of rod spacing, so that it can prevent the EM wave from propagating in any direction within the xy plane [112].

In order to achieve wave confinement within the photonic band-gap structure, the

periodicity of the dielectric lattice has to be broken. This is performed by removing one row of rods from the lattice so that it looks as shown in Figure 7.3 [112]. The incident wave will be propagated across the newly created empty channel within the structure and will be confined within this hollow by the edge rods. Therefore, the wave confinement degree increases with the number of edge rods. However, for practical devices the number of edge rods has to be limited. In the same manner the guiding of the incident wave is achieved in the hexagonal and honeycomb lattice structures. Other devices, such as splitters represented in Figure (7.4), can be designed by removing other portions of the lattice and channeling the wave within the hollow created [113].

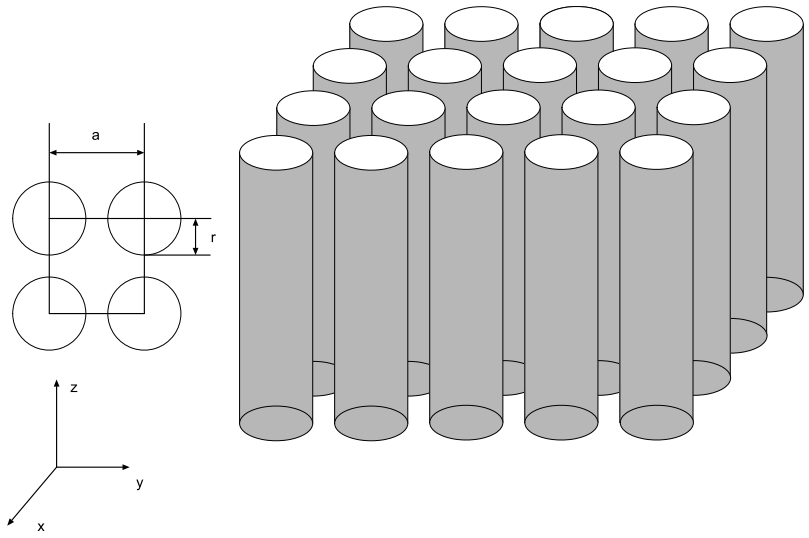

Figure 7.1: A band-gap photonic structure, where a is the *lattice constant* and r is the*radius* of each dielectric rod.

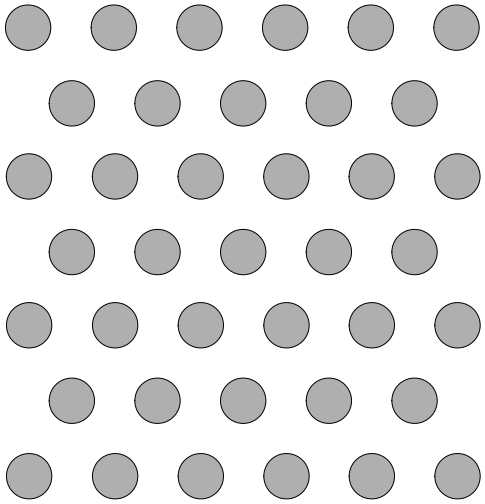

(a) Hexagonal Lattice

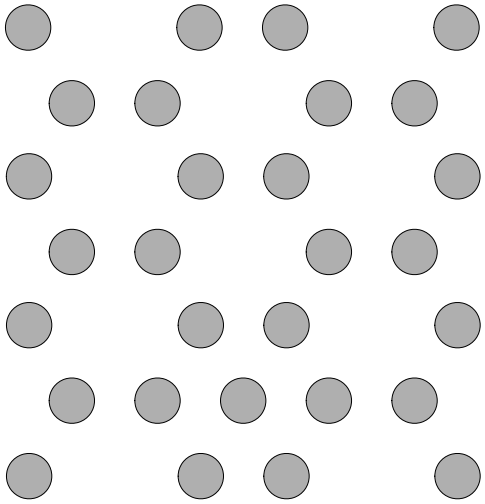

(b) Honeycomb Lattice

Figure 7.2: 2D schematic lattices.

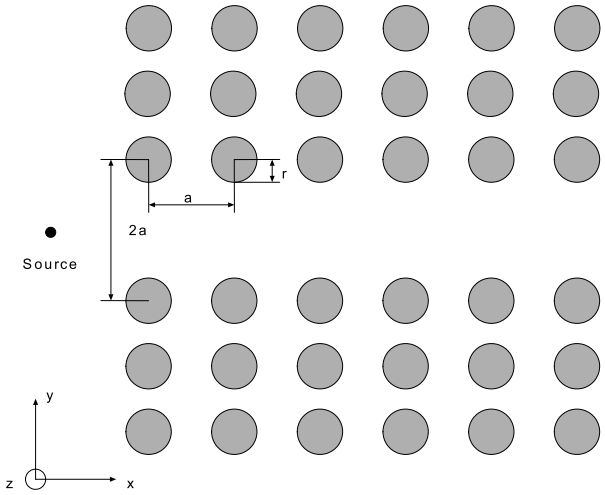

Figure 7.3: A squared lattice band-gap photonic waveguide, where a is the *lattice constant* and r is the *radius* of each dielectric rod.

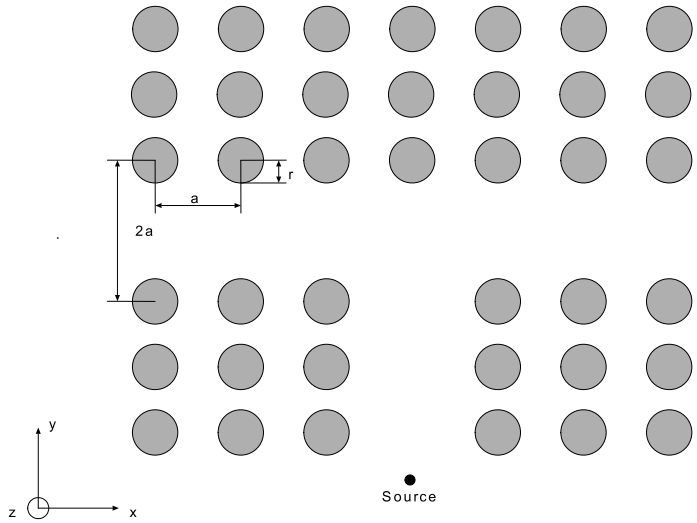

Figure 7.4: A squared lattice band-gap photonic splitter, where a is the *lattice constant* and r is the *radius* of each dielectric rod.

7.3 Integral Equation Formulation and the Buffered Block Forward Backward Method applied to designing Tera-Hertz Photonic Band Gap waveguides

In this chapter an accelerated Integral Equation (IE) technique is used for modeling a 2D THz band-gap photonic waveguide. The IE formulation only requires the discretisation of the scattering surface, thus generating a linear system of equations with fewer unknowns compared to other formulations, such as FEM. The structure is created by periodically aligning a series of dielectric (Si with $\varepsilon_r = 11.7$) rods. The problem of electromagnetic scattering within the waveguide is formulated in terms of the Coupled Electric Field Integral Equation [3].

$$E_z^{inc}(t) = K^t(t) + jk_0\eta_0 A_z^{(0)} + \{\frac{\partial F_y^{(0)}}{\partial x} - \frac{\partial F_x^{(0)}}{\partial y}\}_{S^+} \tag{7.1}$$

$$0 = -K^t(t) + jk_d\eta_d A_z^{d} + \{\frac{\partial F_y^{(d)}}{\partial x} - \frac{\partial F_x^{(d)}}{\partial y}\}_{S^-} \tag{7.2}$$

The Coupled EFIE expresses the fields interior (7.1) and exterior (7.2) in terms of vector potentials **A** and **F**. These potentials are described in terms of the tangential magnetic field (electric current **J**) and tangential electric field (magnetic current **K**). The Method of Moments (MoM) with N suitable basis and testing functions is applied to the Integral Equations. Subsequently the matrix equation of the following form is obtained:

$$\begin{bmatrix} \mathbf{A} & \mathbf{B} \\ \mathbf{C} & \mathbf{D} \end{bmatrix} \begin{bmatrix} \mathbf{j} \\ \mathbf{k} \end{bmatrix} = \begin{bmatrix} \mathbf{E} \\ \mathbf{0} \end{bmatrix} \tag{7.3}$$

where each of **A**, **B**, **C**,**D** is a matrix of size $N \times N$, and the unknown vector **J** of length $2N$ can be defined:

$$\mathbf{J} = \begin{bmatrix} \mathbf{j} \\ \mathbf{k} \end{bmatrix} \tag{7.4}$$

The focus of this chapter is the modelling of 2D THz dielectric band gap waveguides using the Buffered Block Forward Backward (BBFB) method [86; 87; 114]. As has been described in Chapters 5 and 6, the BBFB technique represents a variation of the Successive overrelaxation method and it is employed in solving the matrix equation obtained by applying the MoM to an Integral Equation formulation. The novelty of the BBFB technique is that the interactions between each subregion and the neighbouring subregions, referred to as buffer regions, are taken into account. A brief review of this technique is presented below.

Equation (7.3) can be rearranged so that the unknown electric and magnetic current components are interleaved:

$$\begin{bmatrix} \mathbf{Z}_{11} & \mathbf{Z}_{12} & \dots & \mathbf{Z}_{1N} \\ \mathbf{Z}_{21} & \mathbf{Z}_{22} & \dots & \mathbf{Z}_{2N} \\ \vdots & \vdots & \vdots & \vdots \\ \mathbf{Z}_{N1} & \mathbf{Z}_{N2} & \dots & \mathbf{Z}_{NN} \end{bmatrix} \begin{bmatrix} \mathbf{J}_1 \\ \mathbf{J}_2 \\ \vdots \\ \mathbf{J}_N \end{bmatrix} = \begin{bmatrix} \mathbf{V}_1 \\ \mathbf{V}_2 \\ \vdots \\ \mathbf{V}_N \end{bmatrix} \tag{7.5}$$

where Z_{mn} is a 2×2 matrix containing interactions between the unknowns j_m, k_m and j_n, k_n.

$$\mathbf{Z}_{mn} = \begin{bmatrix} A_{mn} & B_{mn} \\ C_{mn} & D_{mn} \end{bmatrix} \tag{7.6}$$

$$\mathbf{J}_n = \begin{bmatrix} j_n \\ k_n \end{bmatrix} \tag{7.7}$$

$$\mathbf{V}_n = \begin{bmatrix} E_n \\ 0 \end{bmatrix} \tag{7.8}$$

The basis functions are grouped together into M groupings where each contains $\frac{N}{M}$ basis

functions so that equation (7.3) can be now written in a block format:

$$\begin{bmatrix} \tilde{\mathbf{Z}}_{11} & \tilde{\mathbf{Z}}_{12} & \dots & \tilde{\mathbf{Z}}_{1M} \\ \tilde{\mathbf{Z}}_{21} & \tilde{\mathbf{Z}}_{22} & \dots & \tilde{\mathbf{Z}}_{2M} \\ \vdots & \vdots & \vdots & \vdots \\ \tilde{\mathbf{Z}}_{M1} & \tilde{\mathbf{Z}}_{M2} & \dots & \tilde{\mathbf{Z}}_{MM} \end{bmatrix} \begin{bmatrix} \tilde{\mathbf{J}}_1 \\ \tilde{\mathbf{J}}_2 \\ \vdots \\ \tilde{\mathbf{J}}_M \end{bmatrix} = \begin{bmatrix} \tilde{\mathbf{V}}_1 \\ \tilde{\mathbf{V}}_2 \\ \vdots \\ \tilde{\mathbf{V}}_M \end{bmatrix} \tag{7.9}$$

where $\tilde{\mathbf{Z}}_{mn}$ contains the interactions between all the basis functions in groups m and n. The Block Forward Backward (BFB) method finds a solution by solving a series of problems each one of which describes the surface currents in one particular subgroup. The currents are marched forward from group to group as can be seen in Figure 7.5.

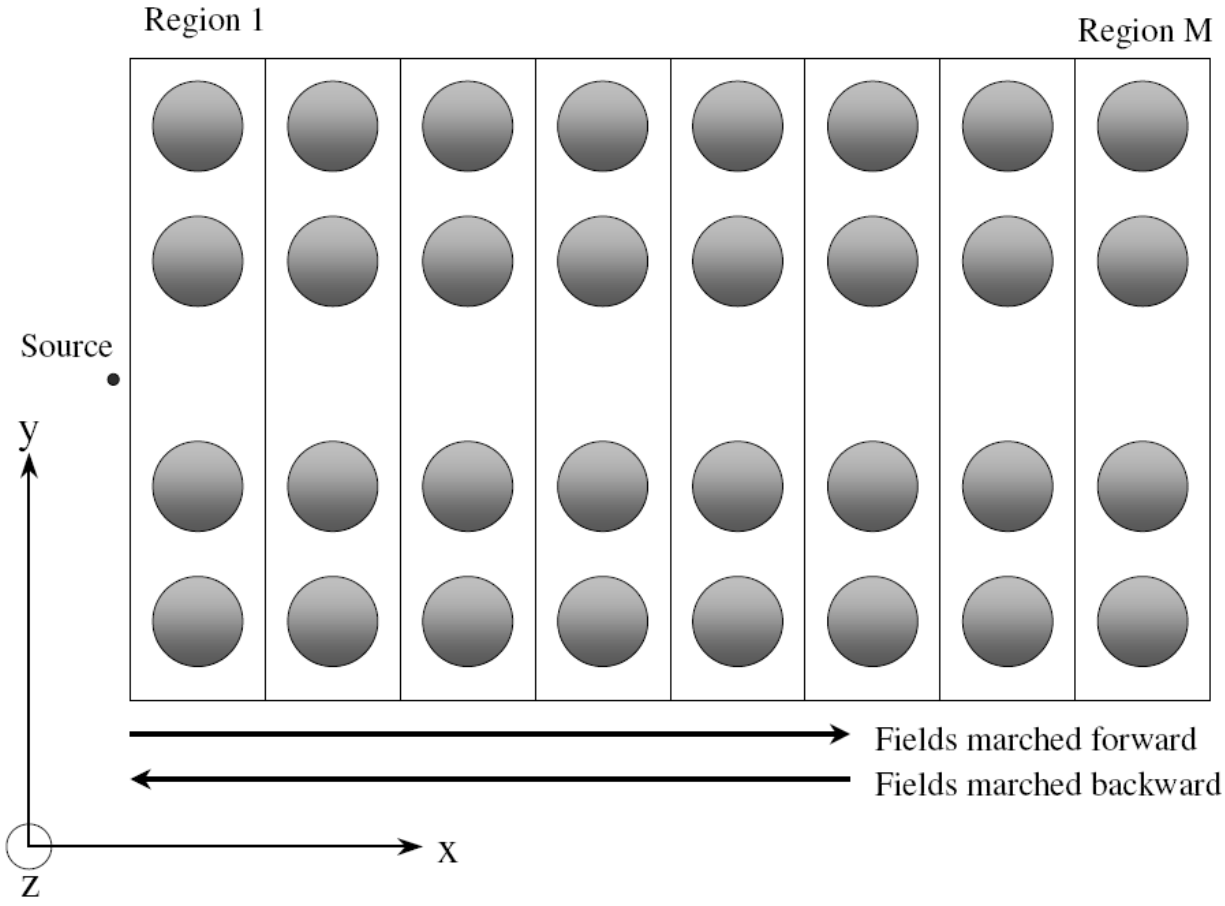

Figure 7.5: Applying the BBFB method to the 2D photonic band gap waveguide.

Equations (7.10) and (7.11) describe the forward and the backward loops of the BFB

technique:

$$\tilde{\mathbf{Z}}_{mm}\tilde{\mathbf{J}}_m^{(k+\frac{1}{2})} = \tilde{\mathbf{V}}_m - \sum_{n<m}\tilde{\mathbf{Z}}_{mn}\tilde{\mathbf{J}}_n^{(k+\frac{1}{2})} - \sum_{n>m}\tilde{\mathbf{Z}}_{mn}\tilde{\mathbf{J}}_n^{(k)} \quad \text{for} \quad m = 1,\ldots,M \tag{7.10}$$

$$\tilde{\mathbf{Z}}_{mm}\tilde{\mathbf{J}}_m^{(k+1)} = \tilde{\mathbf{V}}_m - \sum_{n<m}\tilde{\mathbf{Z}}_{mn}\tilde{\mathbf{J}}_n^{(k+\frac{1}{2})} - \sum_{n>m}\tilde{\mathbf{Z}}_{mn}\tilde{\mathbf{J}}_n^{(k+1)} \quad \text{for} \quad m = M,\ldots,1 \tag{7.11}$$

For the waveguide scenario each 2D rod is separately discretised into P basis functions. All the rods are of the same size, therefore each rod contains the same number of basis functions.

The BBFB method attempts to improve the convergence of the BFB by considering the interactions between each subregion and the neighbouring regions. When applying the BBFB technique to designing the 2D photonic band-gap waveguide, each subregion consists of one line of rods on both sides of the waveguiding channel and the neighbouring subregion is represented by the immediately adjacent line of rods. The forward sweep of the BBFB technique is described by equation (7.12):

$$\begin{bmatrix} \tilde{\mathbf{Z}}_{mm} & \tilde{\mathbf{Z}}_{m(m+1)} \\ \tilde{\mathbf{Z}}_{(m+1)m} & \tilde{\mathbf{Z}}_{(m+1)(m+1)} \end{bmatrix} \begin{bmatrix} \tilde{\mathbf{J}}_m^{(k+\frac{1}{2})} \\ \tilde{\mathbf{B}}_{m+1} \end{bmatrix} = \begin{bmatrix} \tilde{\mathbf{V}}_m \\ \tilde{\mathbf{V}}_{m+1} \end{bmatrix} - \begin{bmatrix} \tilde{\mathbf{L}}_m \\ \tilde{\mathbf{L}}_{m+1} \end{bmatrix} - \begin{bmatrix} \tilde{\mathbf{U}}_m \\ \tilde{\mathbf{U}}_{m+1} \end{bmatrix} \tag{7.12}$$

For this sweep region $m+1$ acts as a buffer for region m. Note that group M will not have a buffer region. For the backward sweep, region $m-1$ acts as a buffer for region m and consequently group 1 does not have a buffer region. This sweep is described by equation (7.13):

$$\begin{bmatrix} \tilde{\mathbf{Z}}_{(m-1)(m-1)} & \tilde{\mathbf{Z}}_{(m-1)m} \\ \tilde{\mathbf{Z}}_{m(m-1)} & \tilde{\mathbf{Z}}_{mm} \end{bmatrix} \begin{bmatrix} \tilde{\mathbf{B}}_{m-1} \\ \tilde{\mathbf{J}}_m^{(k+1)} \end{bmatrix} = \begin{bmatrix} \tilde{\mathbf{V}}_{m-1} \\ \tilde{\mathbf{V}}_m \end{bmatrix} - \begin{bmatrix} \tilde{\mathbf{L}}_{m-1} \\ \tilde{\mathbf{L}}_m \end{bmatrix} - \begin{bmatrix} \tilde{\mathbf{U}}_{m-1} \\ \tilde{\mathbf{U}}_m \end{bmatrix} \tag{7.13}$$

7.4 Results

In Chapters 5 and 6 the Integral Equation formulation was applied to wave scattering problems at 300 MHz. In order to validate our implementation for THz problems the Integral Equation formulation applied to a single 2D rod of radius $r = 46\mu m$ discretised at

a rate of 50 unknowns per wavelength was tested against the analytical Mie series solution [88] at 3THz. The sphere surface currents were computed using both techniques and it can be seen in Figure 7.6 that good agreement between the currents is achieved.

The band gap waveguide is created by periodically aligning a series to Si rods in a rectangular pattern as seen in Figure 7.5. A line source is located on the propagation channel entrance of the waveguide. The frequency of operation is 3THz and a normalised frequency gap map [113] is used in order to obtain the physical parameters of the rods and their spacing.

The ratio $\frac{r}{a}$, where r is the radius of each rod and a is the lattice constant, is selected so that the corresponding normalised frequency is located within one of the available large TM band gaps. The values are normally chosen to be as close as possible to the middle of such a gap. The Buffered Block Forward Backward method was then applied to each configuration. The radius r of the rods has values between $5.3\mu m$ and $8.25\mu m$ and the corresponding lattice constants a are within the $(27.5\mu m, 42.5\mu m)$ range. The length of each waveguide is 20 rods and 3 lines of rods are positioned on each side of the waveguide.

Initially a comparison between the convergence rates of the Block Forward Backward and the Buffered Block Forward Backward Method is performed, as can be seen in Figure 7.8 and Figure 7.9. It can be noted that the BBFB method has a significantly higher convergence rate compared to the BFB technique, although at a higher computational cost. Hence, it can be concluded that, in order to achieve accurate results, a buffer is necessary when applying the Block Forward Backward method.

Next the BBFB method is applied to a range of problems. Figure 7.10 shows the convergence rate of the BBFB method when applied to different waveguide configurations. It represents the normalized error $\log_{10} \frac{||\mathbf{V}-\mathbf{ZJ}||}{||\mathbf{V}||}$ at each iteration. The Buffered Block Forward Backward method achieves a very high convergence rate for the lattice constant $a = 42.5\mu m$ with ratio $\frac{r}{a} = 0.125$ and $a = 32.5\mu m$ with ratio $\frac{r}{a} = 0.225$. The BBFB method applied to the latter configuration was compared to the GMRES solver. GMRES uses a block diagonal preconditioner. Figure 7.11 shows that the BBFB converges significantly quicker than the Krylov solver when applied to the problem of 2D THz dielectric waveguide modelling.

Figure 7.12 represents the electric field along the waveguiding channel, showing very little attenuation. Figure 7.13 shows the power flow across the waveguide. It can be noted that the structure exhibits good waveguiding properties confining the power flow within the hollow between the dielectric rods.

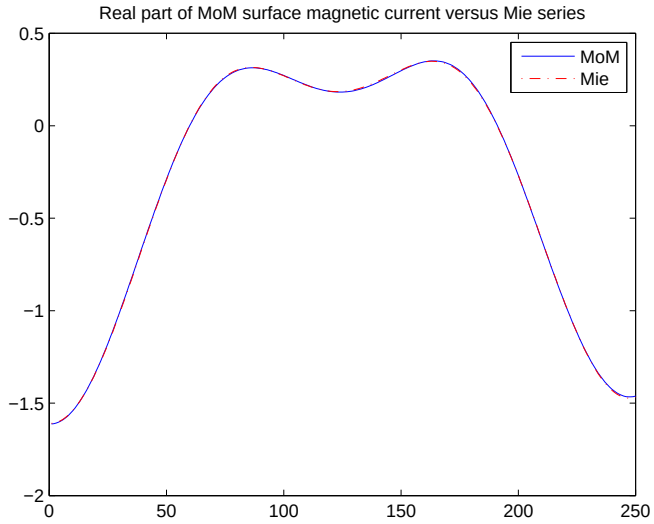

Figure 7.6: IE surface electric field against Mie series.

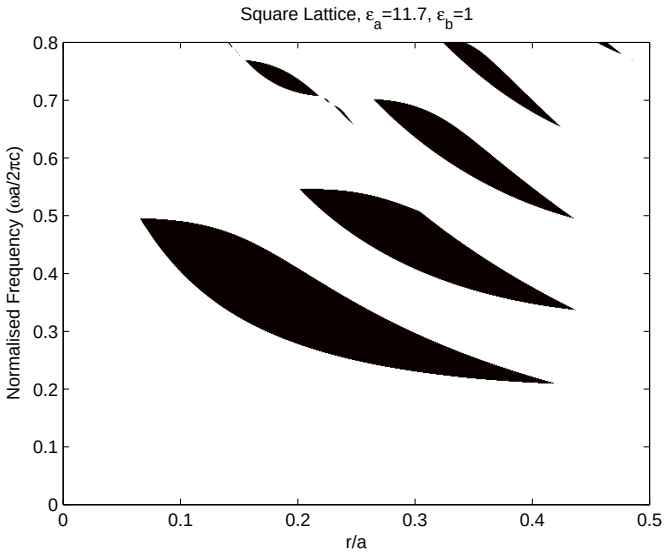

Figure 7.7: Normalised frequency gap map.

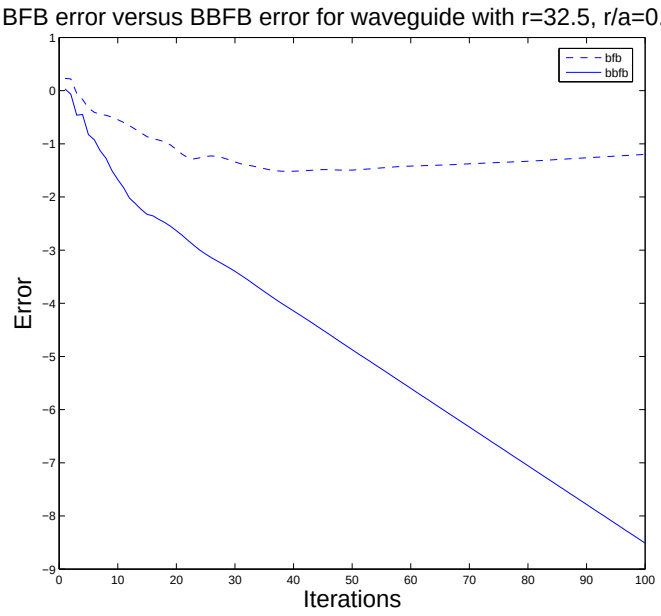

Figure 7.8: Normalised error $\log_{10} \frac{||\mathbf{V}-\mathbf{ZJ}||}{||\mathbf{V}||}$ of BFB and BBFB when applied to a THz waveguide with $a = 32.5\mu m$ and $r/a = 0.225\mu m$.

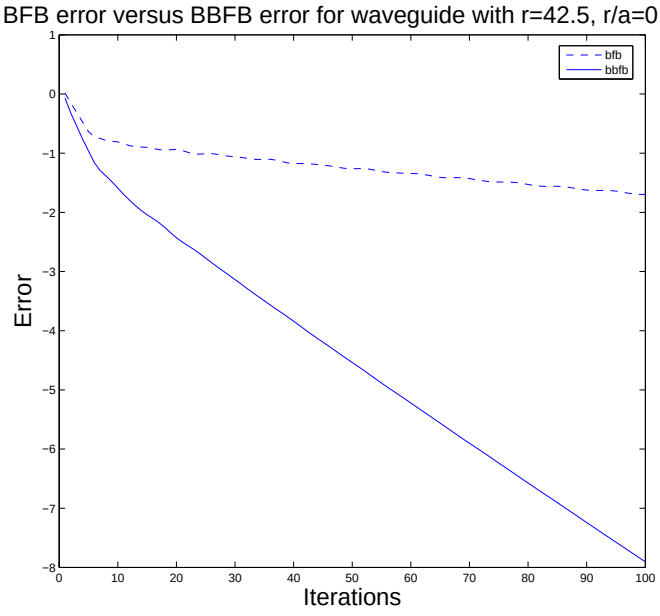

Figure 7.9: Normalised error $\log_{10} \frac{||\mathbf{V}-\mathbf{ZJ}||}{||\mathbf{V}||}$ of BFB and BBFB when applied to a THz waveguide with $a = 42.5\mu m$ and $r/a = 0.125\mu m$.

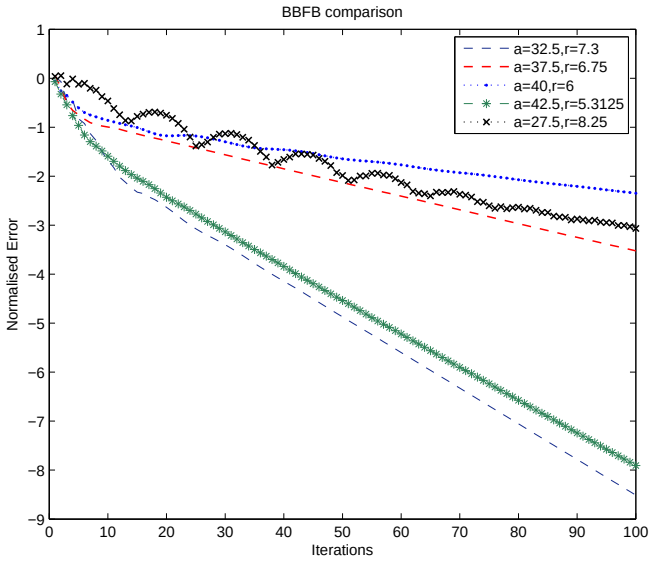

Figure 7.10: Normalised error $\log_{10} \frac{||\mathbf{V}-\mathbf{ZJ}||}{||\mathbf{V}||}$ of BBFB when applied to various band gap waveguides.

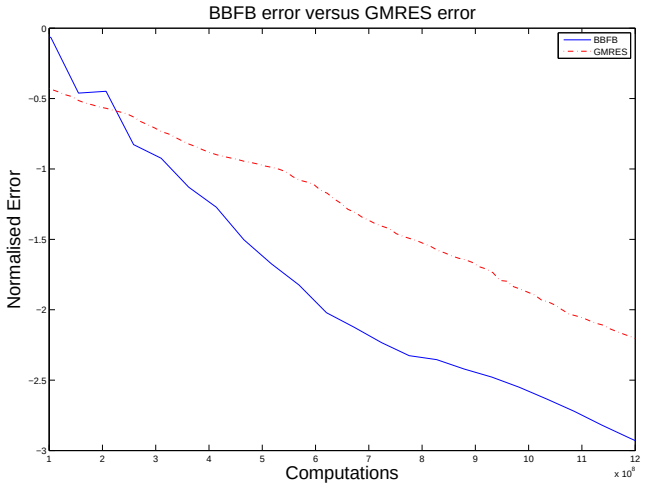

Figure 7.11: The BBFB convergence against GMRES.

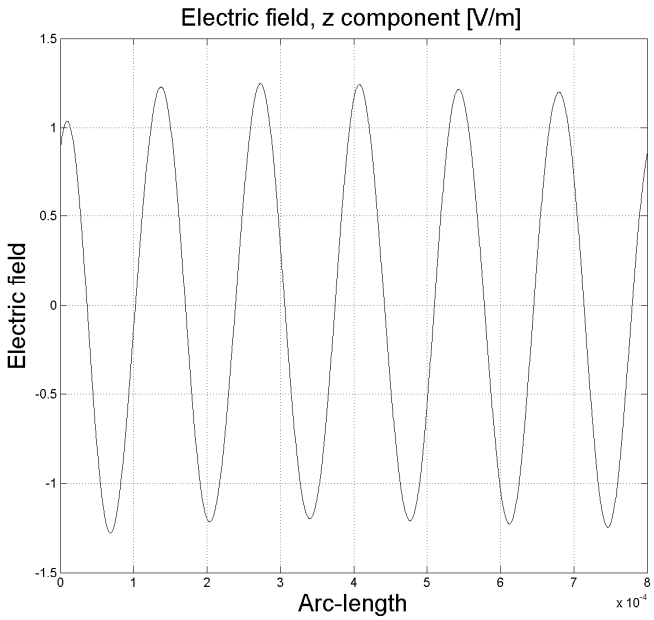

Figure 7.12: Electric field of the dielectric waveguide with the parameters $a = 32.5\mu m$ and $\frac{r}{a} = 0.225$.

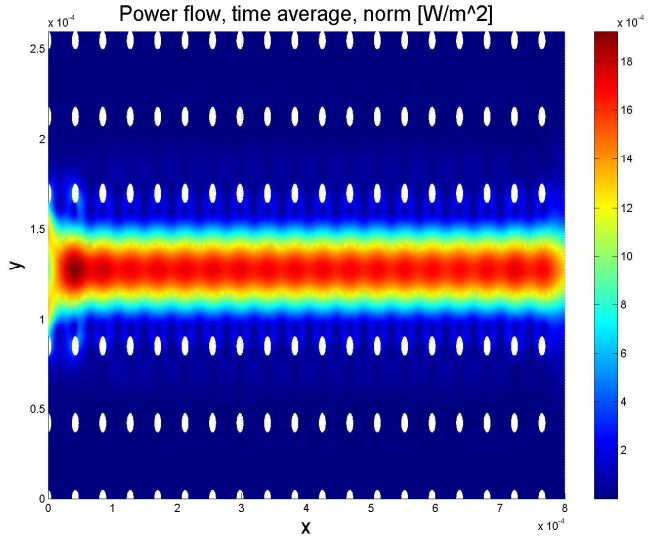

Figure 7.13: Power flow across the dielectric waveguide with the parameters $a = 32.5\mu m$ and $\frac{r}{a} = 0.225$.

7.5 Conclusion

In this chapter the BBFB in combination with the Coupled Electric Field Integral Equation and the MoM was extended to the problem of designing 2D TeraHertz photonic band-gap waveguides. The MoM formulation was validated against the Mie series. The BBFB is shown to achieve highly accurate results when solving the scattered fields within the TeraHertz photonic band-gap structures.

The BBFB was also compared against the preconditioned GMRES and was shown to outperform the latter in terms of convergence. It is thus concluded that the BBFB in conjunction with the Coupled Integral Equation formulation can be used for designing of TeraHertz photonic band-gap waveguides.

Chapter 8

BBFB applied to 3D dielectric scatterers

8.1 Scattering from 3D Homogeneous dielectric Bodies

8.1.1 Introduction

The new Buffered Block Forward Backward Method was presented and it was shown to perform better than other techniques when applied to certain problems. In the previous chapters the BBFB was applied to a perfectly conducting wedge composed of two plates and it was shown to be more efficient than the CGNE technique. The BBFB was used in Chapter 6 to compute the fields scattered from 2D homogeneous dielectric bodies and was shown to perform well in terms of convergence and computational effort. For both perfect electric conductors and 2D dielectric objects the Electric Field Integral Equation Formulation (EFIE) was used. Due to the more complicated structure the scattering from a 2D dielectric body is described in terms of the Coupled Electric Field Integral Equations that express the exterior and interior fields. The drawback of the Coupled Field Integral Equations is that interior resonance problems may occur. To avoid these complications the Combined Field Integral Equation is used when solving the fields scattered from 3D homogeneous dielectric bodies. The Combined Field Integral Equation is then discretised

using the Method of Moments with N testing and basis functions which yields the matrix equation

$$\mathbf{ZJ} = \mathbf{V} \tag{8.1}$$

In the 3D case the $\mathbf{Z}$ matrix is of order $2N$, and $\mathbf{J}$ and $\mathbf{V}$ are column vectors of order $2N$, where N is the number of edges associated with the triangular patch discretisation.

8.1.2 Combined Field Integral Equation Formulation

The problem of scattering from a 3D homogeneous dielectric body is formulated using the Combined Field Integral Equations. The Combined Field Integral Equation was developed in Chapter 3 and is briefly reviewed in this section. The expressions for the exterior problem are [3]:

$$\bar{\mathbf{K}} = -\hat{n} \times \bar{\mathbf{E}}^{inc} - \hat{n} \times \{\frac{\eta}{jk}(\nabla\nabla \cdot \bar{\mathbf{A}} + k^2 \bar{\mathbf{A}}) - \nabla \times \bar{\mathbf{F}}\}_{S^+} \tag{8.2}$$

$$\bar{\mathbf{J}} = \hat{n} \times \bar{\mathbf{H}}^{inc} + \hat{n} \times \{\nabla \times \bar{\mathbf{A}} + \frac{\nabla\nabla \cdot \bar{\mathbf{F}} + k^2 \bar{\mathbf{F}}}{jk\eta}\}_{S^+} \tag{8.3}$$

whereas the interior problem has the following formulation [3]:

$$\bar{\mathbf{K}} = -\hat{n} \times \bar{\mathbf{E}}^{inc} - \hat{n} \times \{\frac{\eta_d}{jk_d}(\nabla\nabla \cdot \bar{\mathbf{A}}_d + k^2 \bar{\mathbf{A}}_d) - \nabla \times \bar{\mathbf{F}}_d\}_{S^-} \tag{8.4}$$

$$\bar{\mathbf{J}} = \hat{n} \times \bar{\mathbf{H}}^{inc} + \hat{n} \times \{\nabla \times \bar{\mathbf{A}}_d + \frac{\nabla\nabla \cdot \bar{\mathbf{F}}_d + k_d^2 \bar{\mathbf{F}}_d}{jk_d\eta_d}\}_{S^-} \tag{8.5}$$

where $\bar{\mathbf{J}}$ and $\bar{\mathbf{K}}$ are the equivalent exterior electric and magnetic surface current densities. $\bar{\mathbf{A}}$ and $\bar{\mathbf{F}}$ are the magnetic and electric vector potential functions in the exterior medium, whereas $\bar{\mathbf{A}}_d$ and $\bar{\mathbf{F}}_d$ are the magnetic and electric vector potential functions in the dielectric material [3]. The CFIE is thus given by:

$$-\hat{n}\times\bar{\mathbf{E}}^{inc} = \hat{n}\times\{\frac{\eta}{jk}(\nabla\nabla \cdot \bar{\mathbf{A}} + k^2 \bar{\mathbf{A}}) - \nabla \times \bar{\mathbf{F}}\}_{S^+} + \hat{n}\times\{\frac{\eta_d}{jk_d}(\nabla\nabla \cdot \bar{\mathbf{A}}_d + k_d^2 \bar{\mathbf{A}}_d) - \nabla \times \bar{\mathbf{F}}_d\}_{S^-} \tag{8.6}$$

$$-\hat{n}\times\bar{\mathbf{H}}^{inc} = \hat{n}\times\{\nabla\times\bar{\mathbf{A}} + \frac{\nabla\nabla\cdot\bar{\mathbf{F}} + k^2\bar{\mathbf{F}}}{jk_1\eta}\}_{S^+} + \hat{n}\times\{\nabla\times\bar{\mathbf{A}}_d + \frac{\nabla\nabla\cdot\bar{\mathbf{F}}_d + k_d^2\bar{\mathbf{F}}_d}{jk_d\eta_d}\}_{S^-} \quad (8.7)$$

After applying the method of moments with N RWG basis functions the matrix equation is obtained [3]:

$$\begin{bmatrix} \mathbf{A} & \mathbf{B} \\ \mathbf{C} & \mathbf{D} \end{bmatrix} \begin{bmatrix} \mathbf{j} \\ \mathbf{k} \end{bmatrix} = \begin{bmatrix} \mathbf{e} \\ \mathbf{h} \end{bmatrix} \quad (8.8)$$

The **A**, **B**, **C** and **D** elements are matrices of order N each, which means that **Z** is a $2N \times 2N$ matrix. In the same manner as it was done for the 2D dielectric case, we can explicitly write equation (8.8):

$$\begin{bmatrix} A_{11} & A_{12} & A_{13} & \dots & A_{1N} & B_{11} & B_{12} & B_{13} & \dots & B_{1N} \\ A_{21} & A_{22} & A_{23} & \dots & A_{2N} & B_{21} & B_{22} & B_{23} & \dots & B_{2N} \\ \vdots & \vdots & \vdots & \vdots & \vdots & \vdots & \vdots & \vdots & \vdots & \vdots \\ A_{N1} & A_{N2} & A_{N3} & \dots & A_{NN} & B_{N1} & B_{N2} & B_{N3} & \dots & B_{NN} \\ C_{11} & C_{12} & C_{13} & \dots & C_{1N} & D_{11} & D_{12} & D_{13} & \dots & D_{1N} \\ C_{21} & C_{22} & C_{23} & \dots & C_{2N} & D_{21} & D_{22} & D_{23} & \dots & D_{2N} \\ \vdots & \vdots & \vdots & \vdots & \vdots & \vdots & \vdots & \vdots & \vdots & \vdots \\ C_{N1} & C_{N2} & C_{N3} & \dots & C_{NN} & D_{N1} & D_{N2} & D_{N3} & \dots & D_{NN} \end{bmatrix} \begin{bmatrix} j_1 \\ j_2 \\ \vdots \\ j_N \\ k_1 \\ k_2 \\ \vdots \\ k_N \end{bmatrix} = \begin{bmatrix} e_1 \\ e_2 \\ \vdots \\ e_N \\ h_1 \\ h_2 \\ \vdots \\ h_N \end{bmatrix}$$

where the elements A_{mn}, B_{mn}, C_{mn} and D_{mn} are derived in Section 3.2.4.

The explicit equation is rewritten in order to facilitate a sequential progression through the domains of electric and magnetic currents. For this the **Z** matrix as well as the **J** and **V** vectors are rearranged accordingly.

$$\begin{bmatrix} A_{11} & B_{11} & A_{12} & B_{12} & A_{13} & B_{13} & \dots & A_{1N} & B_{1N} \\ C_{11} & D_{11} & C_{12} & D_{12} & C_{13} & D_{13} & \dots & C_{1N} & D_{1N} \\ A_{21} & B_{21} & A_{22} & B_{22} & A_{23} & B_{23} & \dots & A_{2N} & B_{2N} \\ C_{21} & D_{21} & C_{22} & D_{22} & C_{23} & D_{23} & \dots & C_{2N} & D_{2N} \\ \vdots & \vdots & \vdots & \vdots & \vdots & \vdots & \vdots & \vdots & \vdots \\ A_{N1} & B_{N1} & A_{N2} & B_{N2} & A_{N3} & B_{N3} & \dots & A_{NN} & B_{NN} \\ C_{N1} & D_{N1} & C_{N2} & D_{N2} & C_{N3} & D_{N3} & \dots & C_{NN} & D_{NN} \end{bmatrix} \begin{bmatrix} j_1 \\ k_1 \\ j_2 \\ k_2 \\ \vdots \\ j_N \\ k_N \end{bmatrix} = \begin{bmatrix} e_1 \\ h_1 \\ e_2 \\ h_2 \\ \vdots \\ e_N \\ h_N \end{bmatrix}$$

A more compact version of the previous equations is written in terms of submatrices of $\mathbf{Z}_{mn}$ of size 2×2, each one of them representing the interaction between the electric and the magnetic currents within the $\mathbf{J}$ vector:

$$\begin{bmatrix} \mathbf{Z}_{11} & \mathbf{Z}_{12} & \dots & \mathbf{Z}_{1N} \\ \mathbf{Z}_{21} & \mathbf{Z}_{22} & \dots & \mathbf{Z}_{2N} \\ \vdots & \vdots & \vdots & \vdots \\ \mathbf{Z}_{N1} & \mathbf{Z}_{N2} & \dots & \mathbf{Z}_{NN} \end{bmatrix} \begin{bmatrix} \mathbf{J}_1 \\ \mathbf{J}_2 \\ \vdots \\ \mathbf{J}_N \end{bmatrix} = \begin{bmatrix} \mathbf{V}_1 \\ \mathbf{V}_2 \\ \vdots \\ \mathbf{V}_N \end{bmatrix} \tag{8.9}$$

where

$$\mathbf{Z}_{mn} = \begin{bmatrix} A_{mn} & B_{mn} \\ C_{mn} & D_{mn} \end{bmatrix} \tag{8.10}$$

$$\mathbf{J}_n = \begin{bmatrix} j_n \\ k_n \end{bmatrix} \tag{8.11}$$

$$\mathbf{V}_n = \begin{bmatrix} e_n \\ h_n \end{bmatrix} \tag{8.12}$$

The basis functions are grouped into M different groups. This leads to:

$$\begin{bmatrix} \tilde{\mathbf{Z}}_{11} & \tilde{\mathbf{Z}}_{12} & \dots & \tilde{\mathbf{Z}}_{1M} \\ \tilde{\mathbf{Z}}_{21} & \tilde{\mathbf{Z}}_{22} & \dots & \tilde{\mathbf{Z}}_{2M} \\ \vdots & \vdots & \vdots & \vdots \\ \tilde{\mathbf{Z}}_{M1} & \tilde{\mathbf{Z}}_{M2} & \dots & \tilde{\mathbf{Z}}_{MM} \end{bmatrix} \begin{bmatrix} \tilde{\mathbf{J}}_1 \\ \tilde{\mathbf{J}}_2 \\ \vdots \\ \tilde{\mathbf{J}}_M \end{bmatrix} = \begin{bmatrix} \tilde{\mathbf{V}}_1 \\ \tilde{\mathbf{V}}_2 \\ \vdots \\ \tilde{\mathbf{V}}_M \end{bmatrix} \tag{8.13}$$

where $\tilde{\mathbf{Z}}_{mn}$ contains the specific interactions between the basis functions within the groups m and n. The forward sweep of the BBFB technique is [86; 87]:

$$\begin{bmatrix} \tilde{\mathbf{Z}}_{m} & \tilde{\mathbf{Z}}_{m(m+1)} \\ \tilde{\mathbf{Z}}_{(m+1)m} & \tilde{\mathbf{Z}}_{(m+1)(m+1)} \end{bmatrix} \begin{bmatrix} \tilde{\mathbf{J}}_m^{(k+\frac{1}{2})} \\ \tilde{\mathbf{B}}_{m+1} \end{bmatrix} = \begin{bmatrix} \tilde{\mathbf{V}}_m \\ \tilde{\mathbf{V}}_{m+1} \end{bmatrix} - \begin{bmatrix} \tilde{\mathbf{L}}_m \\ \tilde{\mathbf{L}}_{m+1} \end{bmatrix} - \begin{bmatrix} \tilde{\mathbf{U}}_m \\ \tilde{\mathbf{U}}_{m+1} \end{bmatrix}$$

and the backward sweep is represented by:

$$\begin{bmatrix} \tilde{\mathbf{Z}}_{(m-1)(m-1)} & \tilde{\mathbf{Z}}_{(m-1)m} \\ \tilde{\mathbf{Z}}_{m(m-1)} & \tilde{\mathbf{Z}}_{mm} \end{bmatrix} \begin{bmatrix} \tilde{\mathbf{B}}_{m-1} \\ \tilde{\mathbf{J}}_m^{(k+1)} \end{bmatrix} = \begin{bmatrix} \tilde{\mathbf{V}}_{m-1} \\ \tilde{\mathbf{V}}_m \end{bmatrix} - \begin{bmatrix} \tilde{\mathbf{L}}_{m-1} \\ \tilde{\mathbf{L}}_m \end{bmatrix} - \begin{bmatrix} \tilde{\mathbf{U}}_{m-1} \\ \tilde{\mathbf{U}}_m \end{bmatrix}$$

8.1.3 Results

Testing against the Mie series

The implementation was validated by comparison with the Mie series. The Mie series theory is described by Stratton in [115]. Consider a 3D homogeneous dielectric sphere of radius a and propagation constant k_d placed in a free space environment with the propagation constant k_0 and illuminated by a plane wave as presented in Figure (8.1). The total fields have the expressions:

$$\bar{\mathbf{E}}^t = \bar{\mathbf{E}}^i + \bar{\mathbf{E}}^s \tag{8.14}$$

$$\bar{\mathbf{H}}^t = \bar{\mathbf{H}}^i + \bar{\mathbf{H}}^s \tag{8.15}$$

where $\bar{\mathbf{E}}^t$ and $\bar{\mathbf{H}}^t$ represent the total fields, $\bar{\mathbf{E}}^i$ and $\bar{\mathbf{H}}^i$ define the incident fields, and $\bar{\mathbf{E}}^s$ and $\bar{\mathbf{H}}^s$ are the scattered fields. The incident fields are formulated as follows:

$$\bar{\mathbf{E}}^i = E^0 \sum_{n=1}^{\infty} \jmath^n \frac{2n+1}{n(n+1)} (\mathbf{m}_{o1n}^{(1)} - \jmath \mathbf{n}_{e1n}^{(1)}) \tag{8.16}$$

$$\bar{\mathbf{H}}^i = -\frac{k_0 E^0}{\mu_0 \omega} \sum_{n=1}^{\infty} \jmath^n \frac{2n+1}{n(n+1)} (\mathbf{m}_{e1n}^{(1)} + \jmath \mathbf{n}_{o1n}^{(1)}) \tag{8.17}$$

where E^0 represents the amplitude of the incident field, and the terms $\mathbf{m}_{o1n}^{(1)}$, $\mathbf{m}_{e1n}^{(1)}$, $\mathbf{n}_{o1n}^{(1)}$, and $\mathbf{n}_{e1n}^{(1)}$ are given by:

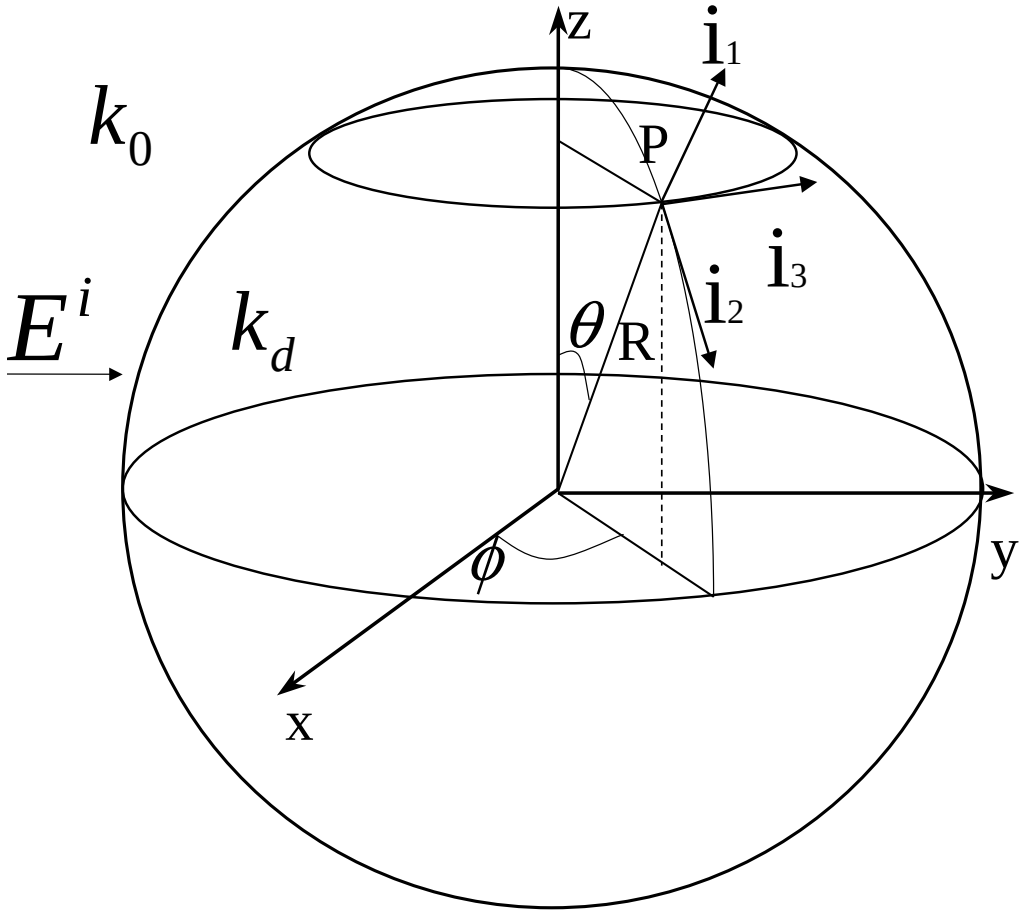

Figure 8.1: A homogeneous dielectric sphere illuminated by a plane incident wave

$$\mathbf{m}_{o1n}^{(1)} = \frac{1}{\sin\theta} j_n(k_0R)P_n^1(\cos\theta)\cos\phi\mathbf{i_2} - j_n(k_0R)\frac{\partial P_n^1}{\partial\theta}\sin\phi\mathbf{i_3} \quad (8.18)$$

$$\mathbf{m}_{e1n}^{(1)} = -\frac{1}{\sin\theta} j_n(k_0R)P_n^1(\cos\theta)\sin\phi\mathbf{i}_2 - j_n(k_0R)\frac{\partial P_n^1}{\partial\theta}\cos\phi\mathbf{i}_3 \quad (8.19)$$

$$\mathbf{n}_{o1n}^{(1)} = \frac{n(n+1)}{k_0R} j_n(k_0R)P_n^1(\cos\theta)\sin\phi\mathbf{i_1} \quad (8.20)$$

$$+ \frac{1}{k_0R}[k_0Rj_n(k_0)R]'\frac{\partial P_n^1}{\partial\theta}\sin\phi\mathbf{i}_2 \quad (8.21)$$

$$+ \frac{1}{k_0R\sin\theta}[k_0Rj_n(k_0R)]'P_n^1(\cos\theta)\cos\phi\mathbf{i}_3 \quad (8.22)$$

$$\mathbf{n}_{e1n}^{(1)} = \frac{n(n+1)}{k_0R} j_n(k_0R)P_n^1(\cos\theta)\cos\phi\mathbf{i_1} \quad (8.23)$$

$$+ \frac{1}{k_0R}[k_0Rj_n(k_0)R]'\frac{\partial P_n^1}{\partial\theta}\sin\phi\mathbf{i}_2 \quad (8.24)$$

$$- \frac{1}{k_0R\sin\theta}[k_0Rj_n(k_0R)]'P_n^1(\cos\theta)\sin\phi\mathbf{i}_3 \quad (8.25)$$

where $j_n(*)$ represents the spherical Bessel function of order n, R is the distance from the centre of the sphere to the point where the fields are to be evaluated, k_0 represents the propagation constant of the outside medium (in this case free space), P_n^1 represents the Legendre function and $\mathbf{i}_1$, $\mathbf{i}_2$ and $\mathbf{i}_3$ are unit vectors in the direction of increasing R, θ and ϕ. The scattered fields for $R > a$ are given by:

$$\bar{\mathbf{E}}^s = E^0\sum_{n=1}^{\infty} \jmath^n \frac{2n+1}{n(n+1)}(a_n^r\mathbf{m}_{o1n}^{(3)} - \jmath b_n^r\mathbf{n}_{e1n}^{(3)}) \quad (8.26)$$

$$\bar{\mathbf{H}}^s = -\frac{k_0}{\omega\mu_2}E^0\sum_{n=1}^{\infty} \jmath^n \frac{2n+1}{n(n+1)}(b_n^r\mathbf{m}_{e1n}^{(3)} + \jmath a_n^r\mathbf{n}_{o1n}^{(3)}) \quad (8.27)$$

where the terms $\mathbf{m}_{o1n}^{(3)}$, $\mathbf{n}_{e1n}^{(3)}$, $\mathbf{m}_{e1n}^{(3)}$ and $\mathbf{n}_{o1n}^{(3)}$ are obtained by replacing the spherical Bessel function $j_n(k_0R)$ in Equations (8.18-8.25) with the spherical Hankel function $h_n^{(1)}(k_0R)$. The transmitted fields valid for $R < a$ are formulated by replacing k_0 with k_d in Equation (8.26) and (8.27):

$$\bar{\mathbf{E}}^t = E^0\sum_{n=1}^{\infty} \jmath^n \frac{2n+1}{n(n+1)}(a_n^t\mathbf{m}_{o1n}^{(1)} - \jmath b_n^t\mathbf{n}_{e1n}^{(1)}) \quad (8.28)$$

$$\bar{\mathbf{H}}^t = -\frac{k_d}{\omega\mu_d}E^0\sum_{n=1}^{\infty} \jmath^n \frac{2n+1}{n(n+1)}(b_n^t\mathbf{m}_{e1n}^{(3)} + \jmath a_n^t\mathbf{n}_{o1n}^{(1)}) \quad (8.29)$$

The currents are to be calculated on the surface of the sphere and the boundary conditions have to be satisfied for $R = a$:

$$\mathbf{i}_1 \times (\bar{\mathbf{E}}^i + \bar{\mathbf{E}}^s) = \mathbf{i}_1 \times \bar{\mathbf{E}}^t \tag{8.30}$$

$$\mathbf{i}_1 \times (\bar{\mathbf{H}}^i + \bar{\mathbf{H}}^s) = \mathbf{i}_1 \times \bar{\mathbf{H}}^t \tag{8.31}$$

And the terms a_n^r and b_n^r are given by:

$$a_n^r = -\frac{\mu_d j_n(N\rho)[\rho j_n(\rho)]' - \mu_0 j_n(\rho)[N\rho j_n(N\rho)]'}{\mu_d j_n(N\rho)[\rho h_n^{(1)}(\rho)]' - \mu_0 h_n^{(1)}(\rho)[N\rho j_n(N\rho)]'} \tag{8.32}$$

$$b_n^r = -\frac{\mu_d j_n(\rho)[N\rho j_n(N\rho)]' - \mu_0 N^2 j_n(N\rho)[\rho j_n(\rho)]'}{\mu_d h_n^{(1)}(\rho)[N\rho j_n(N\rho)]' - \mu_0 N^2 j_n(N\rho)[\rho h_n^{(1)}(\rho)]'} \tag{8.33}$$

where $N = \frac{k_d}{k_0}$ and $\rho = k_0 a$. The expansion coefficients a_n^t and b_n^t are found by solving the equations:

$$a_n^t j_n(N\rho) - a_n^s h_n^{(1)}(\rho) = j_n(\rho) \tag{8.34}$$

$$\mu_0 a_n^t [N\rho j_n(N\rho)]' - \mu_d a_n^r [\rho h_n^{(1)}(\rho)]' = \mu_d [\rho j_n(\rho)]' \tag{8.35}$$

$$\mu_0 N b_n^t j_n(N\rho) - \mu_d b_n^s h_n^{(1)}(\rho) = \mu_d j_n(\rho) \tag{8.36}$$

$$b_n^t [N\rho j_n(N\rho)]' - N b_n^s [\rho h_n^{(1)}(\rho)]' = N[\rho j_n(\rho)]' \tag{8.37}$$

Note that the surface fields $\bar{\mathbf{E}}^t$ and $\bar{\mathbf{H}}^t$ contain two tangential components each E_θ, E_ϕ and H_θ, H_ϕ respectively.

When computing the surface fields using the Integral Equation approach the values for $\bar{\mathbf{J}}$ and $\bar{\mathbf{K}}$ can be obtained from:

$$\bar{\mathbf{J}}(\mathbf{r}) = \sum_{n=1}^{N} j_n \mathbf{b}_n(\mathbf{r}) \tag{8.38}$$

$$\bar{\mathbf{K}}(\mathbf{r}) = \sum_{n=1}^{N} k_n \mathbf{b}_n(\mathbf{r}) \tag{8.39}$$

where $\mathbf{b}_n$ represents the basis functions that belong to the same line considered for the Mie

series. Having solved the matrix equation and obtained j_n and k_n the current densities J_θ, J_ϕ, K_θ and K_ϕ can be computed along a test line on the sphere surface and compared to the fields obtained using the Mie series.

The method was tested for a sphere with the radius of $r = \frac{1}{k_0}$ which leads to 480 basis functions and a system size of 960×960. The matrix equation was solved by direct matrix inversion. The results are presented in figures (8.2-8.3).

A line from the north pole to the south pole was chosen along the surface of the sphere. The currents are calculated for 40 surface points on the chosen line. Figures (8.2-8.3) show the comparison between the currents obtained using the Method of Moments and the currents obtained using the Mie series. It can be seen that satisfactory agreement is achieved. The agreement between the results is not perfect due to the limitations of using flat triangular patches to model the 3D sphere.

A higher level of agreement can be seen when comparing the two techniques applied to a larger sphere. Consider a homogeneous sphere with the radius $r = 2 \cdot \frac{1}{k_0}$, where the total number of basis functions is equal to 1920. The comparisons between the results obtained using the Mie series and the MoM approach are presented in Figures (8.4-8.5), where it can be observed that the currents obtained using the MoM follow Mie series currents much more precisely. This is due to the fact that the curvature of the larger sphere is smaller, therefore the 3D surface can be modelled more precisely using the flat triangular patches.

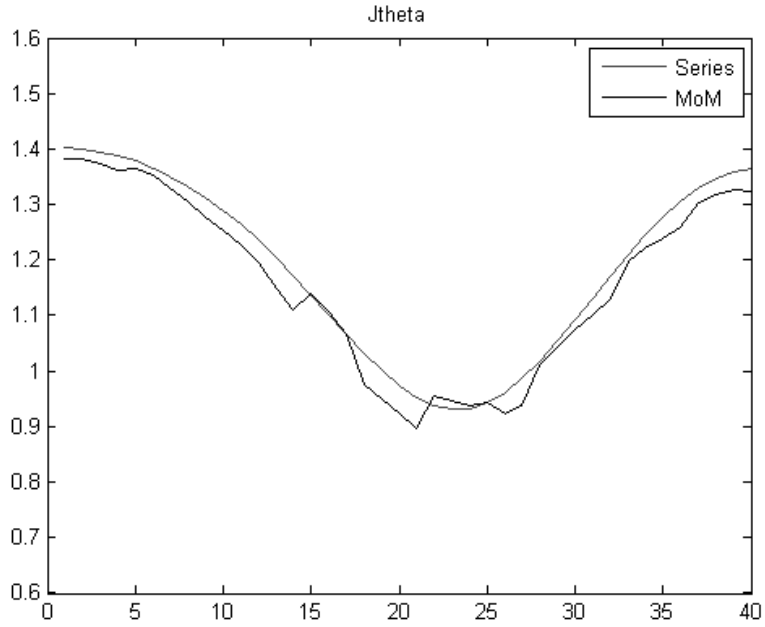

(a) θ component of the Electric Current

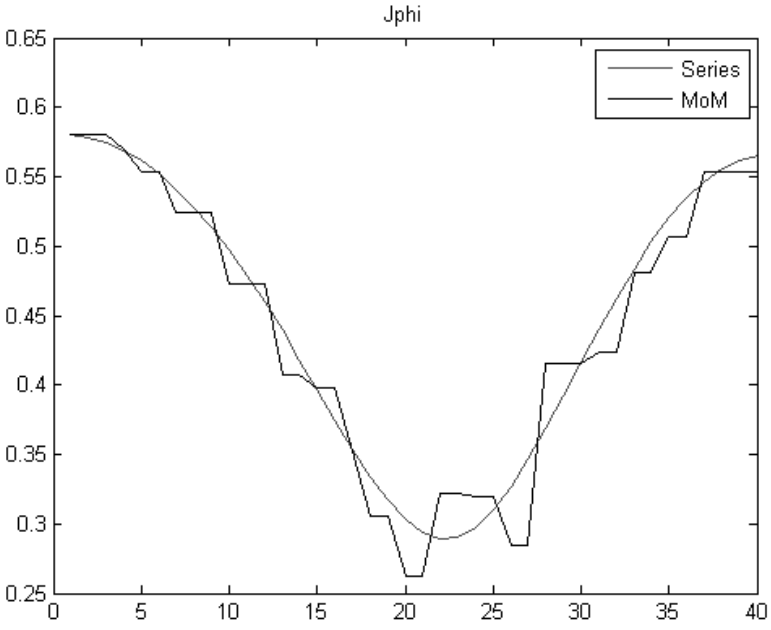

(b) ϕ component of the Electric Current

Figure 8.2: Electric Current obtained using the Mie series vs MoM for $r = \frac{1}{k_0}$

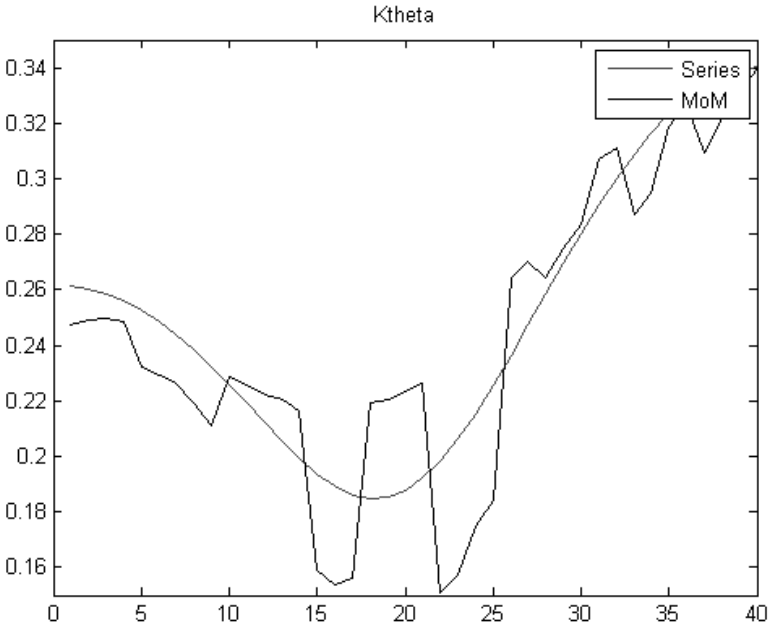

(a) θ component of the Magnetic Current

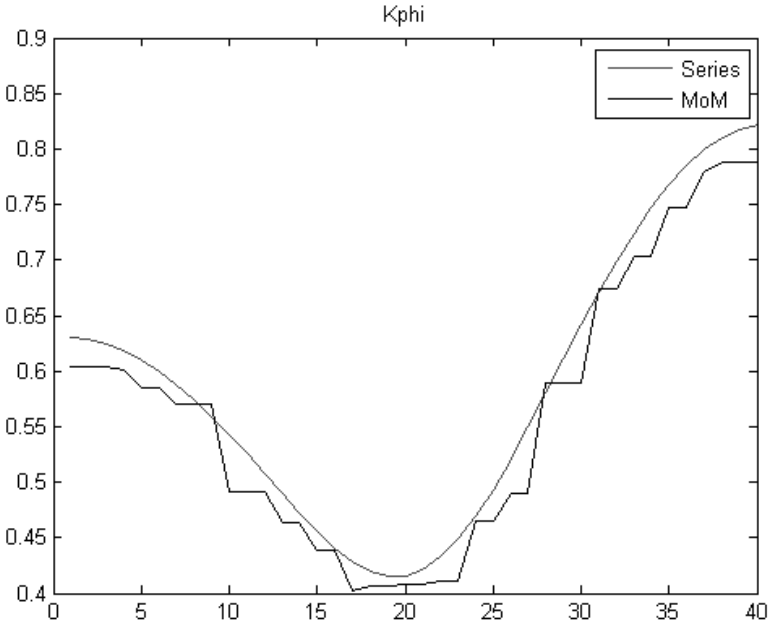

(b) ϕ component of the Magnetic Current

Figure 8.3: Magnetic Current obtained using the Mie series vs MoM for $r = \frac{1}{k_0}$

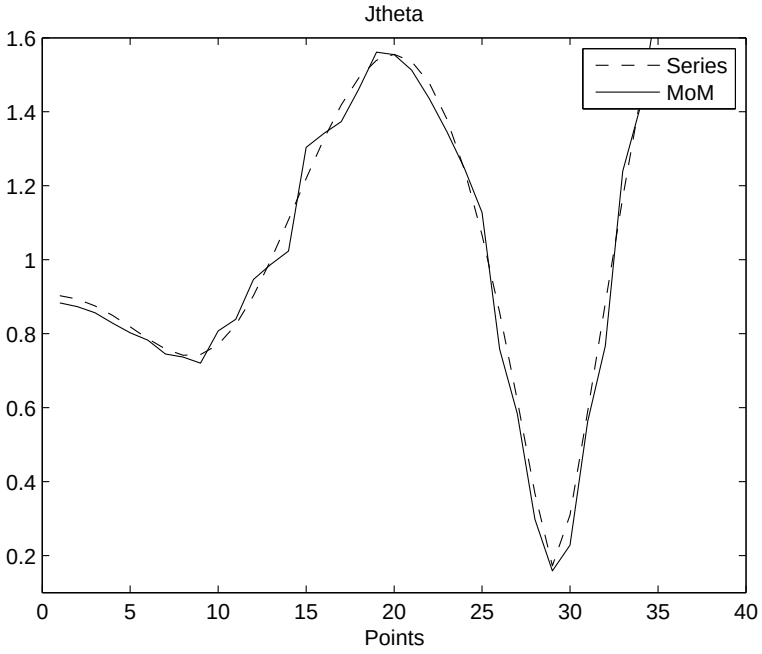

(a) θ component of the Electric Current

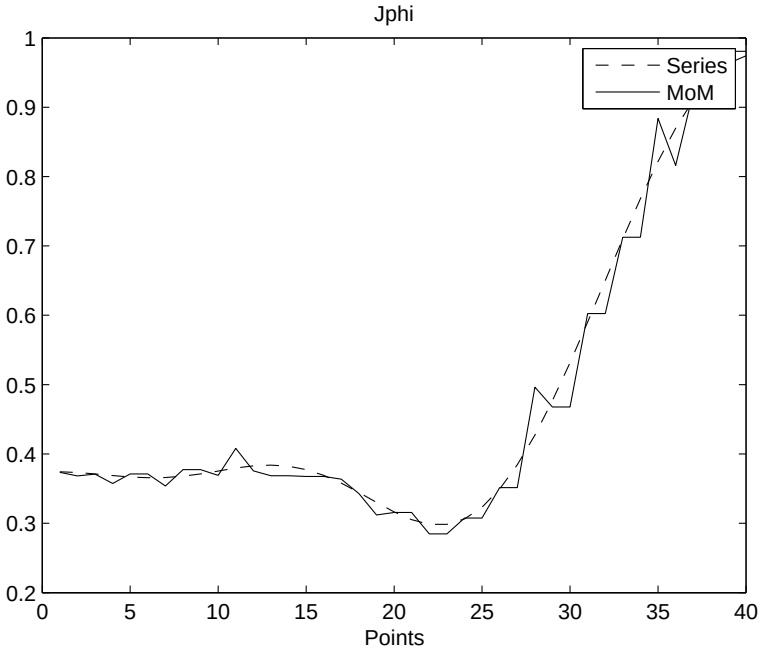

(b) ϕ component of the Electric Current

Figure 8.4: Electric current obtained using the Mie series vs MoM for $r = 2 \cdot \frac{1}{k_0}$.

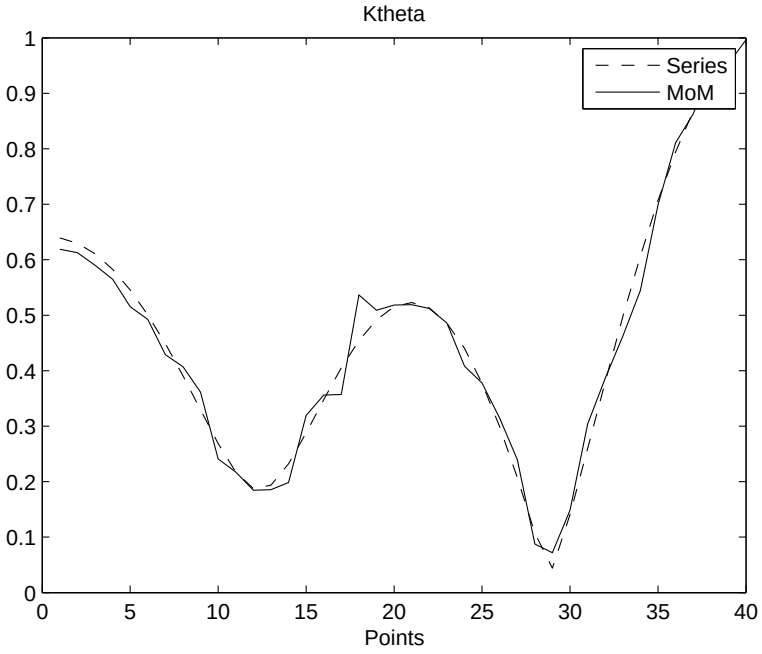

(a) θ component of the Magnetic Current

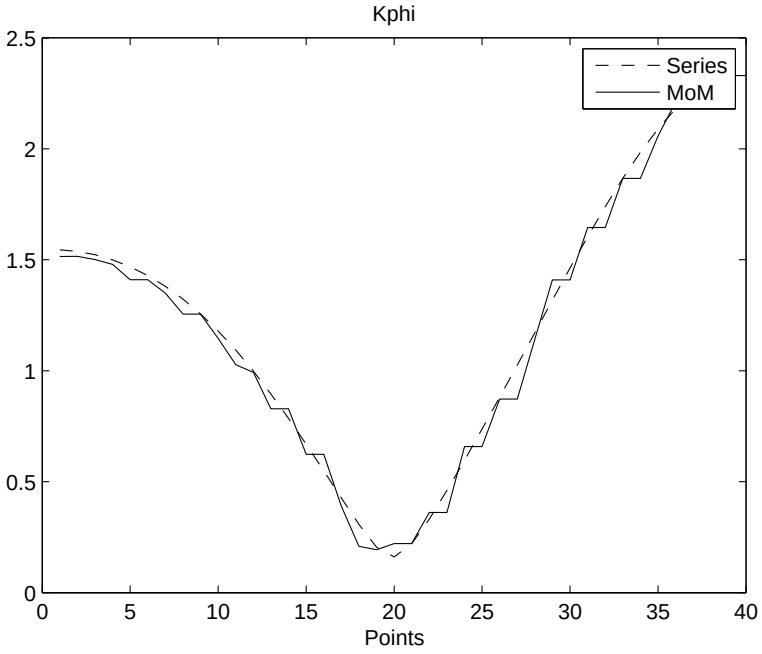

(b) ϕ component of the Magnetic Current

Figure 8.5: Magnetic Current obtained using the Mie series vs MoM for $r = 2 \cdot \frac{1}{k_0}$.

Performance of the BBFB method applied to 3D dielectric homogeneous scatterrers

In order to use the Buffered Block Forward Backward Method for calculating the fields scattered from a 3D homogeneous dielectric object a similar procedure to the one performed in the 2D case was devised. A 3D coarse grid was imposed over the scatterer as can be seen in figure (8.6):

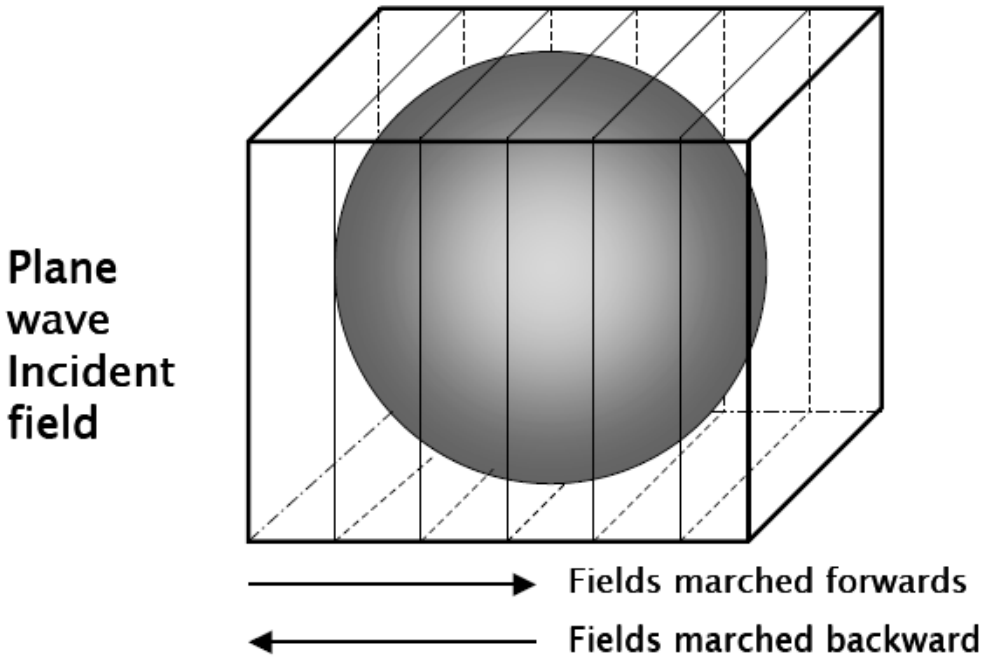

Figure 8.6: The coarse grid superimposed over the homogeneous dielectric sphere, organizing the N basis functions into M groups.

By imposing the 3D coarse grid the surface of the scatterer is partitioned into sections. For the purpose of clarity these sections are herein referred to as slices. After imposing the grid over the structure all the basis functions are rearranged accordingly, so that the basis functions $1, \ldots\ s_1$ belong to the first slice, the basis functions $s_1 + 1, \ldots\ s_2$ belong to the second slice and basis functions $s_{M-1} + 1, \ldots\ s_M$ are contained in slice M.

Consider a sphere of radius $r = \frac{1}{k_0}$ where k_0 is the wave number in free space.

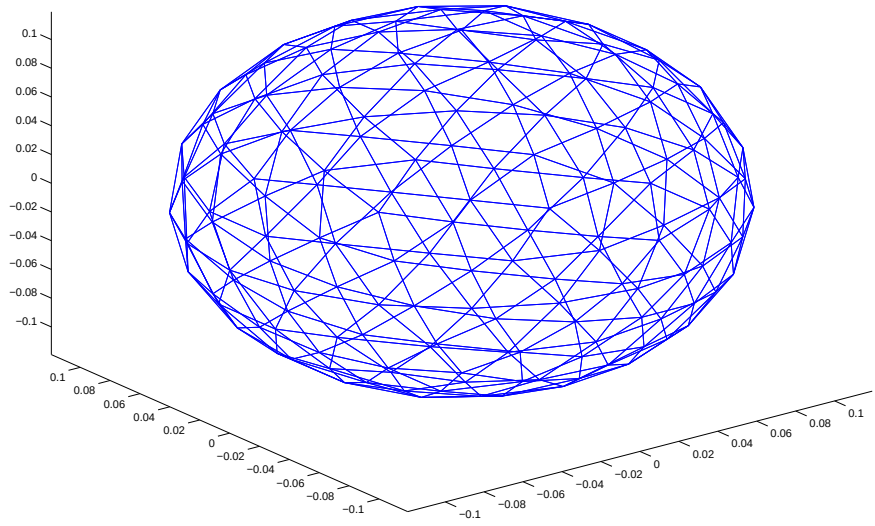

Figure 8.7: Homogeneous dielectric Sphere discretised using N basis functions.

The scattering object is illuminated by a plane wave of frequency $400MHz$. The BBFB is applied to various spheres of the same radius, but with different relative permittivities ε_r. These results are depicted in Table 8.1. The first column of the table represents the relative permittivity of the sphere. The order of the $\mathbf{Z}$ matrix is given in Column 2. In column 3 the total number of slices are given, whereas the grouping arrangement chosen is presented in column 4, whereby 3/2 represents 3 slices in the main subgroup and 2 slices in the buffer. Columns $5-8$ depict the normalised error $\psi = \log_{10} \frac{||\mathbf{V}-\mathbf{Z}\mathbf{J}_{BBFB}||}{||\mathbf{V}||}$, where $\mathbf{J}_{BBFB}$ represent the surface fields computed using the BBFB technique, where $\psi^{(k)}$ is computed in terms of $\mathbf{J}^{(k)}_{BBFB}$. Column 9 depicts the total time required to perform 50 BBFB iterations.

Table 8.1: BBFB applied to a 3D sphere of radius $r = \frac{1}{k_0}$.

ε_r	Order of $\mathbf{Z}$	No. of strips	Gr./Buf. regions	$\psi^{(5)}$	$\psi^{(10)}$	$\psi^{(20)}$	$\psi^{(50)}$	Time (s)
4	960	20	2/1	-0.5	-0.3	-0.1	0.3	241.3
4	960	20	2/2	-1.027	-1.056	-1.132	-1.22	257.1
4	960	20	3/1	-0.53	-0.2	-0.15	-0.01	261.3
4	960	20	3/2	-1.17	-1.28	-1.382	-1.478	291.5
4	960	20	3/3	-2.717	-5.40	-9.67	-13.34	321.5
5	960	20	2/1	-0.71	-0.53	-0.15	0.5	239.6
5	960	20	2/2	-1.5	-2.55	-3.76	-4.33	263.2
5	960	20	3/1	-0.61	-0.73	-0.3	-0.1	269.4
5	960	20	3/2	-1.7	-3.67	-7.33	-13.8	295.3
5	960	20	3/3	-2.9	-5.8	-10	-14	335.1
6	3840	30	2/1	-1.71	-1.93	-2.1	-2.9	1103.1
6	3840	30	2/2	-0.51	-0.71	-1.45	-3.54	1214.5
6	3840	30	3/1	-0.72	-0.9	-0.5	-0.25	1251.3
6	3840	30	3/2	-2.15	-4.26	-8.56	-13.1	1517.7
6	3840	30	3/3	-2.98	-6.5	-9.1	-14.3	1734.8
7	3840	30	2/1	-0.93	-0.87	-1.73	-4.3	1119.3
7	3840	30	2/2	-1.98	-2.37	-4.75	-11.89	1324.1
7	3840	30	3/1	-0.92	-1.12	-0.71	-0.3	1296.3
7	3840	30	3/2	-3.21	-5.31	-10.89	-13.1	1458.2
7	3840	30	3/3	-3.5	-6.1	-11.7	-14.2	1791.2

It can be noted in Table 8.1 that the performance of the BBFB method depends on the grouping arrangement chosen, whereby the normalised BBFB error $\psi^{(k)}$ reaches much smaller values for larger buffers albeit at a larger computational cost. For example for a relative permittivity $\varepsilon_r = 5$ the BBFB reaches a normalised error of -13.8 after 50 iterations when using 3 slices as a main subregion and 2 slices as a buffer. When applying the BBFB to the same scattering surface and using 3 slices as a main subregion but using only 1 slice as a buffer subregion, it can be noted that the method is beginning to diverge after 50 iterations.

Performance of the BBFB method versus Krylov iterative solvers

The BBFB performance when applied to 3D closed homogeneous dielectric scatterer was also compared against some of the Krylov iterative solver, and namely preconditioned GMRES, CGNE and BiCGSTAB.

Consider a 3D homogeneous dielectric sphere of radius $r = 2 \cdot \frac{1}{k_0}$ and relative permittivity $\varepsilon_r = 4$ illuminated by a plane wave. This leads to 1920 basis functions, therefore the $\mathbf{Z}$ matrix is of order 3840. The superimposed grid generates 40 slices and each main subregion contains 3 slices, whereas the buffer is composed of 2 slices. The preconditioner used for the GMRES, BiCGSTAB is a diagonal block preconditioner and contains the diagonal block inverses associated with the groups of the $\mathbf{Z}$ matrix. The normalised error of the BBFB, preconditioned GMRES and BiCGSTAB is plotted against the number of complex multiplications in Figure 8.8. The three methods require a similar computation time per iteration. It can be noted that the BBFB outperforms both the GMRES and BiCGSTAB in terms of convergence, reaching a normalised error of -14.

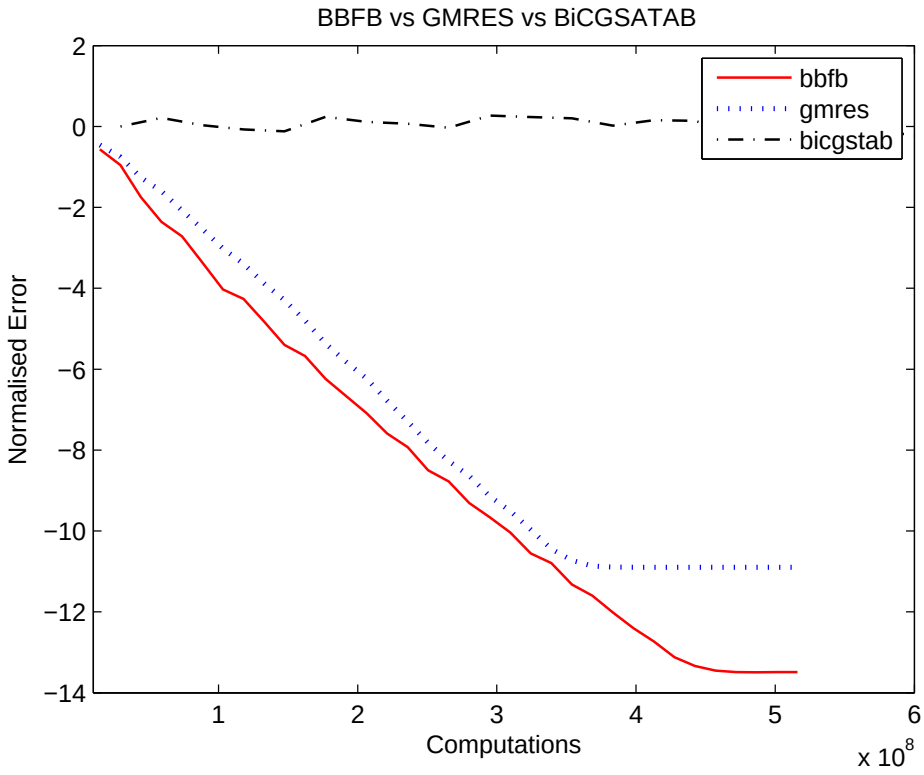

Figure 8.8: BBFB versus Preconditioned GMRES and BiCGSTAB when solving the problem of wave scattering from a 3D sphere

8.2 Conclusion

In this chapter the Buffered Block Forward Backward Method was employed in order to solve the matrix equation obtained after applying the Method of Moments to the Combined Field Integral Equation. The convergence of the BBFB was investigated when applied to 3D closed homogeneous dielectric scatterers. The unknowns are grouped together by superimposing a coarse grid over the scattering structure. It is shown that the BBFB achieves good convergence rates when using an optimal buffer region.

The BBFB is compared against two Krylov solvers, namely the preconditioned GMRES and BiCGSTAB, where the preconditioner used is a block diagonal preconditioner. It is shown that the BBFB outperforms both the preconditioned GMRES and BiCGSTAB in terms of convergence rate. The preconditioned GMRES is shown to have a similar convergence rate.

Chapter 9

Conclusions and Future work

The focus of this thesis is on the efficient solution of electromagnetic wave scattering problems. A general description of Computational Electromagnetics was provided in Chapter 2 where the differential and integral forms of Maxwell's equations were presented in both time and frequency domains. Several of the most popular differential equations numerical techniques, such as Finite Difference Time Domain and Finite Element Method, were briefly described. A general overview of ray optical methods was also provided in the Chapter.

In this thesis integral equation formulations discretised using the Method of Moments are employed in order to solve the scattering problem. The various IE formulations, such as the Electric Field Integral Equation, Magnetic Field Integral Equation, Coupled Field Integral Equation and Combined Field Integral Equation, were derived in Chapter 3. The Method of Moments is a technique used to convert the continuous integral equation to a matrix form. It is applied to the 2D and 3D problems of wave scattering from perfectly electrically conducting scatterers and homogeneous dielectric scatterers.

The matrix equation obtained after applying the MoM to integral equations can be very large. Therefore it can not be solved by direct inversion. Iterative solvers are employed instead. Chapter 4 of this thesis delivers a description of stationary and non stationary iterative solvers. Various preconditioning techniques used in order to improve the solvers are also presented.

The novel Buffered Block Forward Backward method is employed in Chapters 5-8 in

order to solve wave scattering problems involving various types of scattering bodies. The Buffered Block Forward Backward Method (BBFB) is a variation of the Forward Backward technique, which in turn is equivalent the Symmetric Successive Overrelaxation with the relaxation parameter ω set to 1. The Block Forward Backward method is a block variation of the Forward Backward technique, whereby the surface of the scatterer is divided into subregions and the currents are marched from subregion to subregion. The BBFB solver introduces the novelty of computing the interactions between the subregions and their neighbours in order to dampen the artificially induced edge effects.

In Chapter 5 the BBFB is employed in order to solve the problem of electromagnetic wave scattering from a wedge of two perfectly electrically conducting plates. The Electric Field Integral Equation in combination with MoM is used in order to generate the matrix equation in this chapter. The BBFB is shown to have a very good convergence rate, outperforming the preconditioned CGNE. The BBFB has a slower convergence rate as the angle between the two plates diminishes. Nevertheless it still achieves highly accurate results in acceptable time.

In Chapter 6 the Block Forward Backward and Buffered Block Forward Backward methods are used to solve the matrix equation obtained after using the MoM to discretise the Coupled Electric Field Integral Equation. In this chapter the problem of scattering from open and closed 2D homogeneous dielectric structures is considered. The BFB is shown to achieve highly accurate results when applied to open homogeneous scatterers. The BBFB is employed for solving the fields scattered from closed homogeneous structures and it is shown to generate satisfactory results, despite not converging to machine precision.

The BBFB in conjunction with the Coupled Electric Field Integral Equation is extended to the problem of designing 2D TeraHertz photonic band-gap waveguides in Chapter 7. The MoM formulation is validated against the Mie series for TeraHertz frequencies. The BBFB is shown to generate accurate results in acceptable time.

The Combined Field Integral Equation and MoM are used in order to formulate the matrix equation in Chapter 8. The BBFB is applied for solving the problem of electromagnetic wave scattering from 3D homogeneous dielectric structures. It is shown that when a suitable buffer is chosen, the BBFB achieves low normalised error values. A compar-

ison between the BBFB, preconditioned GMRES and preconditioned BiCGSTAB is also performed and it is shown that the BBFB outperforms the two Krylov solvers in terms of convergence.

In terms of future work there are a few problems that can be further investigated. In this thesis the BBFB was applied to relatively simple geometries. The performance of the BBFB can be further investigated when applied to more complex structures. Another issue is the convergence criterion, which was used in this thesis. It is impossible to implement for very large matrix equations, and therefore the spectral radius of the iteration matrix is computationally difficult to obtain. A future work topic may include the formulation of methods to rapidly compute the spectral radius and therefore choose in advance an optimal selection of group/buffer arrangements.

Publications

"Convergence analysis for buffered block forward-backward (BBFB) method applied to EFIE", Conor Brennan, Diana Boguşevschi, IEEE Antenna and Propagation Symposium 2006, New Mexico, USA.

"Buffered Block Forward Backward (BBFB) Method applied to EM wave scattering from homogeneous dielectric bodies", Conor Brennan, Diana Boguşevschi, Scientific Computing in Electrical Science, Sinaia, Romania, 17-22 September 2006, 2006.

"Buffered Block Forward Backward (BBFB) Method applied to EM wave scattering from homogeneous dielectric bodies", Conor Brennan, Diana Boguşevschi, Mathematics in Industry, Volume 11, 2007.

"Buffered Block Forward Backward for computation of fields scattered from dielectric surfaces", Conor Brennan, Diana Boguşevschi, presented at the North American Radio Science Meeting URSI, 2007.

"Comparison of Nonstationary Solvers and the Buffered Block Forward Backward Method for Computing Electromagnetic Wave Scattering", Marie Mullen, Conor Brennan, Diana Boguşevschi, Accepted for the IEE Proceedings IET Microwaves, Antennas and Propagation, 2008.

"Design of 2D TeraHertz band-gap photonic waveguides using an accelerated integral equation technique", Diana Boguşevschi, Elif Degirmenci, Conor Brennan, Pascal Landais, International Conference on Electromagnetics in Advanced Applications, September 14-18, 2009, Torino, Italy.

Appendix

Acronyms

ABC	Absorbing Boundary Condition
BFB	Block Forward Backward Method
BBFB	Buffered Block Forward Backward Method
BiCG	Biconjugate Gradient
BiCGSTAB	Biconjugate Gradient Stabilised
CBF	Characteristic Basis Function
CBFM	Multilevel Characteristic Basis Function
CEM	Computational Electromagnetic Modelling
CFIE	Combined Field Integral Equation
CG	Conjugate Gradient
CGS	Conjugate Gradient Squared
CGNE	Conjugate Gradient Method on the Normal Equation
CGNR	Conjugate Gradient Normal Equation Residual Method
CN/LT	Constant Normal Linear Tangential
CRWG	Curvilinear Rao-Wilton-Glisson
EFIE	Electric Field Integral Equation
EMI	Electromagnetic Interference
EMC	Electromagnetic Compatibility
FB	Forward Backward

FDTD	Finite Difference Time-Domain Method
FEM	Finite Element Method
GFB	Generalised Forward Backward
GMRES	Generalized Minimal Residual
GO	Geometrical Optics
GTD	Geometrical Theory of Diffraction
IE	Integral Equation
MoM	Method of Moments
MOMI	Method of Ordered Multiple Interactions
MFIE	Magnetic Field Integral Equation
MR	Multiresolution
MSMM	Multiple Sweep Method of Moments
PDE	Partial Differential Equation
PEC	Perfect Electric Conductor
PNM	Progressive Numerical Method
RWG	Rao-Wilton-Glisson
SBR	Shooting and Bouncing rays
SDT	Spatial Decomposition Technique
SFIE	Surface Field Integral Equation
SOR	Successive Overrelaxation
SSOR	Symmetric Successive Overrelaxation
TM	Transverse Magnetic
UTD	Uniform Theory of Diffraction

Units

$\bar{\boldsymbol{\mathcal{E}}}$	electric field intensity	V/m	Volts per metre
$\bar{\boldsymbol{\mathcal{H}}}$	magnetic field intensity	A/m	Amperes per metre
$\bar{\boldsymbol{\mathcal{B}}}$	magnetic flux density	$\mathrm{W/m^3}$	Webers per square metre
$\bar{\boldsymbol{\mathcal{D}}}$	electric flux density	$\mathrm{C/m^2}$	Coulombs per square metre
$\bar{\boldsymbol{\mathcal{K}}}^i$	source magnetic current density	$\mathrm{V/m^2}$	Volts per square metre
$\bar{\boldsymbol{\mathcal{J}}}^i$	source electric current density	$\mathrm{A/m^2}$	Amperes per square metre
ρ_e	electric charge density	$\mathrm{C/m^3}$	Coulombs per cubic metre
ρ_m	magnetic charge density	$\mathrm{W/m^3}$	Webers per cubic metre
ε	permittivity	F/m	Farad per metre
μ	permeability	H/m	Henries per metre
λ	wavelength	m	metre
k	wavenumber	$\mathrm{m^{-1}}$	reciprocal metre

References

[1] S. I. Umran and S. I. Aziz. *Engineering Electromagnetics*. Addison Wesley Longman, Menlo Park, California, 1999.

[2] Constantine A. Balanis. *Advanced Engineering Electromagnetics*. John Wiley and Aons, 1989.

[3] Raj Mittra Andrew F. Peterson, Scott L. Ray. *Computational Methods for Electromagnetics*. IEEE Press, Piscataway, New Jersey, USA, 1998.

[4] W. C. Chew, J.M. Jin, E. Michielssen, and Song J. *Fast and efficient algorithms in computational electromagnetics*. Boston Artech House, 2001.

[5] J.C. West. Integral equation formulation for iterative calculation of scattering from lossy rough surfaces. *IEEE Transactions on Geoscience and Remote Sensing*, 38(4):1609–1615, 2000.

[6] R.J. Adams and G.S. Brown. A combined field approach to scattering from infinite elliptical cylinders using the method of ordered multiple interactions. *IEEE Transactions on Antennas and Propagation*, 47(2):364–375, 1999.

[7] A. Glisson and D. Wilton. Simple and efficient numerical methods for problems of electromagnetic radiation and scattering from surfaces. *IEEE Transactions on Antennas and Propagation*, 28(5):593–603, 1980.

[8] S. Rao, D. Wilton, and A. Glisson. Electromagnetic scattering by surfaces of arbitrary shape. *IEEE Transactions on Antennas and Propagation*, 30(3):409–418, 1982.

[9] K. Umashankar, A. Taflove, and S. Rao. Electromagnetic scattering by arbitrary shaped three-dimensional homogeneous lossy dielectric objects. *IEEE Transactions on Antennas and Propagation*, 34(6):758–766, 1986.

[10] Y. Saad and H. A. van der Vorst. Iterative solution of linear systems in the 20th century. *Journal of Computational and Applied Mathematics*, 123:1–33, 2000.

[11] Jeffrey J. Leader. *Numerical Analysis and Scienitfic Computation*. Pearson Education, 2004.

[12] David M. Young. *Iterative Solution of Large Linear Systems*. New York : Academic Press, 1971.

[13] Charles F. Van Loan Gene H. Golub. *Matrix Computations*. The Jhons Hopkins University Press, 1996.

[14] Y. Saad. *Iterative methods for sparse linear systems*. PWS Publishing Co., 1996.

[15] Yousef Saad. *Methods for Sparse Linear Systems*. Society for Industrial and Applied Mathematics, 2003.

[16] A Jennings and J.J. McKeown. *Matrix Computation*. John Wiley and Sons, 1992.

[17] R. et al. Barrett. *Templates for the solution of linear systems : building blocks for iterative methods*. Philadelphia, PA : SIAM, 1994.

[18] Wolfgang Hackbusch. *Iterative Solution of Large Sparse Systems of Equations*. New York : Springer-Verlag, 1994.

[19] J. B. Fraleigh and R. A. Beauregard. *Linear Algebra*. Addison Wesley Publishing Company, 1995.

[20] J.C. West and J.M. Sturm. On iterative approaches for electromagnetic rough-surface scattering problems. *IEEE Transactions on Antennas and Propagation*, 47(8):1281–1288, 1999.

[21] Henk A. van der Vorst. *Iterative Krylov Methods for Large Linear Systems*. New York : Cambridge University Press,, 2003.

[22] A. M. Bruaset. *A survey of preconditioned iterative methods*. Harlow, Essex, England : New York : Longman Scientific & Technical, 1995.

[23] K. S. Yee. Numerical solution of initial boundary value problems involving maxwell's equations in isotropic media. *IEEE Transactions on Antennas and Propagation*, 14:302–307, 1966.

[24] A. Taflove. Review of the formulation and applications of the finite-difference time-domain method for numerical modeling of electromagnetic wave interactions with arbitrary structures. *Wave Motion*, 10:547 – 582, 1998.

[25] S.J. Cooke, M. Botton, and B. Antonsen Jr., T.M.and Levush. A leapfrog formulation of the 3-d adi-fdtd algorithm. *International Journal of Numerical Modelling: Electronic Networks, Devices and Fields*, 22:187–200, 2009.

[26] R. Luebbers, F. P. Hunsberger, K. S. Kunz, R.B. Standler, and M. Schneider. A frequency-dependent finite-difference time-domain formulation for dispersive materials. *IEEE Transactions on Electromagnetic Compatibility*, 32:222 – 227, 1990.

[27] C.E. Brench and O.M. Ramahi. Source selection criteria for fdtd models. In *Proc. IEEE International Symposium on Electromagnetic Compatibility*, volume 1, pages 491–494 vol.1, 1998.

[28] O. M. Ramahi B. Archambeault, C. Brench. *EMI/EMC computational modeling handbook*. Kluwer Academmic Publishers, 2001.

[29] Ulf Andersson. *Time-Domain Methods for Maxwell Equations*. PhD thesis, Stockholm Royal Insitute of Technology, 2001.

[30] Thomas Jonas Klemas. *Full-wave Algorithms for Model Order Reduction and Electromagnetic Analysis of Impedance and Scattering*. PhD thesis, Massachusetts Institute of Technology, 2005.

[31] Quibo Ye. *Electromagnetic Scattering by numerical methods applicable for large structures*. PhD thesis, University of Manitoba, 2000.

[32] A. Buerkle and K. Sarabandi. Analysis of acousto-electromagnetic wave interaction using the finite-difference time-domain method. *IEEE Transactions on Antennas and Propagation*, 56:2191 – 2199, 2008.

[33] J.C. Olivier. On the synthesis of exact free space absorbing boundary conditions for the finite-difference time-domain method. *IEEE Transactions on Antennas and Propagation*, 40:456 – 460, 1992.

[34] J.L. Volakis and L.C. Kempel. Electromagnetics: computational methods and considerations. *IEEE computational science & engineering*, 2:42–57, 1995.

[35] Weng Cho Chew, Jian-Ming Jin, Cai-Cheng Lu, E. Michielssen, and J.M. Song. Fast solution methods in electromagnetics. *IEEE Transactions on Antennas and Propagation*, 45(3):533–543, 1997.

[36] J.L. Volakis. *Finite element method for electromagnetics : antennas, microwave circuits, and scattering applications*. New York : IEEE Press, 1998.

[37] X. Yuan. Three-dimensional electromagnetic scattering from inhomogeneous objects by the hybrid moment and finite element method. *IEEE Transactions on Microwave Theory and Techniques*, 38(8):1053–1058, 1990.

[38] Haiping Cao, Jian Zhu, Zhenhong Fan, and R.S. Chen. Febi solution of scattering from 3d bianisotropic medium objects above a lossy half space. In *Proc. Asia-Pacific Microwave Conference APMC 2008*, pages 1–4, 2008.

[39] R. Wang and J.-M. Jin. A finite element-boundary integral formulation for numerical simulation of scattering by discrete body of revolution geometries. *Electromagnetics*, v 27:65–86, 2007.

[40] S. Adda, L. Anglesio, G. d'Amore, M. Mantovan, and Menegolli M. Ray-tracing techniques to assess the electromagnetic field radiated by radio base stations: application and experimental validation in an urban environment. *Radiation Protection Dosimetry*, 111:339–342, 2004.

[41] D. Jenn. Geometrical optics and the geometrical theory of diffraction. Technical report, Naval Posgraduate School, Monterey, Claifornia, 2004.

[42] J.A.G. Malherbe D.A. McNamara, C.W.I.Pistorius. *Introduction to the uniform geometrical theory of diffraction*. Boston : Artech House, 1990.

[43] J.B. Keller. Geometrical theory of diffraction. *Journal of the Optical society of Amercia*, 52:116–130, 1962.

[44] R.G. Kouyoumjian and P.H. Pathak. A uniform geometrical theory of diffraction for an edge in a perfectly conducting surface. *Proceedings of the IEEE*, 62:1448–1461, 1974.

[45] R. Matschek. A geometrical optics and uniform theory of diffraction based ray tracing optimisation by a genetic algorithm. *Academie des Sciences. Comptes Rendus, Physique*, 6:595–603, 2005.

[46] Jia Minghua, Zheng Guoxin, and Ji Wenli. A new model for predicting the characteristic of rf propagation in rectangular tunnel. In *Proc. China-Japan Joint Microwave Conference*, pages 268–270, 2008.

[47] J. Ma, R. Mittra, and N. Huang. Improving the convergence of the iterative solution of matrix equations in the method of moments formulation using extrapolation techniques. *IEE Proceedings -Microwaves, Antennas and Propagation*, 150(4):253–257, 2003.

[48] C.J. Reddy, M.D. Deshpande, C.R. Cockrell, and F.B. Beck. Fast rcs computation over a frequency band using method of moments in conjunction with asymptotic waveform evaluation technique. *IEEE Transactions on Antennas and Propagation*, 8:1229–1233, 1998.

[49] M. Lashab, C. Zebiri, and F. Benabdelaziz. Wavelet-based moment method analysis of horn antenna for millimeter-wave applications. In *Proc. International Conference on Multimedia Computing and Systems ICMCS '09*, pages 41–45, 2009.

[50] J. Richmond. A wire-grid model for scattering by conducting bodies. *IEEE Transactions on Antennas and Propagation*, 14(6):782–786, 1966.

[51] K.S.H. Lee, L. Marin, and J.P. Castillo. Limitations of wire-grid modeling of a closed surface. *IEEE Transactions on Electromagnetic Compatibility*, EMC-18(3):123–129, 1976.

[52] D. Knepp and J. Goldhirsh. Numerical analysis of electromagnetic radiation properties of smooth conducting bodies of arbitrary shape. *IEEE Transactions on Antennas and Propagation*, 20(3):383–388, 1972.

[53] Nan Wang, J. Richmond, and M. Gilreath. Sinusoidal reaction formulation for radiation and scattering from conducting surfaces. *IEEE Transactions on Antennas and Propagation*, 23(3):376–382, 1975.

[54] A. Sankar and T.C. Tong. Current computation on complex structures by finite-element method. *Electronics Letters*, 11(20):481–482, 1975.

[55] F.P. Andriulli, F. Vipiana, and G. Vecchi. Hierarchical bases for nonhierarchic 3-d triangular meshes. *IEEE Transactions on Antennas and Propagation*, 56(8):2288–2297, 2008.

[56] R.-S. Chen, J. Ding, D.Z. Ding, and Z.H. Fan. A multiresolution curvilinear rao-wilton-glisson basis function for fast analysis of electromagnetic scattering. *IEEE Transactions on Antennas and Propagation*, 57:3179–3188, 2009.

[57] R.D. Graglia, D.R. Wilton, A.F. Peterson, and I.-L. Gheorma. Higher order interpolatory vector bases on prism elements. *IEEE Transactions on Antennas and Propagation*, 46(3):442–450, 1998.

[58] Gang Kang, Jiming Song, Weng Cho Chew, K.C. Donepudi, and Jian-Ming Jin. A novel grid-robust higher order vector basis function for the method of moments. *IEEE Transactions on Antennas and Propagation*, 49(6):908–915, 2001.

[59] R.D. Graglia and G. Lombardi. Singular higher order divergence-conforming bases

of additive kind and moments method applications to 3d sharp-wedge structures. *IEEE Transactions on Antennas and Propagation*, 56(12):3768–3788, 2008.

[60] J. Laviada, F. Las-Heras, M.R. Pino, and R. Mittra. Solution of electrically large problems with multilevel characteristic basis functions. *IEEE Transactions on Antennas and Propagation*, 57(10):3189–3198, 2009.

[61] Mei Song Tong, Weng Cho Chew, B.J. Rubin, J.D. Morsey, and Lijun Jiang. On the dual basis for solving electromagnetic surface integral equations. *IEEE Transactions on Antennas and Propagation*, 57(10):3136–3146, 2009.

[62] A. Buffa and S.H. Christiansen. A dual finite element complex on the barycentric refinement. *Mathematics of Computation*, 76:1743–1769, 2007.

[63] Q. Ye and L. Shafai. Performance of the progressive numerical method and its comparison with the modified spatial decomposition technique in solving large scattering problems. *IEE Proceedings -Microwaves, Antennas and Propagation*, 145(2):169–174, 1998.

[64] A. Iodice. Forward-backward method for scattering from dielectric rough surfaces. *IEEE Transactions on Antennas and Propagation*, 50(7):901–911, 2002.

[65] A. Iodice. Scattering from natural soils modeled by dielectric fractal profiles: the forward-backward approach. *IEEE Transactions on Geoscience and Remote Sensing*, 42(1):77–85, 2004.

[66] A. Iodice. Forward-backward iterative method for scattering by dielectric fractal surfaces. *International Geoscience and Remote Sensing Symposium*, 2:1254–1256, 2002.

[67] A. Iodice. Computation of scattering from dielectric rough surfaces via forward-bacward method. *International Geoscience and Remote Sensing Symposium*, 3:1381–1383, 2001.

[68] D. A. Kapp and G. S. Brown. A new numerical method for rough-surface scattering calculations. *IEEE Transactions on Antennas and Propagation*, 44(5):711–721, 1996.

[69] D. Holliday, L. L.. DeRaad Jr., and G. J. St-Cyr. Forward-backward: A new method for computing low-grazing angle scattering. *EEE Transactions on Antennas and Propagation*, 44:722 – 729, 1996.

[70] C.T. Kelley. *Iterative Methods for Linear and NOnlinear Equations*. Society for Industrial and Applied Mathematics, 1995.

[71] Y. Yang, Z.H. Fan, D.Z. Ding, and Liu S.B. Application of the preconditioned gmres to the crank-nicolson finite-difference time-domain algorithm for 3d full-wave analysis of planar circuits. *Microwave and Optical Technology Letters*, 50:1458–1463, 2008.

[72] Z.B. Ye, D.Z. Ding, Z.H. Fan, and Yang Y. Analysis of waveguides by use of the time-domain finite-element method solved by preconditioned iterative methods. *IET Microwaves, Antennas and Propagation*, 3:23–31, 2009.

[73] K.F. Tsang, M. Lei, and Chen R.S. Application of the preconditioned conjugate-gradient algorithm to the mixed potential integral equation. *IEEE Antennas and Propagation Society, AP-S International Symposium (Digest), v 4, p 630-633, 2002*, 4:630–633, 2002.

[74] D.Z. Ding, E.K.N. Yung, R.S. Chen, and Rui P.L. Fast analysis of combined dielectric/conducting scattering problem using preconditioned loose gmres method. In *Asia-Pacific Microwave Conference Proceedings, APMC*, 2005.

[75] M. A. Sharkawy, V. Demir, and A Elsherbeni. An efficient ilu preconditioning for highly sparse matrices constructed using the fdfd method. *IEEE Antennas and Propagation Magazine*, 49:135 – 139, 2007.

[76] C.L. Rino, K.J. Doniger, and J.R. Martinez. The method of ordered multiple interactions for closed bodies. *IEEE Transactions on Antennas and Propagation*, 51(9):2327–2334, 2003.

[77] P. Tran. Calculation of the scattering of electromagnetic waves from a two-dimensional perfectly conducting surface using the method of ordered multiple interaction. *Waves in Random Media*, 7:295–302, 1997.

[78] D. Holliday, L.L. DeRaad, and G.J. St-Cyr. Forward-backward method for scattering from imperfect conductors. *IEEE Transactions on Antennas and Propagation*, 46(1):101–107, 1998.

[79] M.R. Pino, J. L. Rodriguez, and Burkholder R. J. Generalized forward-backward method for analyzing the scattering from targets on ocean-like rough surfaces. *IEEE Transactions on Antennas and Propagation*, 47:961–969, 1999.

[80] K. Umashankar, S. Nimmagadda, and A. Taflove. Application of integral equation and method of moments for electrically very large scatterers using spatial decomposition technique. In *Proc. AP-S Antennas and Propagation Society International Symposium Merging Technologies for the 90's. Digest*, pages 76–79 vol.1, 1990.

[81] L. Shafai. A progressive numerical method (pnm) and its application to large field problems. *Antennas and Propagation Society International Symposium*, 14:348 – 350, 1976.

[82] D. Torrungrueng and E. H. Newman. Multiple sweep method of moments (msmm) analysis of electrically large bodies. *IEEE Transactions on Antennas and Propagation*, 45:1252–1258, 1997.

[83] K.R. Umashankar, S. Nimmagadda, and A. Taflove. Numerical analysis of electromagnetic scattering by electrically large objects using spatial decomposition technique. *IEEE Transactions on Antennas and Propagation*, 40(8):867–877, 1992.

[84] H. Zhai and C. Liang. A fast wideband analysis of radiation and scattering problems by impedance-matrix interpolation combined with progressive numerical method. *Microwave and Optical Technology Letters*, 43:56–59, 2004.

[85] M. Mullen, C. Brennan, and T. Downes. A hybridized forward backward method applied to electromagnetic wave scattering problems. *IEEE Transactions on Antennas and Propagation*, 57(6):1846–1850, 2009.

[86] C. Brennan, P. Cullen, and M. Condon. A novel iterative solution of the three

dimensional electric field integral equation. *IEEE Transactions on Antennas and Propagation*, 52(10):2781–2785, 2004.

[87] C. Brennan and D. Bogusevschi. Convergence analysis for buffered block forward-backward (bbfb) method applied to efie. In *Proc. IEEE Antennas and Propagation Society International Symposium 2006*, pages 4045–4048, 2006.

[88] D.E. Lawrence and K. Sarabandi. Acoustic and electromagnetic wave interaction: analytical formulation for acousto-electromagnetic scattering behavior of a dielectric cylinder. *IEEE Transactions on Antennas and Propagation*, 49(10):1382–1392, 2001.

[89] M. Koch. Therahertz technology: A land to be discovered. *Optics and Photonics News*, 18:20–25, 2007.

[90] J. Fitzgerald, E. Berry, N. N. Zinovev, G. C. Walker, M. A. Smith, and J. M. Chamberlain. An introduction to medical imaging with coherent terahertz frequency radiation'. *Physics in Medicine and Biology, vol. 47, pp. 67-84, 2002.*, 47:67–84, 2002.

[91] M. Ciesla, D. D. Arnone, A. Corchia, D. Crawley, C. Longbottom, and E. H. Linfield. Biomedical applications of terahertz pulse imaging. *Proceedings of the SPIE*, 3934:73 – 81, 2000.

[92] E. Yablonovitch. Inhibited spontaneous emission in solid-state physics and electronics. *Physical Review Letters*, 58:2059–2062, 1987.

[93] S. John. Strong localization of photons in certain disordered dielectric superlattices. *Physical Review Letters*, 58:2486–2489, 1987.

[94] M. Johri, Y. A. Ahmed, and Bezboruah T. Photonic band gap materials: Technology, applications and challenges. *Current Science*, v 92:1361–1365, 2007.

[95] K.M. Ho, C.T. Chan, and C.M. Soukoulis. Existence of a photonic gap in periodic dielectric structures. *Physical Review Letters*, 65:3152–3155, 1990.

[96] E. Yablonovitch and T.J. Gmitter. Photonic band structure: the face-centered-cubic case. *Physical Review Letters*, 63:1950–1953, 1989.

[97] E. Yablonovitch and K.M. Gmitter, T.J.and Leung. Photonic band structure: the face-centered-cubic case employing nonspherical atoms. *Physical Review Letters*, 67:2295–2298, 1991.

[98] E.R. Brown and O.B. McMahon. Large electromagnetic stop bands in metallodielectric photonic crystals. *Applied Physics Letters*, 67:2138–2140, 1995.

[99] S. Fan, P. R. Villeneuve, and J. D. Joannopoulos. Large omnidirectional band gaps in metallodielectric photonic crystals. *Physical Review B (Condensed Matter)*, 54:11245–11251, 1996.

[100] K.M. Ho, C.T. Chan, C.M. Soukoulis, R. Biswas, and M. Sigalas. Photonic band gaps in three dimensions: New layer-by-layer periodic structures. *Solid State Communications*, 89:413–416, 1994.

[101] C. Jin, B. Cheng, Z. Li, and D. Zhang. Two dimensional metallic photonic crystal in the thz range. *Optics Communications*, 166:9–13, 1999.

[102] S. W. Wang, W. Lu, X. S. Chen, Z. F. Li, and Shen X. C. Two-dimensional photonic crystal at thz frequencies constructed by metal-coated cylinders. *Journal of Applied Physics*, 93:9401–9403, 2003.

[103] A. L. Bingham and D. R. Grischkowsky. Terahertz 2-d photonic crystal waveguides. *IEEE Microwave and Wireless Components Letters*, 18:428–430, 2008.

[104] Z. Jian, J. Pearce, and D. M. Mittleman. Two-dimensional photonic crystal slabs in parallel-plate metal waveguides studied with terahertz time-domain spectroscopy. *Semiconductor Science and Technology*, 20:S300–S306, 2005.

[105] H. Kurt and D.S. Citrin. Photonic crystals for biochemical sensing in the terahertz region. *Applied Physics Letters*, 87:41108–1–3, 2005.

[106] M. Goto, A. Quema, H. Takahashi, S. Ono, and N. Sarukura. Plastic photonic crystal fiber as terahertz waveguide. *Conference on Lasers and Electro-Optics, 2004. (CLEO)*, 1:3 pp. vol.1–, May 2004.

[107] S. Q. Lou, T. Y. Guo, and H. Fang. A new type of terahertz waveguides. *Chinese Phys. Lett.*, 23:235–238, 2006.

[108] L. Vincetti. Hollow core photonic band gap fibre for thz applications. *Microwave and Optical Technology Letters*, 51:1711–1714, 2009.

[109] Y. Zhao and D. Grischkowsky. Terahertz demonstrations of effectively two-dimensional photonic bandgap structures. *Optics Letters*, 31:1534–1536, 2006.

[110] S. Li, H.-W. Zhang, Q.-Y. Wen, Y.-Q. Song, W.-W. Ling, and Y.-X. Li. Improved amplitude-frequency characteristics for t-splitter photonic crystal waveguides in terahertz regime. *Applied Physics B: Lasers and Optics*, 95:745–749, 2009.

[111] R. Meisels, P. Oberhumer, F. Kuchar, F. Aldrian, and R. Gajic. Wide band gaps and low-loss waveguiding in ceramic high dielectric constant photonic crystals. *Journal of Applied Physics*, 102:094106–1–4, 2007.

[112] J. D. Joannopoulos, S. G. Johnson, Winn J. N., and Meade R. D. *Photonic Crystals: Molding the Flow of Light*. Princeton University Press, 2008.

[113] H. Liu, J. Yao, D. Xu, and P. Wang. Propagation characteristics of two-dimensional photonic crystals in the terahertz range. *Applied Physics B (Lasers and Optics)*, B87:57–63, 2007.

[114] C. Brennan and D. Bogusevschi. Buffered block forward backward (bbfb) method applied to em wave scattering from homogeneous dielectric bodies. *Mathematics in Industry*, 11:301–308, 2007.

[115] Julius Adams Stratton. *Electromagnetic Theory*. McGraw-Hill Book Company, 1941.